Optical and Capacitive Alignment of ATLAS Muon Chambers for Calibration with Cosmic Rays

Diplomarbeit

Fakultät für Physik

der

Ludwig-Maximilians-Universität München

vorgelegt von

Gerd Wolfram Stiller

München, den 13. Dezember 2002

1. Gutachter:	*Prof. Dr. Dorothee Schaile*
2. Gutachter:	*Prof. Dr. Martin Faessler*

Man muß noch Chaos in sich haben, um einen
tanzenden Stern gebären zu können.

Friedrich Nietzsche, Also sprach Zarathustra

Contents

Introduction and Overview

Over the last few decades experimental high energy physics has allowed mankind to develop a more thorough understanding of the underlying principles of nature. Todays experimental particle physics is searching for an answer to the question of what “basic building blocks” matter consists of and how exactly these “basic building blocks” interact with each other.

Together with the discoveries made and the goals achieved in experimental particle physics, the ambition to discover unknown particles and unknown interactions (so-called “new physics”) and to develop a model exactly describing “new” as well as “known” physics based on experimental data has grown. Over the past years the exploration of new phenomena has required higher center-of mass energies in turn requiring experiments of a larger scale.

Apart from the search for “new physics” one of the main objects in experimental particle physics is to thoroughly test a model describing all currently known elementary particles and all their known interactions. This so-called Standard Model enabled physicists to accurately describe and predict all results gained by particle physics experiments to date [1].

However, one last particle predicted by the Standard Model still remains to be found, the Higgs boson. This pseudoscalar boson, the mass of which is a free parameter of the Standard Model, has been introduced to allow for the mass generation of the massive particles without destroying gauge invariance. Upon the start of operation of the hadron collider LHC[1] in 2007 currently being built at CERN[2], proton-proton collisions at center-of-mass energies up to 14 TeV will make the discovery of the Higgs boson and the determination of its mass in case of its existence possible.

The search for the Higgs boson or more generally the search for the origin of particle masses and the exploration of a new energy domain covering a wide range of theoretical models for new particles and new phenomena constitute two major goals of the LHC experiments ATLAS[3] and CMS[4] which are currently in

---

[1] LHC is an acronym for Large Hadron Collider.

[2] CERN is an acronym for Conseil Européen pour la Recherche Nucléaire, now “Organisation européenne pour la recherche nucléaire” or “European Organization for Nuclear Research”.

[3] ATLAS is the acronym for A Toroidal LHC Apparatus.

[4] CMS is the acronym for Compact Muon Solenoid.

the construction phase.

This diploma thesis focuses on one small aspect closely linked to and needed for the ATLAS experiment - the optical and capacitive alignment of ATLAS BOS[5] muon chambers in the Munich Cosmic-Ray Test-Facility.

The alignment monitoring is needed to guarantee mechanical stability of the cosmic-ray test-facility setup during the data-acquisition periods for tests of the precision muon chambers installed. These tests are conducted to ensure full reliability of the muon chamber and all its subsystems for the time when the chambers have to cope with the stringent requirements of the ATLAS muon spectrometer.

During the chamber testing their deformations and relative movements with respect to each other are monitored in order to correct the reconstructed muon tracks for these displacements and deformations.

The first part of the first chapter gives a brief introduction to the LHC, outlining the reasons for building a hadron collider and considering its advantages and disadvantages. The second section of that chapter is dedicated to the ATLAS experiment describing the basic detector layout and its underlying physics requirements.

Chapter two is dedicated to the Munich Cosmic-Ray Test-Facility outlining its setup and purpose and showing its importance for the muon spectrometer of the ATLAS experiment.

Chapter three focuses on the importance of the muon chamber alignment within the cosmic-ray test-facility giving a description of the alignment systems used. Their custom setup and their purpose is explained.

Chapter four shows the possibilities of the optical alignment systems based on the analysis of measured data. Models of single chamber deformations and possible chamber movements relative to each other are described. Also, an approach to accurately reconstruct deformations and movements is offered. Furthermore, these deformations and displacements are compared to temperature data in order to point out correlations.

The calibration of the capacitive probes and the analysis of the calibration data is presented in the fifth chapter. An upper limit on the accuracy achieved with that calibration procedure is given.

Finally, the sixth chapter summarizes the methods used and the results gained and gives a brief outlook on the question of what the alignment systems will be capable of in the future.

---

[5] BOS is the acronym for Barrel Outer Small. It "codes" the specific type of muon chamber (either large or small) and its position within the ATLAS detector later on, namely in its barrel part in the outer layer of the muon system (see also 1.2.1).

Chapter 1

The LHC and the ATLAS Experiment

The year 2007 will hopefully mark the starting point of a long and fruitful operation of the LHC project at CERN near Geneva in Switzerland (*Figure 1.1*).

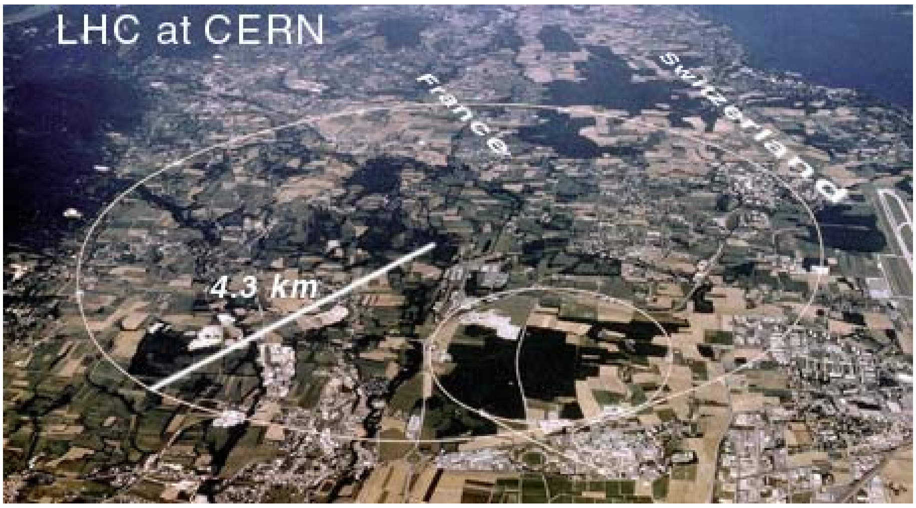

Figure 1.1: Aerial view of the European Organization for Nuclear Research CERN. The position of the accelerators SPS (Super Proton Synchrotron) and LHC (Large Hadron Collider) with respect to the border between France and Switzerland can be seen.

As already shortly outlined in the introduction the Large Hadron Collider is a proton-proton (pp)-storage ring which will allow access to a range of collision energies not reached ever before by any other collider. Hopes are to discover physics beyond the Standard Model (such as SUSY[1] or technicolor), to detect

---

[1] SUSY is the acronym for Supersymmetry.

the Higgs boson (or to rule out its existence) and to determine its mass as well as being able to make precision measurements on already known quantities such as W and the top-quark masses [2]. The two detectors ATLAS and CMS will be the tools used by particle physicists around the world to achieve these ambitious goals.

1.1 The Large Hadron Collider LHC

The pp-storage ring LHC set up in the former LEP[2] tunnel of 27 km circumference opens up the possibility to reach higher energies compared to LEP, because the use of protons for particle collisions is not limited by the energy loss through synchrotron radiation. Formerly this radiation set the practical limit on the acceleration possible with electrons and positrons (see below). Instead, the limit on the energies that can be reached in pp-storage rings is given by the technically realizable magnetic field strength of the beam's bending magnets (see below).

Proton-proton collisions at LHC will allow to reach center-of-mass energies up to 14 TeV. Since the proton is of composite nature, only a fraction of that energy is available to an elementary particle interaction. Quarks and gluons, the constituents of the proton (the so-called "partons"), each carry a fraction of the center-of mass energy of a collision.

The design luminosity of the LHC is 10^{34} $cm^2 s^{-1}$, bunch crossings are 25 ns apart with an average of 23 interactions per crossing at design luminosity. Every bunch will consist of 10^{11} protons in beams having transverse radii of 15 μm [3][3].

The existing PS[4] and SPS[5] accelerator facilities will be reused to deliver protons with an energy of 450 GeV for injection into the Large Hadron Collider (*Figure 1.2*).

Two proton beam pipes are used. These are placed in a common cryostat with superconducting dipole magnets having opposite magnetic field directions. The magnets are able to create magnetic field strengths exceeding 8 T to provide the bending power needed.

The LHC being a hadron collider one question has to be asked and remains to be answered: What disadvantages and what advantages do hadron colliders have?

Readers who have paid attention to what has been said so far with respect to the LHC will point out that not all of the proton energy can be taken advantage of to produce particles. This is due to the compositeness of the proton already mentioned above (the interacting partons carry only a fraction of the proton

---

[2] LEP is the acronym for Large Electron-Positron Collider.

[3] All numbers in this paragraph have to be handled with care and considered preliminary since technical development may still require changes affecting the machine parameters.

[4] PS is the acronym for Proton Synchroton.

[5] SPS is the acronym for Super Proton Synchroton.

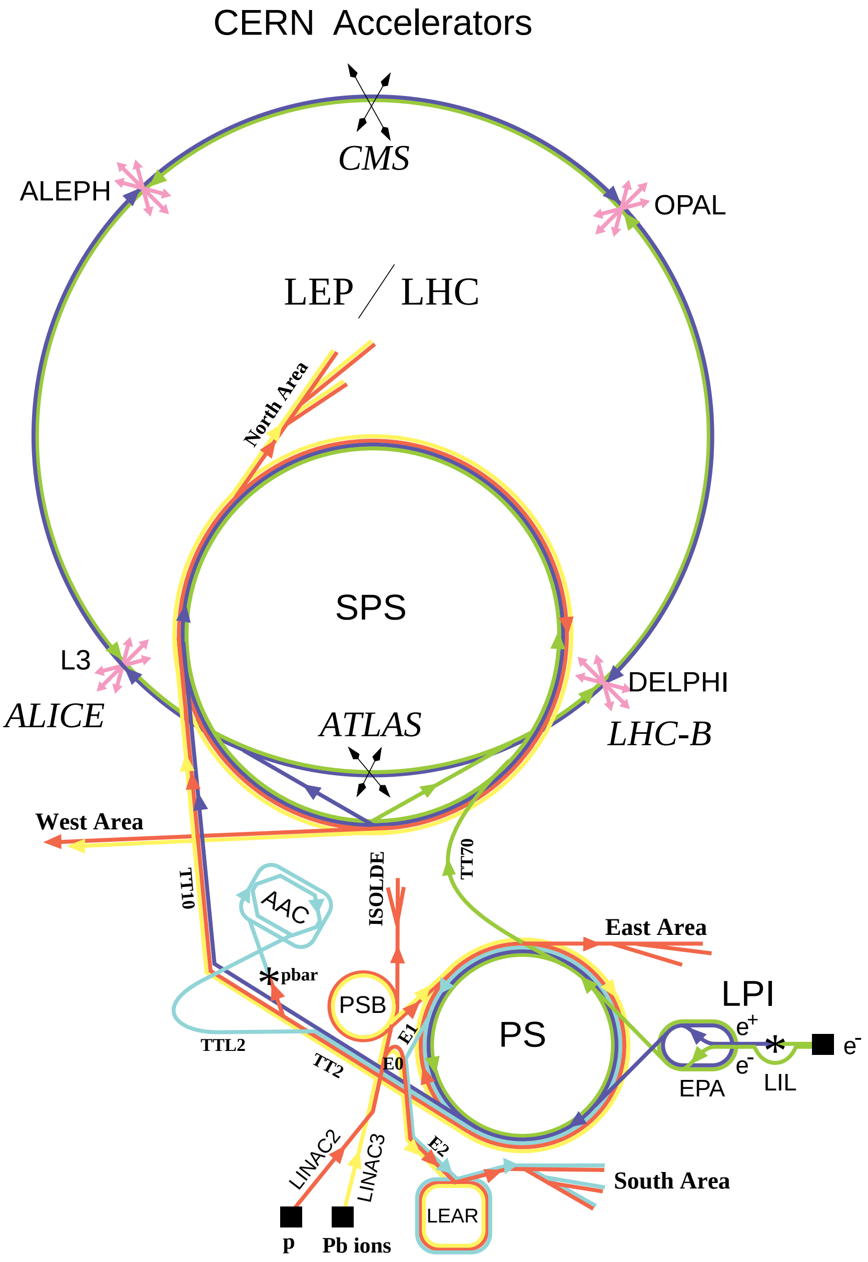

LEP: Large Electron Positron collider
SPS: Super Proton Synchrotron
AAC: Antiproton Accumulator Complex
ISOLDE: Isotope Separator OnLine DEvice
PSB: Proton Synchrotron Booster
PS: Proton Synchrotron

LPI: Lep Pre-Injector
EPA: Electron Positron Accumulator
LIL: Lep Injector Linac
LINAC: LINear ACcelerator
LEAR: Low Energy Antiproton Ring

Figure 1.2: Particle accelerators at CERN. In addition to the LHC accelerator chain and the LHC experiment locations the former LEP experiment sites are also shown [4].

momentum) which is an unfortunate disadvantage. Furthermore, the proton compositeness implies the following necessity: Although the proton energy in the beam may be known perfectly, proper analysis of collision data requires the knowledge of the parton-density functions.

Not disregarding these disadvantages, there are advantages which make hadron colliders like the LHC scientifically profitable. As mentioned before loss of beam energy due to synchrotron radiation cannot generally be disregarded in circular colliders. Synchrotron radiation is emitted by the charged beam particles which are accelerated when the beam is bent by the magnetic force of the magnets to follow the curvature of the ring ([5], p. 676 ff). For a particle of mass m with an energy E, the energy loss ΔE per revolution in a storage ring of radius R is proportional to

$$\Delta E \propto \frac{1}{(mc^2)^4} \frac{E^4}{R} \tag{1.1}$$

which obviously[6] leads to

$$\frac{\Delta E_{proton}}{\Delta E_{electron}} = \left(\frac{m_e}{m_p}\right)^4 \approx 10^{-13} \tag{1.2}$$

[7],[8]. The result of equation (1.2) decreases with the fourth power of the ratio of the rest masses of the beam particles, so a suppression of synchrotron radiation due to the high proton mass results in much higher beam energies being possible in proton-proton (pp) or proton-antiproton ($p\bar{p}$) rings compared to an e^+e^- ring.

Compared e^+e^- cross-sections, another advantage of using protons for collisions is that pp cross-sections are huge. To exploit this advantage, one has to know how to trigger on specific reactions which will be a major experimental challenge in the environment of the LHC.

One further advantage is the continuous momentum distribution of the interacting partons, leading to a wide range of center-of-mass energies of parton-parton systems, although the beam energy of the hadron collider is fixed and remains untouched.

---

[6] $m_p \approx 1836.153\ m_e$ [6], with m_p being the rest mass of the proton and m_e being the rest mass of the electron

1.2 The ATLAS Detector and its Experimental Goals

After having outlined the physics potential of the LHC, its structure and the reasons for building a hadron collider in section 1.1 of this chapter, we will now have a closer look at the ATLAS experiment. First a description of the detector layout and its subsystems is given, then the focus shifts towards the physics possible with this detector layout. Since this thesis deals with the muon chamber alignment, the ATLAS muon spectrometer layout and its performance requirements will be described in more detail.

1.2.1 The ATLAS Detector Layout

In figure 1.3 a three-dimensional view of one of the LHC multi-purpose experiments, the ATLAS detector, is shown. Its width of 44 m as well as its height of 22 m together with its weight of approximately 7000 t already give a rough hint of the scale of the whole experiment.

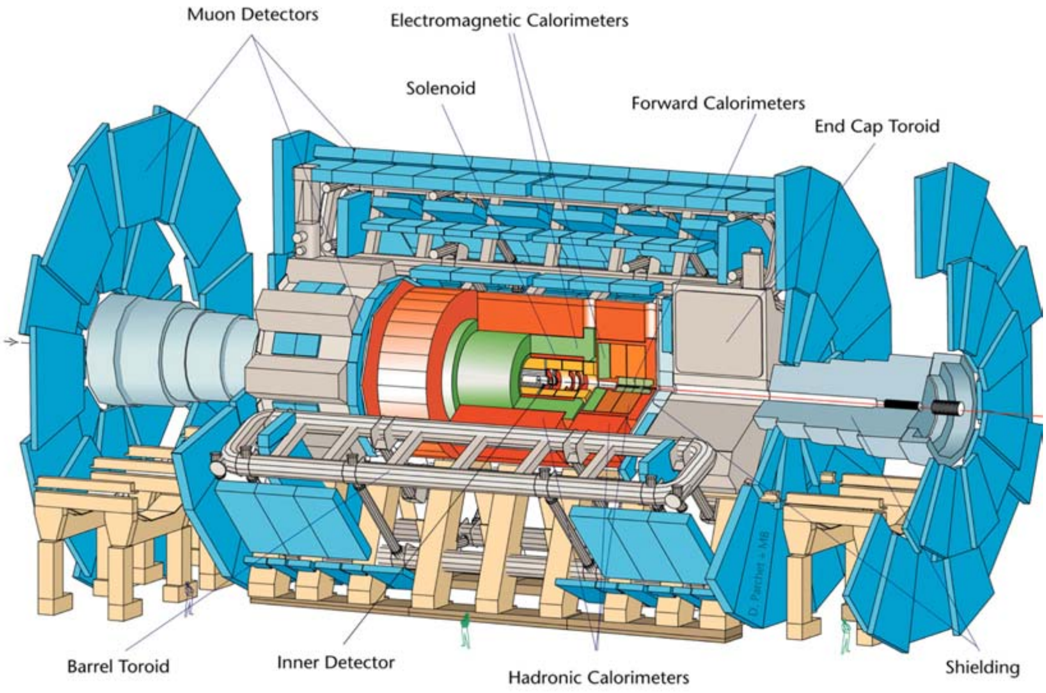

Figure 1.3: Three-dimensional view of the ATLAS detector [2].

The detector is made up by three subsystems, the inner detector, the calorimeters and the muon spectrometer. Starting with the inner detector and moving outwards, these subdetectors are described in the following [2].

The Inner Detector

The inner detector is contained in the superconducting central solenoid magnet which provides a nominal magnetic field of 2 T, thus allowing charge identification and momentum measurement. It combines high-resolution detectors at the inner radii with continuous tracking detectors at the outer radii. This allows the inner detector to fulfill the requirements of identifying particles, of providing high precision tracking close to the primary pp-collision vertex and of finding secondary vertices. It has to withstand an intense radiation background, so only detector technologies being sufficiently radiation hard are employed. Figure 1.4 shows the layout of the inner detector which consists of the following subsystems:

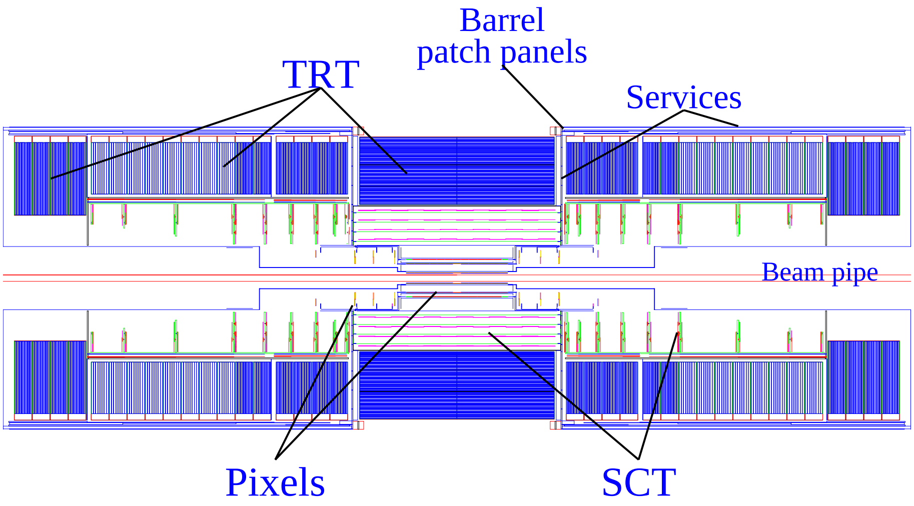

Figure 1.4: Longitudinal view of the ATLAS inner detector [2].

- **The Pixel Detector** is designed to provide a set of highly precise measurements of very high-granularity as close to the interaction point as possible. Therefore it has been arranged in three barrels at radii of ~ 4 cm, 10 cm and 13 cm and five disks with radii between 11 and 20 cm on each side. These layers of so called pixel sensors consist of semiconductor detectors with a two-dimensional segmentation,“pixels” with a size of 50 $\mu m \times 300$ μm.

In the barrel region (for pseudorapidities[7] $|\eta| \leq 1.7$) a resolution of 12 μm in the direction of the cylinder around the beam axis, the so called $R\phi$-direction, and a resolution of 66 μm in the direction along the beam axis, the z-direction, can be achieved.

For $1.7 \leq |\eta| \leq 2.5$ the resolution of the disks in the $R\phi$-direction is comparable to the barrel part whereas the resolution of the r-coordinate measurement will be about 77 μm.

- **The Semiconductor Tracker** consists of eight layers of silicon microstrip detectors alternately shifted under a small stereo angle of 40 μrad to provide measurements with resolutions of 16 μm in the $R\phi$- and of 580 μm in the z-direction in the barrel part.

  The forward regions consist of nine double disks providing equally good resolution in $R\phi$.

  The semiconductor tracker contributes to the measurement of momentum, impact parameter and vertex position as well as providing good pattern recognition because of its high granularity. It covers a range of $|\eta| \leq 2.5$.

- **The Transition Radiation Tracker** makes use of the straw detector technology. Straw detectors are gas-filled tubes of small diameter with a wire placed in their middle. By applying high voltage between the mantle of the tube and the wire, a charged particle passing through the straw is able to ionize the gas. The collected ions and electrons induce a signal in the straw.

  By employing xenon gas to detect transition-radiation photons created in a radiator between the straws, these gain an electron identification capability [2].

  The straw detector technology is intrinsically radiation hard and is able to operate at very high rates, so it is a good choice for this subsystem since it must cope with large occupancy and high counting rates at the LHC design luminosity.

  On average it will allow measurement of another 36 track points with a resolution of 170 μm. Again it is arranged in a barrel part with axial straws (sensitive in the range of $|\eta| \leq 0.7$) and two end-caps (sensitive in the range of $0.7 \leq |\eta| \leq 2.5$).

---

[7] Instead of using the polar angle θ, in high energy physics usually the pseudorapidity $\eta \equiv -\ln \tan \frac{\theta}{2}$ is used. Three pseudorapidity ranges have to be distinguished:

- $|\eta| \leq 1.05$: the barrel region
- $1.05 < |\eta| \leq 1.4$: the transition region
- $1.4 < |\eta|$: the end-cap region

.

The Calorimeters

Moving further outwards the next shell of the ATLAS detector is taken up by the calorimeters. The electromagnetic (EM) calorimeter is designed to measure the energy deposited by electrons and photons and stop these particles from entering other subdetectors. It makes up the inner part of the calorimeters, while the outer part, the hadronic calorimeter has to fulfill the same task for hadrons. The global layout of the calorimeters is shown in figure 1.5.

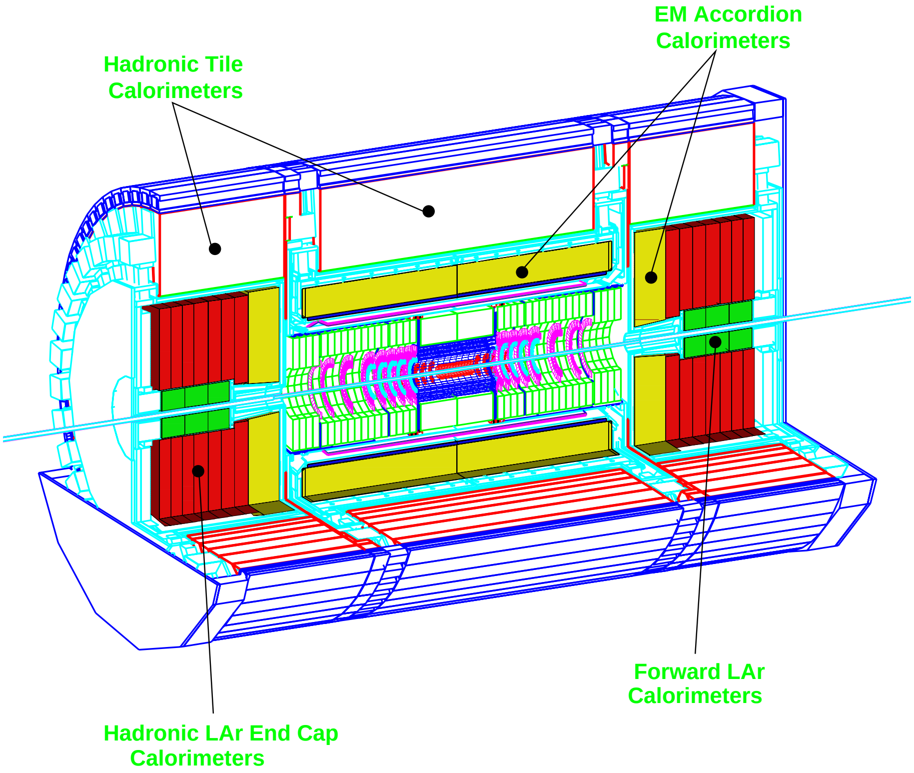

Figure 1.5: Three-dimensional cutaway view of the ATLAS calorimeters [2].

- **Electromagnetic Calorimeter**

  The electromagnetic calorimeter can be subdivided into a barrel and an end-cap part covering a total pseudorapidity range of $|\eta| \leq 3.2$. Over its full coverage it employs lead absorber plates alternating with copper electrodes on Kapton carriers. Each gap between the absorber plates and the electrodes is filled with liquid argon (LAr).

  This LAr detector is accordion-shaped with a total thickness of > 24 radiation lengths (X_0) in the barrel and > 26 X_0 in the end-caps. It has a granularity of $\Delta\eta \cdot \Delta\phi \approx 0.025 \cdot 0.025$ [8], offering an energy resolution

---

[8] ϕ is the azimuthal angle.

of $\Delta E/E = 10\%/\sqrt{E/GeV}$. The granularity and the energy resolution is sufficient to satisfy the physics requirements (reconstruction of jets and measurement of E_T^{miss}[9]).

- **Hadronic Calorimeter**

  The structure of the hadronic calorimeter can be separated into a barrel part and an end-cap part, an already well known concept for the reader. This time however, both parts of the hadronic calorimeters use different detector techniques. On average the total thickness will be about 11 interaction lengths (λ).

  The barrel hadron calorimeter (Tile Calorimeter) makes use of scintillating tiles as active material which are embedded in iron-absorber plates. The readout is realized by wavelength-shifting fibers connected to photomultipliers.

  In the end-cap and forward regions a liquid argon calorimeter with copper or tungsten absorbers similar to the electromagnetic calorimeter is used.

  A total region $|\eta| \leq 4.9$ is covered by the hadronic calorimeters having a granularity between $\Delta\eta \cdot \Delta\phi \approx 0.1 \cdot 0.1$ and $0.2 \cdot 0.1$ depending on the pseudorapidity range. The energy resolution ranges between $\Delta E/E = 50\%/\sqrt{E/GeV}$ and $\Delta E/E = 100\%/\sqrt{E/GeV}$.

The Muon Spectrometer

The outermost and also largest shell of the ATLAS detector is taken up by the muon spectrometer. It defines the overall dimension of the detector. This subdetector is only reached by particles not leading to a signal in the detector due to their weak interactions with matter like neutrinos and by muons, since these can traverse the calorimeters because they only loose energy by ionization. Since strongly interacting particles and electrons are absorbed in the calorimeters, the muon spectrometer detects less particle tracks than the inner detector, so events having a rather clear signature can be expected.

It is the task of the muon spectrometer to allow the precise measurement of the transverse momentum p_t of the muons. It consists of three layers of precision chambers and superconducting toroidal air-core magnets, generating a magnetic field of 0.4 T on average. The use of air-core magnets has the advantage that a very small amount of material has to be traversed by muons crossing the muon spectrometer. This limits multiple scattering effects, which would otherwise degrade the momentum resolution. The layout of the muon spectrometer is shown in figure 1.6.

The underlying idea of the design is to deflect muons coming from the interaction point in longitudinal direction with the help of the toroidal magnetic field.

---

[9] E_T^{miss} is the missing transverse energy.

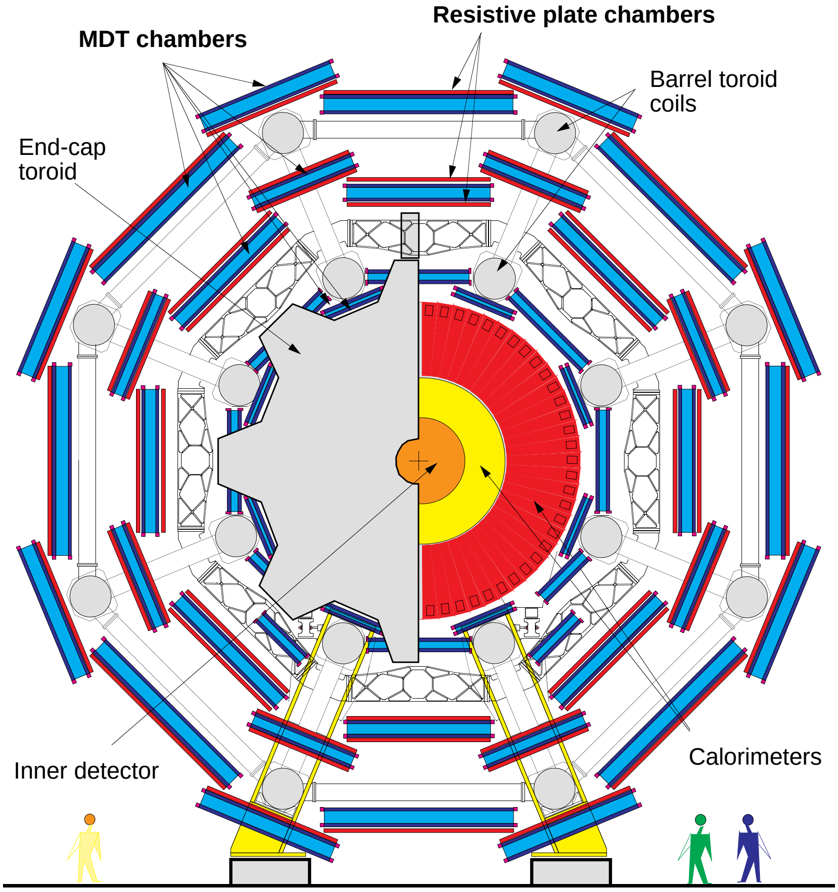

Figure 1.6: Transverse view of the muon spectrometer [9].

It is intended to measure one track segment of the deflected muon track beneath, one within and one above the toroid coils of the magnet. For this purpose two layers of precision chambers are placed outside of the magnetic field (one layer on each side), the third layer, however, is placed within the magnetic field (compare to figure 1.6 and figure 1.7). Knowing the magnetic field map, it is possible to reconstruct the muon momenta from the curvatures of the muon tracks.

Figure 1.7 shows a longitudinal cut through the muon spectrometer. In the barrel region three layers of RPCs[10] are used as trigger chambers, a task taken over by three layers of TGCs[11] in the end-cap and forward regions of the spectrometer. These chambers also offer the possibility to provide a second coordinate measurement, not essential for momentum measurement, but useful for pattern recognition. The high resolution measurement of the precision coordinate (the coordinate in bending direction of the magnetic field) is done through the use of

---

[10] RPC is the acronym for Resistive Plate Chamber.

[11] TGC is the acronym for Thin Gap Chamber.

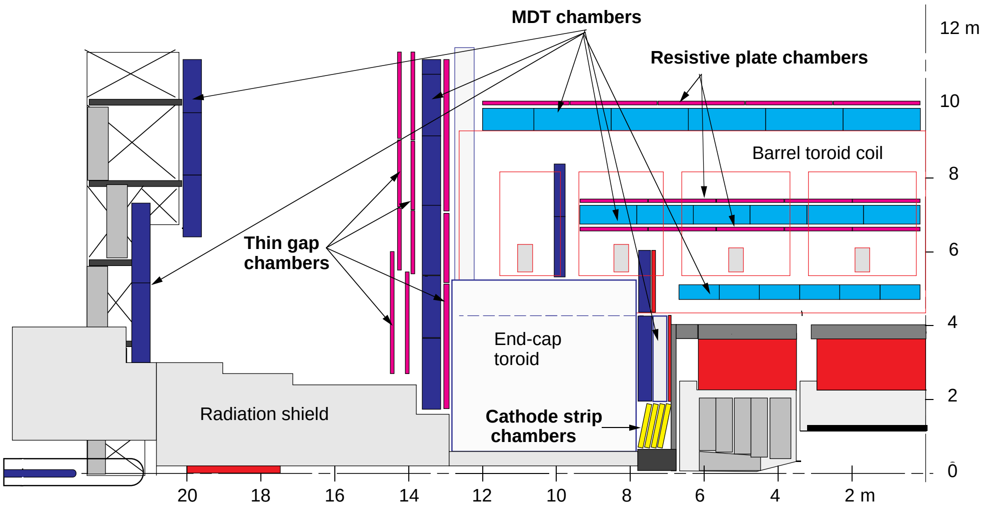

Figure 1.7: Side view of one quadrant of the muon spectrometer [9].

MDT[12] chambers almost throughout the whole spectrometer apart from a small section in the forward region where CSCs[13] are used because of their higher rate capability.

RPC chambers consist of two parallel resistive bakelite plates separated by insulating spacers forming a narrow gas gap of 2 mm. The primary ionization electrons caused by muons crossing the detector volume are multiplied into avalanches by a high, uniform electric field of typically 4.5 kV/mm inducing a signal in the readout strips which have a pitch varying from 30.0 to 39,5 mm. An RPC chamber is able to provide a typical space-time resolution of 1 $cm \times 1ns$ with digital readout.

The TGCs are similar in design to multiwire proportional chambers, with the difference that the anode wire pitch is larger than the cathode-anode distance. Their space-time resolution is comparable to the one of the RPCs.

Multiwire proportional chambers with cathode strip readout are the CSCs. They consist of a symmetric cell in which the anode-cathode spacing is equal to the anode wire pitch. The precision coordinate is obtained by measuring the charge induced on the cathode by the avalanche formed near the anode wire. A spatial resolution of 60 μm is achieved by segmentation of the readout cathode and by charge interpolation between neighboring strips.

The inner layer of the ATLAS muon spectrometer consists of MDT chambers constructed from two multilayers each being formed by four monolayers of drift

---

[12] MDT is the acronym for Monitored Drift Tube, owing to property of the drift-tube chambers that their deformations are being monitored by a built-in optical system once they have left the flat granite assembly table. More details on the chamber structure and the monitoring of the deformations will be given in chapter 3.1.2.

[13] CSC is the acronym for Cathode Strip Chamber.

tubes whereas the MDT chambers of the middle and outer station consist of two multilayers formed by three monolayers of drift tubes.

The length of the drift tubes ranges from 1 m to about 6 m depending on the chamber position foreseen for operation. These tubes are the basic detection element of the MDT chambers and are made of aluminum tubes of 30 mm outer diameter and 400 μm wall thickness with a 50 μm diameter central W-Re wire. This wire is placed inside the tube with an accuracy of 10 μm. The tubes are filled with a mixture of 93% Ar and 7% CO_2 at 3 bar absolute pressure. Using an operating voltage of 3080 V a gas gain of $2 \cdot 10^4$ can be reached.

A muon passing through the gas-filled drift-tube volume ionizes gas atoms on its way through. The secondary electrons created drift in the direction of the electric field towards the central wire in the vicinity of which the field strength accelerates the electrons so much that a charge-carrier avalanche is initiated. This avalanche leads to a signal in the wire allowing to measure the arrival time of the primary electron. The larger the distance between the muon track and the wire the later this signal arrives. A dependence between the drift time of the electrons in the gas-filled volume and the time difference between the trigger of the muon spectrometer and the anode signal exists, allowing to calculate the drift radius out of the measured drift time. The drift radius of a single tube calculated this way is on average precise to 80 μm ("single-tube resolution"). Since the position of the anode wires inside a drift chamber will be known to about 30 μm ("wire-placement accuracy"[14]), the single-tube resolution is altered to $\sqrt{80^2 + 30^2}\ \mu m \approx 85\ \mu m$. Every chamber will contribute a track point with a precision of about $85\ \mu m/\sqrt{6} \approx 35\ \mu m$ or $85\ \mu m/\sqrt{8} \approx 30\ \mu m$ to the total muon track ("intrinsic chamber resolution").

In order to achieve the precision mentioned above the precision chambers of the muon spectrometer have to be aligned in such a way that the alignment contribution to the final measurement error stays well below the intrinsic chamber resolution. Since it will not be possible to keep the geometry of the chambers and their position in the spectrometer stable on the scale of the above mentioned measuring accuracy, no attempt is made at physical chamber repositioning. Instead, the effect of movements and deformations within the spectrometer (i.e. caused by mechanical stress or temperature gradients) on the sagitta measurements of tracks will be corrected for offline using the information from an optical alignment system [9]. The parts of the ATLAS muon spectrometer alignment system relevant to this thesis will be described in section 3.1.

---

[14] The "wire-placement accuracy" is the precision achieved when the muon chambers are built (and the drift tubes and thereby their anode wires are placed relative to the other chamber elements).

1.2.2 The Experimental Goals of the ATLAS Experiment

After having had a close look at the ATLAS detector and its subsystems, the question of the physics in reach naturally pops up. Let us examine in more detail what kind of measurements can be made with the ATLAS detector and which subdetectors are of crucial importance to each physics channel.

Initially the design luminosity foreseen is 10^{33} cm^2s^{-1}. At this luminosity the occupancy in the tracking chambers is expected to still allow an efficient identification of B-mesons giving rise to precision measurements in b- and t-quark physics. The LHC will produce large quantities of these heavy quarks which will allow an unprecedented precision measuring their properties, especially the top mass ([2], especially *Vol. II, chapters 17, 18*).

An important point of interest is the confirmation of theories beyond the Standard Model. Supersymmetry (SUSY) is a particularly promising candidate. In the Minimal Supersymmetric extension of the Standard Model (MSSM) a fermionic degree of freedom is assigned to each bosonic degree of freedom and vice versa. Problems intrinsic to the Standard Model can be overcome by this symmetry because bosonic and fermionic terms cancel each other. The MSSM requires the existence of five Higgs bosons (H^+, H^-, H^0, h^0, A^0) some of which carry charge. Their masses are expected to lie in an energy range accessible to the LHC. For further reference and more detailed information please consult [2] (especially *Vol. II, chapter 20*).

Being one of the last missing "building blocks" of the Standard Model, one of the main experimental goals of the ATLAS experiment is the discovery of the Higgs boson. Using the mechanism of spontaneous symmetry breaking the mass of the electroweak gauge bosons $W^\pm$ and Z^0 can be explained by introducing a scalar Higgs field. Also, the introduction of fermion masses is made possible by Yukawa couplings to the Higgs field. In contrast to the masses of the gauge bosons the coupling constants and, therefore, the lepton masses remain free parameters of the model, just like the mass of the Higgs boson.

The experimental "hunt" for the Standard Model Higgs boson has so far shown that its mass has to be greater than 114.4 GeV at the 95 % confidence level [10]. At the same time theoretical considerations set an upper limit for the Higgs mass of about 1 TeV. Studies have shown that if a Higgs boson with couplings close to the Standard Model predictions exists, it will be discovered at LHC.

Depending on the Higgs mass m_H several different Higgs decay processes are kinematically allowed. Some of these decays leave a particularly clear signature inside the detector and are thus especially suitable for finding the Higgs boson ([2], especially *Vol. II, chapter 19*):

$$80\text{ GeV} < m_H < 150\text{ GeV}: \quad \mathrm{H} \rightarrow \gamma\gamma \tag{1.3}$$

$$\mathrm{H} \rightarrow \mathrm{b}\,\bar{\mathrm{b}} \rightarrow 2\,\mathrm{j} \tag{1.4}$$

$$150\text{ GeV} < m_H < 2\,m_Z \approx 180\text{ GeV}: \quad \mathrm{H} \rightarrow \mathrm{Z}\,\mathrm{Z}^* \rightarrow 4\,\ell^\pm \tag{1.5}$$

$$2\,m_Z < m_H < 800\text{ GeV}: \quad \mathrm{H} \rightarrow \mathrm{Z}\,\mathrm{Z} \rightarrow \begin{cases} 4\,\ell^\pm \\ 2\,\ell^\pm\,2\,\nu \end{cases} \tag{1.6}$$

$$800\text{ GeV} < m_H < 1\text{ TeV}: \quad \mathrm{H} \rightarrow \left\{ \begin{array}{c} \mathrm{Z}\,\mathrm{Z} \\ \mathrm{W}^+\mathrm{W}^- \end{array} \right\} \rightarrow \begin{cases} \ell^\pm\,\nu\,2\mathrm{j} \\ 2\,\ell^\pm\,2\mathrm{j} \\ 2\,\ell^\pm\,2\,\nu \\ 4\,\ell^\pm \end{cases} \tag{1.7}$$

($\ell\epsilon\{\mathrm{e}, \mu\}$, Z^* is a virtual Z, j stands for a hadronic jet).

The requirements the ATLAS detector has to fulfill can be illustrated with the aid of the above mentioned Higgs decay channels. Since the decay processes differ largely from each other and the hadronic background (because of the use of protons for collisions) cannot be neglected, different subdetectors have to be combined:

The electromagnetic calorimeter should allow identification of decays (1.3), whereas thesecond decay channel (1.4) makes a very precise vertex detector necessary.

Looking at the decays (1.6) and (1.7) the eminent need for a good overall detector coverage and a good "co-operation" between several subdetectors, in this case muon spectrometer and electromagnetic as well as hadronic calorimeter, becomes clearly visible.

The largest mass range is covered by decays having leptons in their final states. In (1.5) and (1.6) the final states $4\,\ell^\pm = 2\,\mu^+\,2\,\mu^-$ and $4\,\ell^\pm = \mu^+\,\mu^-\,e^+\,e^-$ occur with the highest probability. They are identified with the help of the muon spectrometer, the precision of which plays a crucial role in being able to accurately identify the muons and to determine their transverse momentum.

The muon spectrometer aims at achieving momentum resolutions of $dp_t/p_t \leq 10\%$ at $1\ TeV$ throughout the whole pseudorapidity range covered. This means not only a good spatial resolution of a single tube ("single-tube resolution", $\leq 80\mu m$) of the MDTs is needed, but also highest requirements are set on the knowledge of the relative geometrical position of the muon chambers, the so called alignment.

The momentum resolution of the muon spectrometer (*Figure 1.8*) is limited by different effects depending on the transversal momentum regime p_t of the muons (illustrated in figure 1.9):

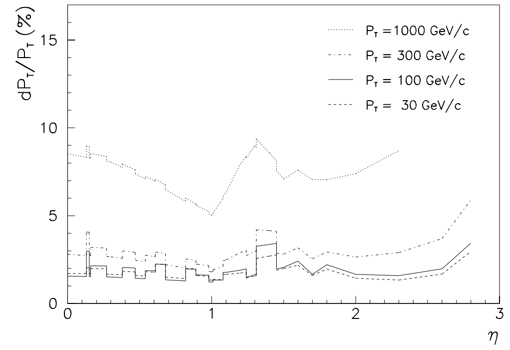

Figure 1.8: Dependence of the momentum resolution of the muon spectrometer on the pseudorapidity η for different transverse momenta p_t [9].

- At low momentum ($p_t < 30\ GeV$) in the central region, energy loss fluctuations in the calorimeters are dominant.
- At moderate momentum ($30 < p_t < 300\ GeV$), the resolution is limited by multiple scattering effects caused by the calorimeter and the magnet coils.
- At high momentum ($p_t > 300\ GeV$), the resolution is dominated by the precision with which the magnetic deflection is measured, i.e. the intrinsic detector resolution and by the precision of the alignment.

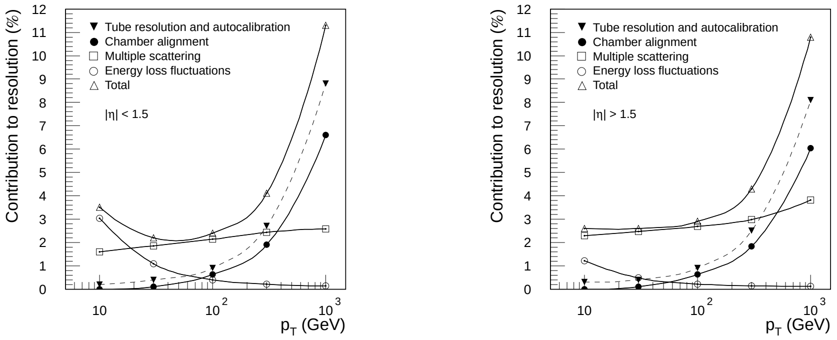

Figure 1.9: Contributions to the momentum resolution of the muon spectrometer. Left: Averaged over $|\eta| < 1.5$. Right: Averaged over $|\eta| > 1.5$. [9]

Keeping the basic design of the ATLAS detector in mind, we have focussed on its physics discovery potential giving reasons for the muon spectrometer being so important for the success of the experiment. We have explained that its performance is limited by different effects. The two most dominant and thus most important of these effects are the spatial resolution of a single tube ("single-tube resolution") and the muon chamber alignment.

We have seen that if the wire-placement accuracy achieved when building the precision chambers is very high, the spatial intrinsic chamber resolution is dominantly limited by the spatial resolution of each of its single tubes ("single-tube resolution"). Therefore it is absolutely crucial to precisely know where the anode wire of each of the drift tubes of each precision chamber is located (otherwise the wire-placement accuracy would degrade the spatial intrinsic chamber resolution). A direct consequence of this requirement was planning, building and operating test facilities for the quality control of muon chambers like the Munich Cosmic-Ray Test-Facility. Here the wire position of a test chamber can be measured relative to the wire position in two reference chambers in addition to the "standard" ATLAS quality control procedures. This test-facility and its purpose will be described in more detail in the following chapter.

Chapter 2

The Munich Cosmic-Ray Test-Facility

The preceding chapter ended with the conclusion that test facilities are needed for the quality control of the MDT chambers built because a lot of requirements have to be fulfilled by these precision chambers in order to exploit the full physics potential of the ATLAS muon spectrometer (compare to 1.2.1 and 1.2.2).

Figure 2.1 is a photograph showing the Munich Cosmic-Ray Test-Facility proposed by A. Staude [11]. The fully operational setup with three chambers can be seen.

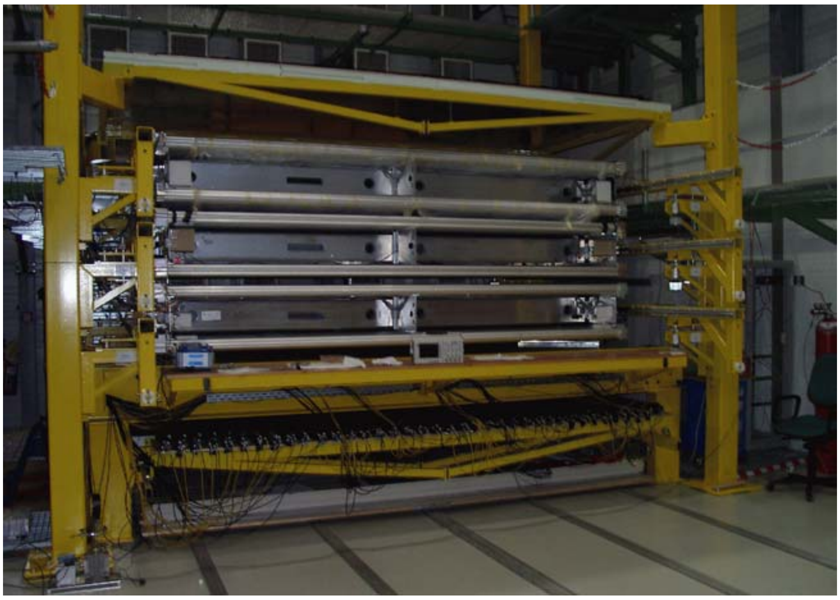

Figure 2.1: Side view of the cosmic-ray test-facility with a complete three-chamber setup.

Let us now have a detailed look at the setup and its components in order to understand how the test facility works.

2.1 The Cosmic-Ray Test-Facility Setup

A schematic view of the experimental setup is given in figure 2.2. It consists of two reference MDT muon chambers whose exact geometry and wire position is known through measurements with an x-ray tomograph at CERN to an accuracy of about 2 μm RMS [12]. These are placed above and below a third chamber, enclosing it in a sandwich structure. The third chamber is the chamber to be tested and will therefore hereafter be called "test chamber". Hits in the reference chambers caused by cosmic muons[1] allow the reconstruction of a track used to calculate the wire positions in the test chamber.

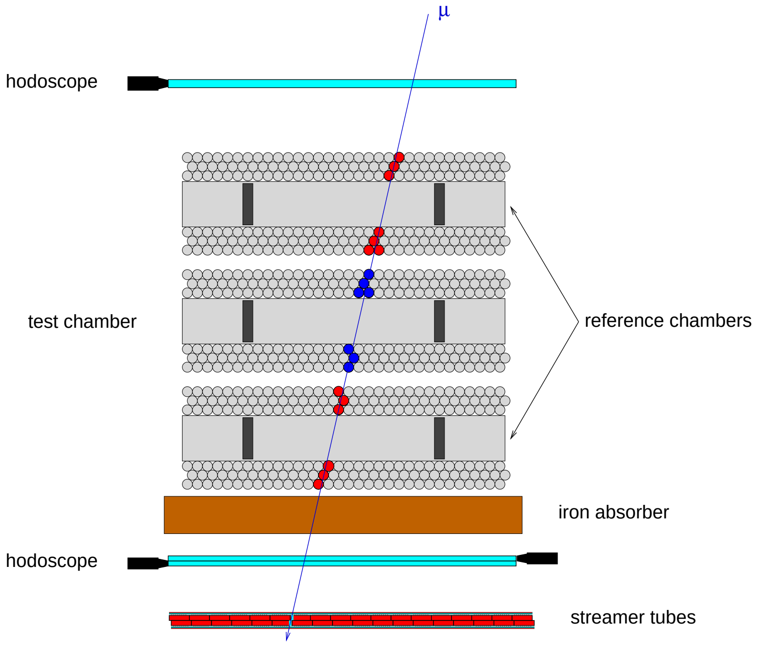

Figure 2.2: Schematic view of the cosmic-ray test-facility setup. The line diagonally crossing all three chambers shows the track of a high-energy muon passing through all detector parts and even through the iron absorber without experiencing track deflections due to multiple scattering.

---

[1] Owing to the nature of their origin muons being part of the observed cosmic radiation are called "cosmic muons".

Where do those cosmic muons come from? High-energy protons from outer space are virtually bombarding the terrestrial atmosphere. Due to strong interaction between these protons and atomic nuclei of the atmosphere charged pions are produced. In weak decays charged pions decay into muons and the corresponding neutrinos. Many of those muons have an energy high enough to reach the surface of the earth. For horizontal detectors the rate of muons of an energy above 1 GeV is roughly 1 $cm^{-2}min^{-1}$ ([6], p.151). Knowing where the cosmic muons come from, we will turn our attention back on their detection at the test facility.

A layer of 42 scintillation counters, each 90 mm wide, is placed above the upper reference chamber perpendicularly to the drift tubes. Underneath the 34 cm thick iron absorber a second hodoscope consisting of two layers of 38 scintillation counters[2] each is positioned. Combining the information of the hodoscope hits enables to determine the coordinate of the cosmic muons in the direction along the drift-tube wires. Additionally, it yields a time zero for the drift-time measurement. This event time is obtained by averaging over the hit times in two overlapping scintillators in the lower layers which are read out on opposite sides. It therefore is independent of the impact point of the muon in the hodoscope and has a precision of 750 ps.

The purpose of the iron absorber is to harden the energy spectrum of the cosmic muons. The energy spectrum is approximately proportional to $\frac{1}{E^2}$ and peaks at low energies. The iron absorber stops all low-energy cosmic rays and all cosmic muons of an energy below 600 MeV, which has been shown in a simulation with mtgeant-4 (*Figure 2.3*).

Low-energy muons having an energy above 600 MeV experience stronger multiple scattering when passing the iron absorber than high-energy muons. The scattering angle is determined with the aid of a layer of Iarocci tubes placed below the hodoscope. These are read out via 10 mm wide pick-up strips. The cosmic muon spectrum can then, in addition, be hardened by applying a cut on the scattering angle. The scattering angle in the iron absorber is determined by extrapolating the track reconstructed in the lower reference chamber to the plane where the Iarocci tubes are installed. The extrapolated track position can be compared with the hit position in the Iarocci tubes.

Low-energy muons are also subject to multiple scattering in the test chamber and the reference chambers. Therefore further hardening of the muon spectrum is possible by applying another cut on the scattering angle in the chambers as well. The scattering angle in the test chamber is obtained by comparing the slopes of the track reconstructed in the upper reference chamber with the slope of the track reconstructed in the lower reference chamber.

The muons left over after applying the cuts mentioned above are less affected by multiple scattering. This opens up the possibility to use their tracks to deter-

---

[2] 100 mm wide

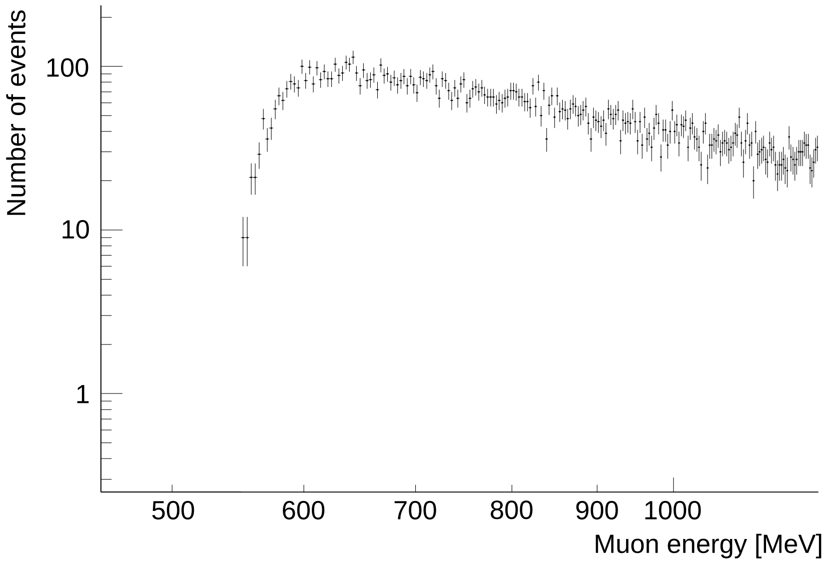

Figure 2.3: Plot of the cosmic muon spectrum after having passed through the iron absorber [13].

mine the geometry of the test chamber.

2.2 Purpose of the Cosmic-Ray Test-Facility

Knowing the parts of the Munich Cosmic-Ray Test-Facility, let us answer the question of what kind of tests and measurements are possible.

The main purpose of the cosmic-ray test facility is the quality control of 88 BOS-type MDT muon chambers which are built at MPI[3] Munich. All of these will be tested at the test-facility prior to installation in the ATLAS muon spectrometer to make sure they fulfill the strong requirements. The ATLAS collaboration has agreed on measuring the efficiency, the noise and the drift-time spectra for each tube. This is done with the setup described in section 2.1. Gas leak rates and leakage currents are also determined.

Apart from the quality control aspect, the Munich Cosmic-Ray Test-Facility offers the possibility to measure the position of the wire-to-wire distance and of the wire-plane distances of the test chamber. Thereby the test chamber geometry is examined closely. It has been shown ([13] and [14]) by comparison of measurements of the cosmic-ray test-facility and the x-ray tomograph that the ATLAS z-coordinate (the “precision” coordinate) of the anode wires and the distance of the tube layers of a test chamber can be determined with an accuracy of 10 μm after a data-acquisition time of 20 hours.

---

[3] MPI is the acronym for Max-Planck Institut.

Geometrical acceptance limits lead to less detected muon tracks passing the drift tubes located on the sides of the test chamber. This problem can be overcome by measurements for which the test chamber is shifted by 50 *cm* to the left and 50 *cm* to the right perpendicular to the anode wires in addition to the measurement where the test chamber is installed centered relative to the reference chambers. Thus the position of all of the anode wires in the test chamber is determined with the same statistics. This opens up the possibility to make these measurements in addition to the standard quality-control procedure foreseen by the ATLAS collaboration for all chambers built in Munich. However, the verification of the geometrical precision of the chambers is only possible with the accuracy mentioned above, if the setup (*Figure 2.2*) is rigid in a sense that all possible chamber deformations and displacements are well below the accuracy limit. This has to hold for the whole data-acquisition time of 20 hours. Therefore the experimental apparatus is installed in an air-conditioned hall. The temperature is stabilized to 19.5^o C with a maximum fluctuation of $\pm 0.5^o$ C[4].

Nevertheless, it is naive to rely on the temperature stabilization to provide sufficient control over the conditions in the experimental environment. The accuracy of a few micrometers within which the relative chamber positions have to be known make alignment monitoring of the three chambers installed at the test facility indispensable. The relative chamber positions have to be known with high accuracy to be able to determine the wire-to-wire distance and the wire-plane distance of the anode wires (the “wire-placement accuracy”) with 10 μm precision. Possible relative chamber movements or chamber deformations would degrade this wire-placement accuracy, which in turn would degrade the intrinsic chamber resolution as explained in section 1.2.2.

Therefore two alignment monitoring systems using different principles have been set up by the author of this thesis. The goal of the alignment systems that were installed is not only to enable to select periods of stability where no deformations and displacements of the muon chambers occurred, but to be able to correct for deformations and displacements in the analysis of the cosmic-ray data. Thus one should be able to use cosmic-ray data acquired during any period of time to determine the anode-wire position and the distance of the tube layers of a test chamber with the accuracy wanted.

Before modelling chamber deformations and relative movements and reconstructing these in chapter 4 the next chapter will introduce the technical concepts of the alignment systems. Their test-facility specific setup is described including all the technical and conceptual problems that had to be solved in order to make the systems work. Of course the individual purpose of each alignment system will be shown in this context.

---

[4] The manufacturer guarantees a stabilization to $\pm 2^o$ C.

Chapter 3

Muon Chamber Alignment at the Munich Cosmic-Ray Test-Facility

Chapter 2 ended with the conclusion that alignment monitoring of the muon chambers installed in the test facility is indispensable. It is technically not feasible to exert enough control over mechanical and environmental parameters to keep the whole setup mechanically rigid within an upper limit of 5 μm for relative chamber displacements over the data-acquisition time of 20 hours.

Nonetheless, the chamber displacements and their individual deformations are expected to be of the order of a few micrometers only because mechanical and environmental stability of the experimental setup were issues handled carefully when planning and building the test facility.

To be absolutely sure that either no chamber deformations and no displacements of the chambers relative to each other occurred during data acquisition or to reconstruct these reliably to correct the cosmic-ray data for them, alignment monitors have been foreseen for the test-facility setup. These systems have to be able to measure relative movements with an accuracy better than 2 to 3 μm depending on the coordinate. Alignment systems fulfilling this requirement were installed, tested and used by the author.

The alignment systems installed make use of different principles to detect movements. They can be separated into an optical and an electrical or, more precisely, a capacitive alignment system. We will now explain the working principle of each system. This will be directly followed by the explanation of the installation procedure and its problems and of course by outlining their solution. The test-facility specific purpose will be made transparent.

3.1 The Optical Alignment System

The optical alignment system makes use of the so called RasNiK[1] system developed for the alignment of the ATLAS MDT muon chambers at NiKhef[2]. This is the built-in optical system monitoring the drift-tube chamber deformations already mentioned in section 1.2.1. This specific use of the RasNiK system is called in-plane alignment and will be explained in section 3.1.2.

For the chamber alignment at the test-facility a test-facility proprietary setup of the RasNiK system is used in addition to the in-plane alignment. This so called "reference" alignment system was designed by J. Elmsheuser and Č. Zupančič and installed by the author. The in-plane and the reference system both use the same basic concept we will now explain.

3.1.1 Basic Concept of the RasNiK System

Figure 3.1 shows the basic concept of the RasNiK system. It consists of three major components: an illuminated coded mask, a lens and a CCD[3] sensor with readout electronics (a "camera"). The CCD video frame is captured by a commercially available video framegrabber card. The digitized CCD response is then stored in a binary file which is used to determine the location of the lens center with respect to the optical axis in this case defined by the centers of the CCD and the mask.

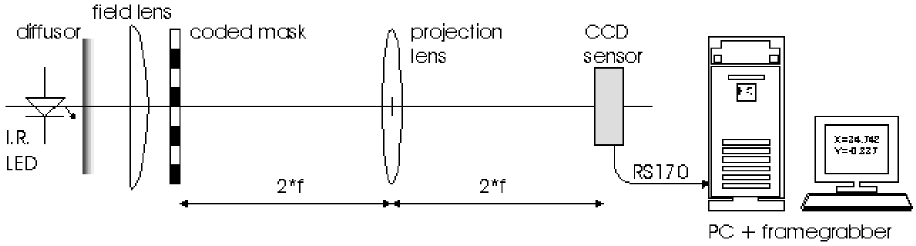

Figure 3.1: Principle of the CCD/RasNiK system [9].

Required to achieve optimal performance is a sharp image of the mask on the CCD. This means the imaging equation

$$\frac{1}{f} = \frac{1}{g} + \frac{1}{b} \tag{3.1}$$

with f being the focal length of the lens, g being the distance between mask and lens and b being the distance between lens and CCD has to be fulfilled.

---

[1] RasNiK is the acronym for Red alignment system NiKhef.

[2] NiKhef stands for National Institute for Nuclear Physics and High Energy Physics, Amsterdam (Netherlands).

[3] CCD is the acronym for charge coupled device.

The position information is encoded in a modified chessboard pattern of the mask (*Figure 3.2*). The idea has a striking simplicity: a simple alteration of square black and white fields make up a "chessboard" in which every ninth row and column contains encoded (by inverting some squares) information allowing the unique identification of the part of the mask registered by the CCD. The total size of the mask defines the maximum misalignment allowed and the number of black/white transitions the accuracy (the more the better) ([9], [15]).

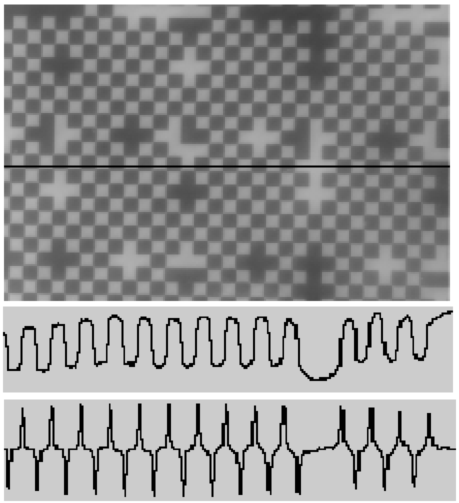

Figure 3.2: Digitized CCD response (0-255) shown on a gray scale (0=black and 255=white. The upper part shows the mask image. The irregularities on every ninth row and column are due to encoded information. The inserts show the digital output and the result of a differential filter (along the horizontal line). This shows the black/white transition localizing power of such a filter [9].

The mask is lit by the so called RasLeD, an array of nine high efficiency IR emitters arranged in a square to illuminate the diffusor in front of the coded mask. It has a light wavelength of 875 *nm* so that the system should operate independently of external light conditions [16].

An infrared filter is mounted in front of the CCD camera for the same purpose. This camera uses a CMOS type sensor with 384 times 287 pixels each having a size of 12 μm^2 [17].

Since the system was designed to measure movements in the micrometer range with high resolution, the intrinsic precision of the mask and the CCD have to be better than 1 μm. This is why the production of these elements relies on the highly precise successive photographic etching of silicon wafers.

An important component of this system is the software for the analysis of the digitized images. The basic algorithm used proceeds as follows: First the black/white transitions between squares are located. Then the minimal distance to an orthogonal grid of equidistant lines is calculated and a χ^2 being the sum of the squares of the minimal distances is defined. By minimizing the χ^2 the five fit parameters - common rotation angle, periodicity and offset in the two directions orthogonal to the optical axis - are calculated.

Through an identification and decoding of the global code information the misalignment in the plane perpendicular to the optical axis is calculated using the two offset parameters. Dividing the periodicity by the size of a basic square on the mask yields the scale factor A which then is used together with the focal length f to calculate the misalignment along the optical axis.

This means the RasNiK system is a genuine 3-dimensional position monitor. We have outlined above that in the plane transverse to the optical axis the misalignment is determined from the part of the mask seen by the CCD. Displacing the lens perpendicularly to the optical axis by d μm is detected as a shift of the mask pattern on the CCD sensor by 2 × d μm for systems with g = b = 2f. An accuracy in this plane better than 1 μm is achieved in actual setups ([9],[19] and [20]).

Along the optical axis the misalignment is determined from the scale factor. For systems with $g = b = 2f$ a longitudinal displacement of ϵ which means e.g. $g = 2f + \epsilon$ and $b = 2f - \epsilon$ yields for the scale factor

$$A \equiv \frac{b}{g} = \frac{2f-\epsilon}{2f+\epsilon} \Rightarrow \epsilon = \frac{1-A}{1+A} \cdot 2f \approx (1-A) \cdot f. \tag{3.2}$$

For actual setups this means a longitudinal accuracy of $0.03 \times f \mu m$ (f in mm) is achieved ([9],[19] and [20]).

Having explained the basic concept of the RasNiK system as well as its components and the achievable accuracy, we will next look at how this system is implemented in the MDT chambers to monitor their deformations (section 3.1.2). Afterwards we will explain how the RasNiK system is used in the reference alignment system (section 3.1.3). Actual measurements and their interpretation are presented in chapter 4.

3.1.2 The In-plane Alignment System - Setup, Purpose, Problems and Solutions

It has already been said that monitored drift-tube (MDT) chambers owe their name to the property of their deformations being monitored after they have left the flat granite assembly table. Chamber sizes ranging from 1.11 m × 1.20 m up to 4.99 m × 2.16 m in the barrel are such that deformations due to gravitational forces have to be taken into account if the chamber is only supported at both ends. This does not mean that deformations due to gravitational forces are the only chamber deformations to be taken into account.

The monitoring is accomplished by the so called in-plane alignment system. It consists of 4 RasNiK monitors[4]. The light rays of those monitors all lie in the plane centered with respect to both multilayers of a chamber and parallel to these ("in-plane"). Figure 3.3 shows a three-dimensional drawing of a typical type of MDT chamber with indicated paths of the light rays.

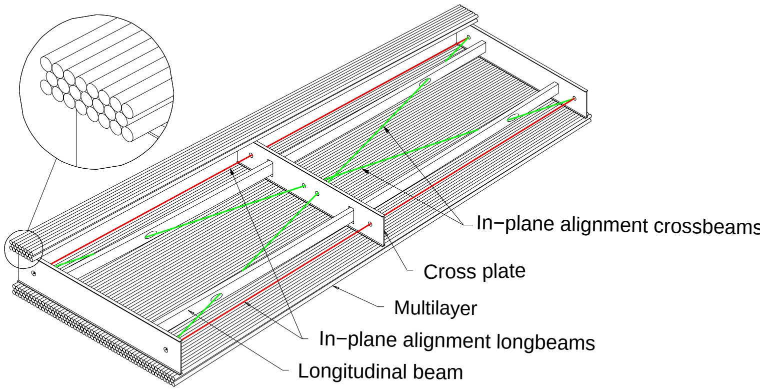

Figure 3.3: Schematic drawing of an MDT chamber. The paths of the light rays of the in-plane alignment system are indicated [9].

Figure 3.4 shows where the optical elements of each of the four monitors are positioned. The CCDs of the in-plane system are mounted to one of the extremal cross-plates, the masks are fixed to the other. The four lenses needed are contained in the middle cross-plate. Although there are four masks and four lenses, only two CCDs are employed because each of them is used twice to subsequently detect the images of two different masks.

The RasNiK monitors of the in-plane system can be subdivided into two basic types: the so called longbeams and the so called crossbeams. In figure 3.4 the light rays running straight along the sides of the MDT chamber (colored red) are longbeams, whereas the light rays diagonally crossing the chamber (colored green) are crossbeams. A channel name is assigned to each RasNiK monitor of the in-plane system. Figure 3.4 follows the common channel naming convention for the in-plane alignment system monitors.

The in-plane system was designed to allow to measure and reconstruct possible deformations of the MDT chambers on the micrometer scale[5]. The implemented layout was optimized to detect deformations caused by gravitational forces, although it is nevertheless sensitive to deformations caused by other effects (i.e. thermal expansion). We will leave it to section 4.2.1 of this thesis to build a model of deformations the parameters of which can be reconstructed.

---

[4] A "RasNiK monitor" is one basic RasNiK system (mask - lens - CCD) as described in the section 3.1.1.

[5] Measurements on the intrinsic resolution of an in-plane system are presented in chapter 4.

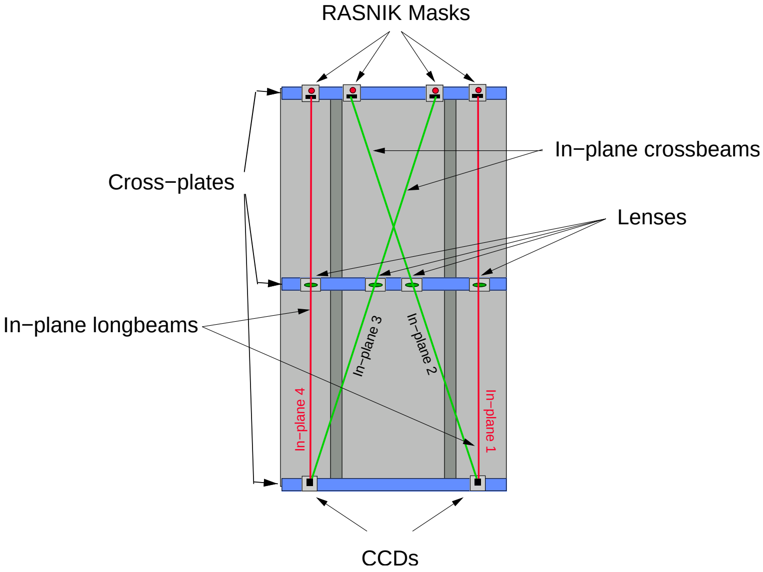

Figure 3.4: Sketch of the in-plane alignment system showing the standard 4-ray scheme.

Apart from some cabling the setup of the in-plane alignment system consisted of defining and initializing a channel for each RasNiK monitor in the software controlling the data acquisition and the image analysis of the RasNiK systems. This software called “Icaras” is a Microsoft Windows program package developed at NiKhef. It allows definition of RasNiK monitor channels which can be switched on and off via channel-multiplexing circuitry connected to the serial port of a Windows-PC. The CCD images of each monitor are captured by a framegrabber card and the digitized image is analyzed by the analysis module integrated in the Icaras program package. The Icaras program allows to define channel sequences and to specify time intervals at which data is acquired for all channels of a predefined sequence in the specified order.

A standardized readout software for the whole slow-control system of the cosmic-ray test-facility monitoring the chamber temperatures, the MDT and Iarocci tube gas mixture, the MDT-gas pressure and the humidity inside the test facility in addition to the alignment monitoring is planned and has in parts already been realized. This readout software is developed for Linux operating systems. Therefore the optical alignment data acquired with the above mentioned Icaras Windows program have to be transferred to the slow-control data-acquisition system running Linux.

Attempts to set up software controlling the data acquisition and the image analysis of the RasNiK monitors on a the Linux-based slow-control PC[6] were unsuccessful. The Linux software for RasNiK data acquisition and image analysis

---

[6] Linux software for RasNiK data acquisition and image analysis is developed at the University of Freiburg.

crashed frequently, probably due to crashes of the Linux framegrabber driver. Measurements made with the Linux setup were absolutely not reproducible: before and after a crash the position measurements of the same RasNiK monitor yielded completely different values. This also explains why measurements made with the Linux setup did not yield the same results for the same RasNiK monitor channels as measurements made with the Windows software. No systematic offset between the measurements of both systems could be determined. These are reasons to run the data-acquisition software of the optical alignment system in a Windows environment.

This decision additionally has the advantage that the data-acquisition software intended for RasNiK systems by the developers of the hardware can be used. The Icaras program as well as the framegrabber driver work stable over long periods of time. Calibration data for each of the RasNiK monitors of each chamber measured during the chamber assembly on the flat granite table at MPI Munich is (and should be) directly comparable to the readings of these RasNiK monitors at the test facility, since the same Windows-based software is employed.

The disadvantage of the decision is obvious: data acquired with the Windows system has to be transferred to the Linux-based slow-control system to be integrated in a homogeneous slow-control data flow. Through the setup of a Samba-server[7] the possibility to write all data measured with the Icaras Windows program directly to the slow-control Linux-based PC was opened up.

All slow-control "event" data should have time stamps independent of the computer system the software of each individual slow-control system is running on. For that reason it is important to synchronize both the Linux-based and the Windows-based slow-control computer systems by running a timeserver routine.

Although running the data-acquisition and image analysis software on the Windows-based computer system proved to be more stable as far as the reproducibility of measurements and the reliability of the framegrabber driver are concerned, in the beginning the Icaras software crashed frequently. A crash of the Icaras software normally led to a system lock-up which could only be resolved by rebooting the computer system. Unlike the situation after crashes of the framegrabber driver when using the Linux-based system the Windows software yields RasNiK monitor readings for each channel before and after a crash which are comparable to each other.

The failure of the software was correlated to the time at which the sun began to shine onto the chambers through the test facility windows. It had previously been observed that stray as well as direct light leads to a degradation of the CCD image quality through loss of contrast up to the point where the features of the black/white transitions become so feeble that these can no longer be correctly located by the image analysis algorithm described above (see section 3.1.1).

---

[7] Samba is a Linux program package providing seamless file and print services to e.g. Windows clients.

When the analysis algorithm is no longer able to locate the black/white transitions needed to decode the position information, it should write an error code to the output file and continue with the analysis of the next RasNiK monitor image. This is what the Icaras program does, but if all the grabbed images of all monitors cannot be analyzed the program crashes within a period of minutes. This problem was reported to the developers of the Icaras program at NiKhef together with sample images saved before the analysis leading to the program failure. It turned out to be a known problem that was being worked on. Recent versions of Icaras are not as sensitive to this effect any more, although crashes will eventually occur if images cannot be analyzed for long periods of time. This means all alignment systems based on the RasNiK principle have to be shielded from direct as well as from stray light.

A series of tests was conducted with the aim to find out which parts of a RasNiK system have to be shielded from external light. The outcome is not surprising: in principle only the CCD camera has to be shielded in such a way that most of the light reaching the CCD sensor is emitted by the RasLeds. Although the CCD is most sensitive for near infrared wavelengths it is nonetheless sensitive to all wavelengths in a range from 400 *nm* to 1100 *nm* as can be seen in figure 3.5.

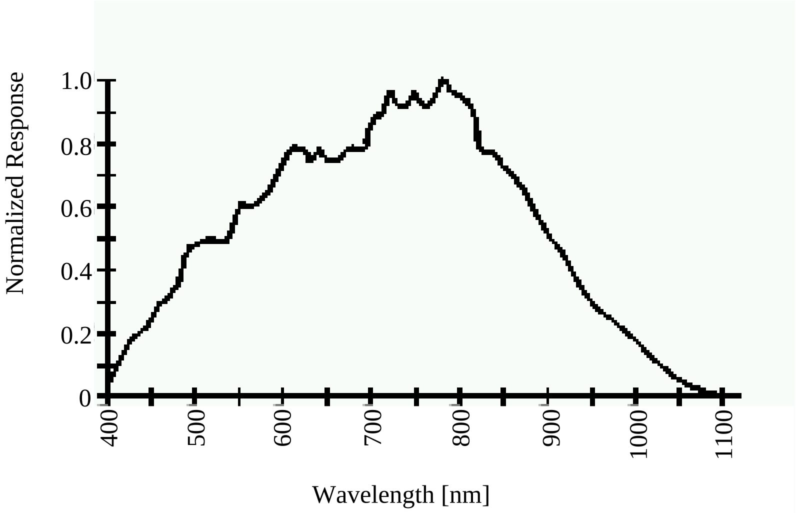

Figure 3.5: Spectral response of the CMOS chip of the CCD camera (RasCam) in dependence of the wavelength [18]. Although the sensor is most sensitive in the near infrared regime, it detects light of wavelength from 400 *nm* up to 1100 *nm*.

The sensitivity of the CMOS[8] sensor to a wide range of wavelengths causes direct as well as stray light, no matter if natural or artificial, to produce a high

---

[8] CMOS is the acronym for complementary metal oxide semiconductor.

background. Hence the signal-to-noise ratio becomes small and the contrast of the image of the mask on the CCD degrades rapidly.

Covering the sides of the MDT chambers installed in the test facility solves this problem. Only half of the side of one chamber needs to be completely covered between its multilayers, namely the part between the middle crossplate containing the lenses and the outer crossplate containing the CCD cameras. Styrofoam sheets which had been "coated" with black cardboard on one side were employed for this purpose. They are so lightweight that they can simply be taped to the side of an MDT chamber. If need be, they can easily be installed as well as rapidly removed.

After the installation of the light shielding for the chambers the data acquisition of all in-plane RasNiK monitors with the Icaras program has been running stable over periods of days. In future it would be desirable to install lightweight aluminum tubes between the lenses and the CCDs of the in-plane system to provide shielding from other light sources than the illuminated masks. This would have the advantage of being a permanent installation since at the moment the styrofoam plates have to be removed for all chambers each time the test chamber is replaced or needs to be moved.

For precise muon track point measurements of the MDT chambers the chamber sag along the direction of the anode wires needs to be adjusted with the aid of the in-plane system. Even on the perfectly flat granite assembly table the anode wires of each drift tube of a chamber have a maximum sag of about 200 μm along a tube because they are subject to gravitational forces. The drift distance-drift time relation (r-t relation) though depends on the concentricity of the anode wire of a drift tube with respect to the tube walls. Therefore the whole chamber and thereby each drift tube has to be adjusted in such a way that its sag corresponds to the anode wire sag. This guarantees concentricity of the signal wire along each tube.

The possibility to adjust the chamber sag along the tube direction is implemented into the design of the MDT chambers. Upon construction a set of calibration RasNiK readings for each chamber is recorded while the chamber is still lying on the granite table. On the assembly table the chamber sag should be zero, whereas the anode wire sag is already about 200 μm as stated above. The minute a chamber is installed at the test facility, the sag of the chamber has to be adjusted so that the middle crossplate is positioned 200 μm below the extremal crossplates.

For this purpose the in-plane RasNiK readings of the chamber installed are measured and compared to the calibration data from the assembly table. The sag of the chamber is then adjusted with the aid of two bolts connecting the middle crossplate to the longitudinal beams on each side of the spacer structure until

$$\frac{RasNiK_{measured} - RasNiK_{calibration}}{2} \approx -(200 \pm 50)\mu m \qquad (3.3)$$

holds true. The factor $\frac{1}{2}$ in equation (3.3) is needed because displacements d of the lens perpendicular to the optical axis of optical systems like the in-plane system with $g = b = 2 \cdot f$ are detected as shift of the mask pattern on the CDD of $2 \cdot d$. The adjustment of the sag compensation will have to be done for each test chamber installed in the cosmic-ray test-facility in future.

Data giving evidence for the functioning of the in-plane alignment system is presented in chapter 4. There an approach to calculating single chamber deformations using that data is offered, too.

3.1.3 The Reference Alignment System - Setup, Purpose, Problems and Solutions

After having explained the setup, purpose, problems and their solutions of the in-plane alignment system, we will now focus on the reference alignment system. This system was designed to monitor possible relative chamber displacements between the upper and lower reference chamber due to e.g. temperature fluctuations. The setup of the reference system for both ends of the reference chambers is shown in figure 3.6.

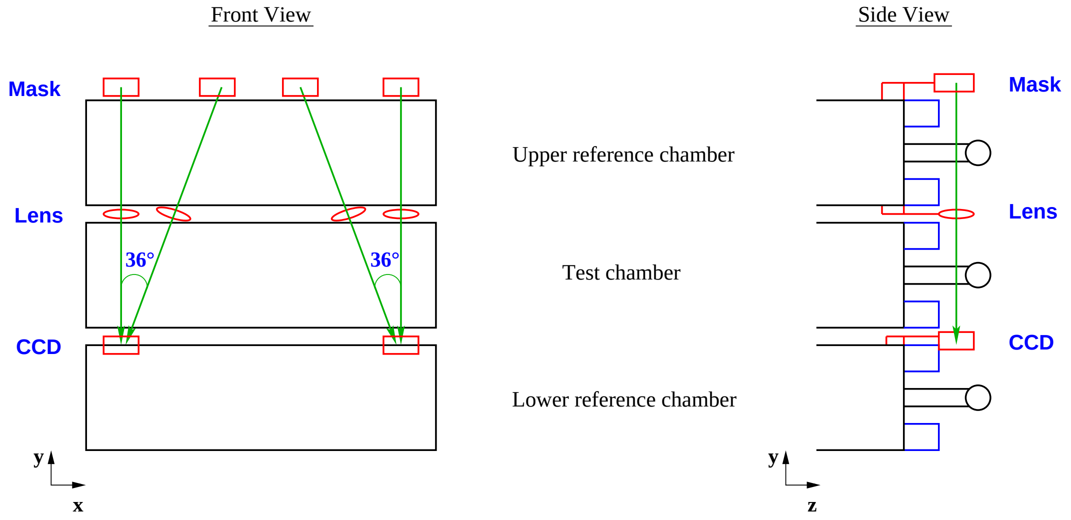

Figure 3.6: Sketch of the reference alignment system which allows to monitor relative displacements between the upper and lower reference chambers.

The reference system again makes use of the RasNiK principle described in section 3.1.1 by using a total of eight RasNiK monitors (four on each end of the chambers). The support structures of the coded masks and the lenses are screwed to small aluminum "feet"[9] which are glued to the upper and lower multilayer of

---

[9] These "feet" of 5 cm length and 1 cm width are shaped to fit right between two adjacent drift tubes.

the upper reference chamber. The support structures of the CCDs are in turn screwed to aluminum feet glued to the upper multilayer of the lower reference chamber (compare to the right hand side of figure 3.6).

The RasNiK systems arranged perpendicular to the multilayer planes are sensitive to relative displacements between the chamber corners in x- and z-direction. The achievable accuracy of these measurements is about 2-3 μm. In analogy to the in-plane system we will call these RasNiK monitors “reference longbeams”.

The RasNiK monitors tilted by 36^o with respect to the reference longbeams are the so called “reference crossbeams”. The choice of the angle was ruled by the need to allow passage of the light beam unobstructed by the chamber support structures. These monitors were implemented into the design of the reference alignment system because they offer the possibility to detect relative displacements between the reference chambers in the y-direction. Displacements δ in y-direction are detected by the reference crossbeams as a relative chamber displacement in x-direction by $\delta \cdot \sin 36^o \approx \frac{1}{2} \cdot \delta$. Measurements made with the reference crossbeams should thus be accurate to about 4 μm.

In order to install the system the above mentioned aluminum feet had to be glued onto the chamber multilayers at the positions foreseen. Together with J. Elmsheuser the author tested a total of four different types of compound glues. Pieces of damaged drift tubes were arranged in such a way that they simulated a multilayer surface. The part of the tubes the aluminum foot was to be glued to as well as the aluminum foot itself were cleaned with acetone in order to get rid of any dirt or fat. For each gluing the components of the glue were mixed anew to guarantee that it had not been setting yet. The setting time of the different glues ranged from hours to about one minute. After the gluing the feet were not subjected to mechanical stress of any kind for 24 hours. After that time it was tried to rip the feet of the tubes by employing brute force. Apart from one particular type of glue a lot of effort and a big screwdriver were needed to loosen the feet.

A glue having a setting time of about ten minutes was chosen for the gluing of the mounting feet to the reference chambers. This glue was the best compromise between setting reasonably fast, being more than sufficiently strong after not having been exposed to mechanical stress for 24 hours and being viscous enough not to drip down if the gluing had to be done from underneath (i.e. for the feet of the lenses glued to the lower multilayer of the upper reference chamber).

Since two mounting feet are needed per support structure, these were screwed to a small aluminum sheet with holes precisely drilled so the distance between the holes and thereby between the two feet was such that they fit precisely between two adjacent tubes leaving one space between tubes open. The aluminum sheet guaranteed the fixed geometry during the gluing process in addition to providing a smooth surface to which the feet could securely be screwed. It allowed to apply pressure to both aluminum feet of one gluing at once by applying pressure to the aluminum sheet itself. The gluing procedure for the actual gluing to the chambers exactly corresponds to the procedure of the test gluings.

Subsequent to the installation of the reference chambers at the test facility the support structures for the optical elements needed for the reference RasNiK system were installed. The support structures are custom made out of aluminum in order to be as lightweight as possible while still providing good mechanical stability.

The support structures have to be assembled prior to screwing them to the mounting feet because they consist of multiple parts. They were carefully designed so that the imaging equation (3.1) is fulfilled for each reference RasNiK monitor after all of the elements are fixed to the chambers. Therefore they have to be precisely manufactured. However, instead of being CNC[10] machined most of the parts were made from thin bent aluminum sheets. Though the bending was done with care small variations of the dimensions of the parts made it difficult to assemble some support structures.

For the lens support structures of the reference crossbeams the part of the support structure supposed to contain two lenses could not be assembled because the designer had not thought of leaving enough space for the heads of the screws which were supposed to hold the assembly together. In close cooperation with the machine shop the problem was overcome by thinking up a small fix for the lens support allowing its assembly.

The mechanical precision of the supports caused further problems. When the support structures were mounted to the aluminum feet, some of the feet just sprang off the chamber when the screws were tightened. Of two aluminum feet per support structure only one mounting foot showed this behavior. Small angles between both sides of a support structure screwed to the smooth surface provided by the feet lead to an enormous mechanical stress applied to either one of them.

The problem was solved by refinishing the surface of both sides of all support structures to be even enough and re-gluing the unglued foot. To ensure the wanted geometrical arrangement, this foot was fixed to the refinished support structure which in turn was screwed to the foot which remained on the chamber. This procedure has the advantage that one can be sure that the support structure can be screwed to the mounting feet without tearing these feet from the chamber after the re-gluing of the second foot since the geometry remains exactly the same.

When all optical elements were installed at their respective positions, the problem encountered next was the lack of sharpness of the reference longbeams and the fact that no mask images could at all be detected for some of the crossbeams. Apparently the imaging equation was not fulfilled in the case of the longbeams and the geometry was not right in the case of the crossbeams. Through the use of washers the mask-lens distance of the reference longbeams was adjusted in

---

[10] CNC is the acronym for <u>c</u>omputer <u>n</u>umerically <u>c</u>ontrolled.

iterative cycles until a sharp and stable image could be detected on the CCD.

The adjustment of the crossbeams was not as easy. For the crossbeams which did not yield an image the author found out that an image could be detected by the CCD if the mask was tilted towards a position perpendicular to the optical axis of the RasNiK monitor[11]. Again an iterative empirical procedure led to detectable mask images of all reference crossbeams.

Figure 3.7 shows an example of mask images for a long- and a crossbeam of the reference alignment system captured by the framegrabber. The mask image of the reference longbeam (left) shows good sharpness and contrast throughout the whole image area. In comparison to that only the left hand side of the mask image of the reference crossbeam (right) is as sharp and offers as much contrast.

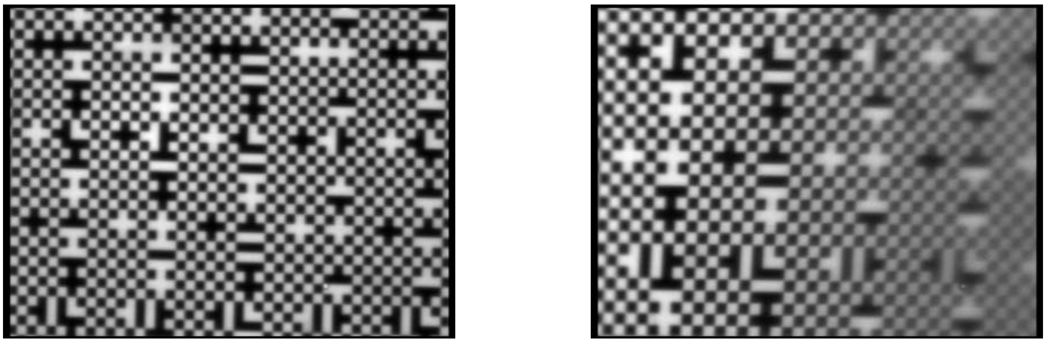

Figure 3.7: RasNiK mask images of the reference alignment system captured by the framegrabber. Left: Reference Longbeam. Right: Reference Crossbeam.

This effect is caused by the geometry of the setup. The lenses of the crossbeams are all tilted from a horizontal position to a position perpendicular to the optical axis of the RasNiK monitor. Both the CCD and the illuminated mask should be installed in a perfectly horizontal position which at least for the CCDs is the case. Simple geometrical optics show that the effect seen in the crossbeam images is due to the limited depth of focus of the reference crossbeam monitors. The limited depth of focus causes about one third of the image to be reasonably sharp whereas the rest of the image becomes more and more blurred the further one moves away from that area.

The next question which automatically arises is whether mask images such as the one shown on the right hand side of figure 3.7 can actually be analyzed reliably by the analysis module of the Icaras program. Fortunately, they can. Only one block of the coded chessboard pattern of 9 × 9 black or white squares has to be used to decode the position information [15]. Figure 3.7 clearly shows that at least one such block can be detected by the CCD camera.

---

[11] As in section 3.1.1 the optical axis of a RasNiK monitor is defined by the centers of the mask and the CCD sensor.

In analogy to the problems of the in-plane system the reference alignment system shows the same sensitivity to direct or stray light reaching the CCD cameras. Therefore they have to be shielded from as much of the unwanted light as possible. For this purpose the author designed and built little boxes out of black cardboard. Each of the 14 cm high boxes has a cutout of 1.4 $cm\times$ 2.0 cm at the top to permit the passage of the reference longbeams and a cutout of 2.0 $cm\times$ 2.7 cm on one side to allow the passage of the crossbeams. Each CCD sensor can now be shielded with the aid of these boxes that are simply placed over the CCD camera. The mask images of the reference system shown in figure 3.7 already make use of the light shielding described here.

Chapter 4 is dedicated to show data acquired with the reference as well as with the in-plane alignment system. There the measured intrinsic resolution of both systems is compared. Data proving the functioning of the reference system are presented and an approach to calculating relative chamber displacements between the reference chambers is explained in section 4.3 of that chapter.

The reference system dealt with in this paragraph only monitors any movements of the reference chambers relative to each other. The following section 3.2 will show how to monitor the position of the test chamber with respect to the upper reference chamber and thus with respect to the position of the lower reference chamber. System-wise a different approach is followed than for the reference chamber alignment.

3.2 The Capacitive Alignment System

The previous section 3.1 introduced the optical alignment system. This system is used to monitor relative displacements between the two reference chambers (compare to figure 2.2 and paragraph 3.1.3) and individual chamber deformations (see paragraph 3.1.2).

What though happens to the test chamber? How can one tell whether it stays in place or whether the reference chambers move relative to it? For this purpose a commercially available system designed by Capacitec, Inc. is employed. It relies on capacitive probes specifically intended for the measurement of gaps.

3.2.1 Basic Concept of the Capacitec$^{\text{TM}}$ System

To understand the basic concept behind capacitive measurement of gaps let us have a look at a simple model : Two parallel plates separated by a distance d, each having a surface area A can be seen as a parallel-plate capacitor of the capacitance $C = \epsilon\frac{A}{d}$. Knowing the capacitance allows to infer the distance d. This is the basic concept of capacitive displacement measurement used by Capacitec for their “non-contact displacement measurement”.

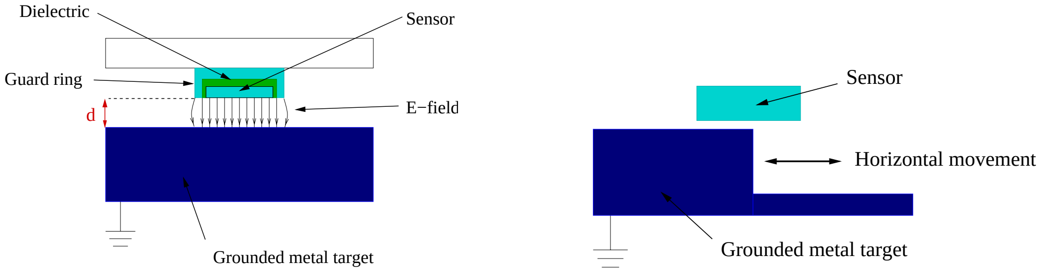

Figure 3.8: Concept of the capacitive distance measurement. Left: Measurement of vertical displacements. Right: Measurement of horizontal displacements.

The capacitance is measured by connecting it to a alternating current source of constant current I and measuring the voltage drop across the capacitor. The r.m.s. voltage is proportional to the distance d. This r.m.s. voltage is the output signal supplied by the amplifier electronics of the Capacitec system. It is used to determine the distance d of the parallel plates (see figure 3.8 (left)). An accuracy of about 1 μm is achieved for vertical measurements. How this is done will be shown in chapter 5.2.1.

Although the application the capacitive probes were designed for is the measurement of vertical displacements between a sensor and a grounded metal surface outlined above, it is additionally possible to measure horizontal displacements with the same probes by skillfully choosing the geometry of the grounded metal piece.

This idea originates from a group at the L3-experiment at LEP which used capacitive probes produced by Capacitec to monitor the stability of the relative alignment between the silicon microvertex detector and the time expansion chamber of the L3 detector [25]. The choice of the geometry of the grounded target is simple: a step-like geometry like the one shown on the right hand side of figure 3.8 allows to detect horizontal movements.

How exactly is this done? As already said a capacitive probe is placed over the edge of a grounded metal step of height $D - d$ (*Figure 3.9*). The vertical distance between probe and target is d. If we let $A(\xi)$ be the part of the surface area of a probe with radius R which is located over the step itself and let ξ be the normalized displacement of the probe center with respect to the edge of the step, this yields

$$A(\xi) = \frac{1}{2}\pi R^2 + R^2 \left[\arcsin\frac{\xi}{R} + \frac{\xi}{R}\sqrt{1 - \left(\frac{\xi}{R}\right)^2} \right]. \tag{3.4}$$

The capacitance of this setup is the sum of two capacities: the capacity of the sensor part located over the step itself (left part of the sensor shown on the right hand side of figure 3.8) and the capacity of the sensor part located over the base

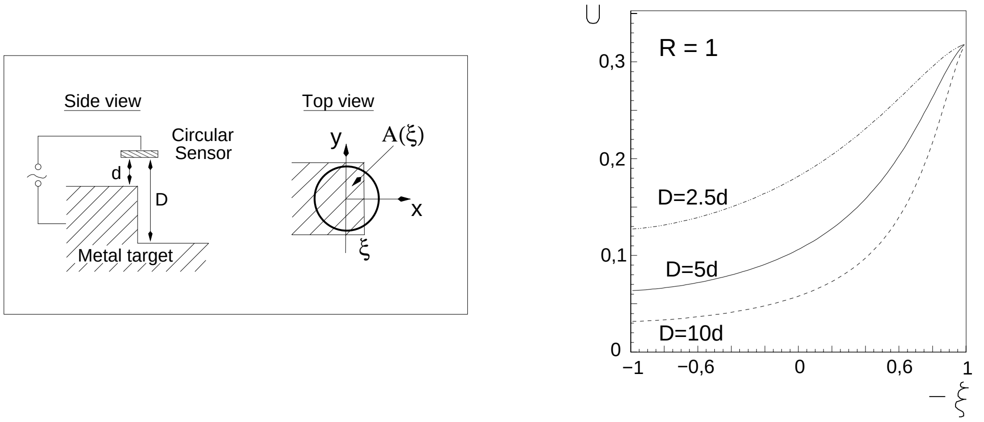

Figure 3.9: Horizontal displacement measurement with capacitive probes. Left: Schematic drawing of the underlying idea. Right: Expected dependence of the sensor voltage on the sensor position over the edge of a metal step [13].

of the grounded metal step:

$$C = \epsilon \frac{A(\xi)}{d} + \epsilon \frac{\pi R^2 - A(\xi)}{D}. \tag{3.5}$$

The dependence of the output voltage U on the normalized displacement ξ of the probe center with respect to the edge of the step is visualized on the right hand side of figure 3.9. Curves are plotted for three steps of different heights $D - d$. For $\xi = -1$ the sensor surface is completely located over the step itself, for $\xi = 1$ it is completely located over the base of the step. The plot shows that the slope of the voltage curves depends on the height of the step: the higher it is, the steeper the slope. It was agreed on to choose $D = 5d$ as the nominal height of the metal steps employed at the test facility.

Since the signal output of the amplifiers is not a capacitance but a voltage which is proportional to $\frac{1}{C}$, the sensitivity of the probes is maximal in regions where relative capacitance changes are largest. This region is reached when only a third of the sensor surface is located over the step. Probes used for the measurement of relative horizontal displacements between the test chamber and the upper reference chamber at the test facility are nominally placed in that position. With the setup chosen horizontal displacements can be measured with an accuracy better than 3 μm. This will be shown in chapter 5.2.2.

Before we have a look at how the capacitive alignment system is set up at the test facility, let us make some concluding remarks about the sensor. The left hand side of figure 3.8 gives some insight into the structure of the whole probe. It consists of the sensor itself embedded in a dielectric which in turn is embedded in the so called “guard ring”. The purpose of this ring is to provide a better homogeneity of the electric field by lessening boundary effects[12]. These are normally not negligible and are caused by the finite surface of the sensor itself (meaning we are talking about a parallel-plate capacitor of finite dimensions which is subject to boundary effects).

Apart from lessening the influence of boundary effects and thereby enlarging the "effective" sensor surface the guard ring acts as a shield for the back side of the sensor.

3.2.2 The Capacitive Alignment System - Setup, Purpose, Problems and Solutions

Now we know how capacitive probes may be used to measure vertical and horizontal displacements. Next, let us have a look at the setup of the capacitive alignment system at the test facility where it is used to monitor the relative displacements between the test chamber and the upper reference chamber.

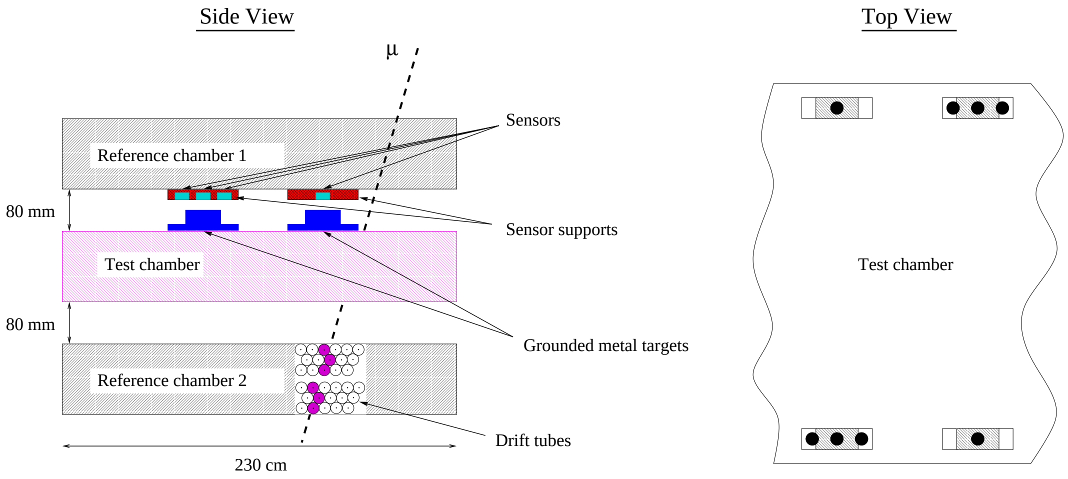

Figure 3.10: Schematic drawing of the setup of the capacitive alignment system used to monitor relative displacements between the upper reference chamber and the test chamber.

Figure 3.10 shows where the probes and the corresponding grounded metal targets are placed. The probes of a diameter of $7\ mm$ have a nominal vertical distance of $4\ mm$ to the corresponding target[13]. The probes are fixed to a plexiglass support block. These supports are screwed to little aluminum "feet" glued to the upper reference chamber. The metal targets are simply put on the test chamber directly underneath the sensor supports and centered with respect to these supports.

---

[12] The boundary effects cause the signal output of the system to be only approximately linear.

[13] The choice of the nominal vertical distance will be made clear in chapter 5.

Two single sensors located on one diagonal are used to determine the vertical distance between the test chamber and the upper reference chamber. The two remaining sensor triplets on the other diagonal are used to measure the vertical distance between the sensor in the middle of each triplet and the metal target. This distance is then used in the calculation of the horizontal displacements between the chambers through the use of the voltage output of the sensors located over the edges of the metal step. The method developed by the author which is used to determine the vertical and horizontal displacements between the test chamber and the upper reference chamber is explained in chapter 5.

Knowing the setup and the purpose of the capacitive alignment system, we will have a close look at the setup-specific components to show which problems were encountered and solved when setting up the system.

The metal targets are electrically isolated from the chamber they are placed on. Little aluminum "feet" of 5 cm length and 1 cm width are screwed to the bottom of the targets on each side. These "feet" were specifically manufactured to fit right between two adjacent drift tubes and thus allow to precisely place the targets centered underneath the sensor supports. The weight of the steel targets is big enough to consider their position as fixed once placed on the test chamber. In order to achieve the precision wanted these steel targets are CNC machined.

It is important to provide a proper grounding connection for the targets. The author's experience gained when working with the capacitive probe calibration stand[14] revealed this known but easily forgotten fact. Consequently, ground wires were attached to the targets and connected to the ground connector of the amplifier electronics rack.

The probes are so called button probes with a sensor diameter of 7 mm. They have to be securely fixed to a sensor support. This support is CNC machined out of plexiglass in order to guarantee the geometry described in section 3.2.1. The plexiglass support blocks contain cutouts into which the probes are placed.

To hold the probes in place different methods of fixation have been tried. Initially double-sided adhesive tape was thought to be a good choice, since it allows to easily remove the sensors from their supports while seemingly providing sufficiently good fixation. The author tested different types of double-sided tape. Although all of them initially allowed to fix the probes to the sensor supports, probes became unglued from their support after a period of weeks. One double-sided tape seemingly worked well but the author was not willing to take up the risk of sensors falling out of their supports after longer periods of time.

The author's choice was to fix the sensors to their supports by gluing them to those with composite glue. It was inspired by the experience of the L3 alignment group which also used a composite glue.

The main disadvantage is that probes cannot be easily replaced in case of their failure. For the single sensor supports it is no big problem to replace the

---

[14] See chapter 5.1.

whole support including the sensor, for the triplets, however, this cannot be easily done. Still, the probability of a sensor to fail is not very high. Should a failure occur nonetheless, it is still possible to unglue it from the support because at temperatures of about 200^o C the glue becomes fluid once again. Mechanical fixes are also possible and have been thought of. Hopefully no probe failure will occur during the operation time foreseen which should hold true under normal circumstances.

The advantages of permanently gluing the probes to their support are evident. If measurements have to be precise on the micrometer scale, the probes should be fixed in such a way that they do not move compared to that scale. Using epoxy glue, this can undoubtedly be accomplished. The glue solves another problem: It was impossible to fix some probes to their support in just one well defined position using double-sided adhesive tape. Some of the cutouts in the machined support blocks didn't have a smooth enough surface to allow it. Instead of having to order new support blocks machined with higher precision or more care, the glue allowed to smoothen the uneven surface in some cutouts. This procedure results in the probes being placed in one well-defined position, not moving on a micrometer scale, guaranteeing a maximum mechanical stability for the duration of the experiment.

A prerequisite for calculating the relative displacements between the test chamber and the upper reference chamber from the sensor output voltages is to correlate these to vertical and horizontal displacements by means of calibration data previously recorded. It was one of the author's tasks to calibrate the capacitive sensors to make actual displacement measurements possible. The calibration procedure is described in detail in chapter 5. We will conclude this chapter by pointing out another problem detected and solved, linking operation and calibration of the capacitive probes.

Originally, it was intended to fix the capacitive probes to their respective supports once and then to use these supports containing the fixed probes for calibration in the capacitive probe calibration stand as well as in the actual experimental setup without ever changing the support (and thus having to unglue and re-glue the probes). However, certain reasons made it necessary to change the geometry of the sensor supports used for the experimental setup (shown in figure 3.10).

This led to the situation that the supports designed for use in the experiment could not be installed in the calibration stand. The step of the metal target used in the calibration stand was now too wide, too. A gluing and ungluing of sensors to different supports for calibration and actual measurement would have been necessary. Thereby reproducibility of the calibration would have been sacrificed because the sensors cannot be fixed reproducibly to different supports. Also, one would have had to rely on methods to fix the probes allowing easy removal of these. As already pointed out above, it would have proven to be difficult to find a way to fix the probes mechanically stable on the micrometer scale that allows for easy removal of the probes at the same time.

The author solved the problem by redesigning the support blocks used in the experimental setup so that these could be installed in the calibration stand and in the experimental setup without changing the actual sensor arrangement in the supports. This opened up the possibility to permanently glue the probes to the sensor support and to repeat the calibration any time with good reproducibility. The geometry of the metal target of the calibration stand was adapted to the geometry used in the experimental setup. Since a new target had to be machined, the author opted for stainless steel as the target material avoiding the problem of degradation of the precisely machined surfaces and edges by rust.

Chapter 5 shows the reader how the calibration of the sensors is actually done, what the calibration data looks like and what algorithms were developed to analyze it. The precision achieved with these algorithms is shown explaining the choice of the nominal vertical distance between probes and targets.

Chapter 4

Data Analysis of the Optical Alignment Systems

Outlining the setup and the goals of the Munich Cosmic-Ray Test-Facility in chapter 2 revealed the need and the importance of monitoring the relative alignment of the muon chambers installed at the test facility. Chapter 3 then explained the working principle and setup of the alignment systems used. Knowing the need for as well as the purpose, principle and setup of these alignment monitoring systems this chapter will present data measured with the optical systems.

Let us recall that the optical alignment system can be subdivided into the in-plane system of the MDT chambers and the reference system set up at the test facility. Monitoring the geometry of each chamber is the task of the in-plane system. The reference system is used for the relative alignment monitoring of the upper and lower reference chamber.

Starting out with the presentation of a method to determine the intrinsic resolution of each of the installed RasNiK monitors, section 4.1 will also present results gained with that method and compare these to measurements made at NiKhef.

Analysis of the in-plane system data is explained in section 4.2. The chapter will conclude with the presentation of the analysis of data acquired with the aid of the reference system in section 4.3. A model of possible chamber deformations or displacements is used in both sections to reconstruct the parameters of those.

4.1 Intrinsic Resolution of the Optical Alignment Systems

To determine the intrinsic resolution of a RasNiK monitor in the direction transverse or longitudinal to its optical axis[1], in principle two different methods can be used.

The most simple and intuitive method is to scan the position of one of the optical elements[2] of a monitor in one direction (e.g. transverse to the optical axis) and to fit a straight line to the position reconstructed from the mask image in dependence of the position set for the optical element scanned. The residuals of this fit are a measure for the accuracy of the reconstructed position and thereby for the resolution of the system. In addition to yielding the resolution this method has the advantage that the linearity of the system is tested at the same time [19].

It is neither possible to move any of the optical elements of any of the RasNiK monitors of the in-plane nor of the reference alignment system in well-defined steps. Therefore the first method cannot be applied to determine the intrinsic resolution of the RasNiK systems installed. Nevertheless the resolution can be determined by repetetively acquiring images while all optical elements of one monitor remain in their fixed position. This so-called “multiple image” method has already been used during the development of the RasNiK system (see [19] and [21]).

The r.m.s. values of the distributions of the reconstructed positions are a measure for the resolution of the monitor for displacements in different directions if the setup used is mechanically stable for the time of the resolution measurement. The advantage of this method over the first one is that it depends neither on the setting accuracy of the element position (normally about 1 μm) nor on the errors caused by mask or lens[3]. Resolutions determined with this method describe the intrinsic accuracy of the RasNiK system as such including the synchronization accuracy of the framegrabber[4] and a possible jitter of the grabbed mask image caused by thermal fluctuations of the air[5].

In this thesis, the second of the methods described was employed to determine the intrinsic resolution of the alignment system monitors. Figure 4.1 shows an example of the distributions of the reconstructed positions for the x-, y- and z-coordinate illustrating the “multiple image” method.

---

[1] As in section 3.1.1 and 3.1.3 the optical axis of a RasNiK monitor is defined by the centers of the mask and the CCD sensor.

[2] Mask, lens or CCD

[3] The precision of the mask is about 0.1 μm and estimates of the lens aberration predict a contribution of less than 0.5 μm [19].

[4] The accuracy of the framegrabber leads to an error of the measurement of less than 0.2 μm [19].

[5] The thermal fluctuations of the air contribute 1-5 μm to the achievable precision, depending on the setup [19].

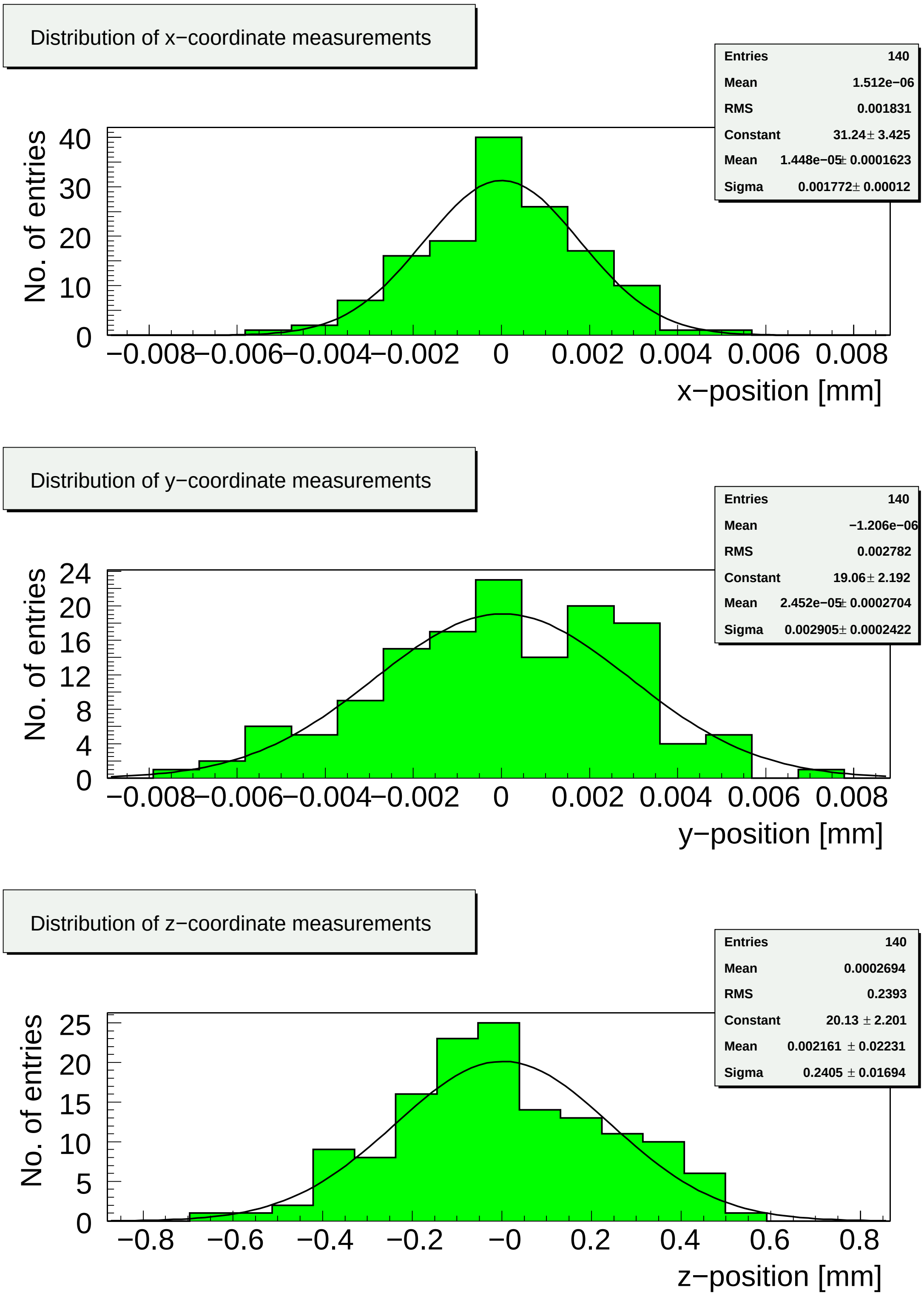

Figure 4.1: Distribution of the reconstructed positions of multiple images used to determine the intrinsic resolution of a RasNiK monitor. Sample data for one of the reference longbeams (Reference longbeam 1).

In order to determine the resolution with the "multiple image" method 140 subsequent images were grabbed and analyzed for each channel of the reference system and for the in-plane system of the chambers installed at the test facility. To acquire and analyze 140 images a maximum time of 10 minutes ($< 4.3\ s$ per image analysis cycle) is needed when running Icaras version 4.5 on a Windows NT 4.0 PC with an AMD K6/2, 400 MHz processor[6]. The data-acquisition time of 10 minutes per channel is such that the whole setup can be regarded as being mechanically stable. It is important that this hypothesis is true because otherwise real deformations or displacements of the chambers would degrade the resolution measurement.

To obtain data plots like the one shown in figure 4.1 the mean value of the 140 position measurements is calculated for the x-, y- and z-coordinate measurements. This calculated mean value is then subtracted from each of the 140 measurements for x, y and z and the data gained this way is filled into histograms. The subtraction of the mean values from all of the measurements for each coordinate causes the plotted distributions to be centered around zero as can be seen in figure 4.1. In order to make it easier to visually compare the distribution for the x- and y-coordinate the abscissa was fixed for both plots and the binning is the same. This cannot be done for the z-coordinate measurement, since the expected resolution is about two orders of magnitude worse.

The distributions for each of the three coordinates are then fitted by a χ^2 fit with a Gauss function in order to determine the intrinsic resolution. The mean value of the fit function should be in good agreement with zero and the sigma of the Gaussian distributions is taken to be the intrinsic resolution measured with the "multiple image" method as described above. As can be seen from figure 4.1 the sigma and the r.m.s. values agree very well in all cases indicating very stable conditions during the measurements.

Before we take a look at the intrinsic resolutions determined with this method let us have a look at a small but important detail of the analysis. Data is shown for the z-coordinate which as a matter of fact is not directly measured with a RasNiK system. Section 3.1.1 explained that one of the five fit parameters of the χ^2 fit used to determine the mask displacement is the periodicity of the black/white transitions of the mask image. It stated that the scale factor or magnification M is determined by dividing the periodicity of the image by the size of a basic square on the mask.

Assuming the object distance mask-lens g is constant, the image distance

---

[6] Faster analysis cycles ($< 0.8\ s$) are possible with modern computers, e.g. PCs running Windows 2000 with a Pentium 4, 2.0 GHz processor [22]. Direct comparison of the processing power of both computers reveals that the time needed for an analysis cycle which mainly depends on the execution time of the analysis algorithm in turn largely depends on the processing power. This was already assumed earlier [23].

lens-CCD b is related to the magnification M by

$$b = M \cdot g. \tag{4.1}$$

The origin $z = 0$ of the z-coordinate is assigned to an image distance b_0 for which the imaging equation

$$\frac{1}{f} = \frac{1}{b_0} + \frac{1}{g} \tag{4.2}$$

is fulfilled. In equation (4.2) f is the focal length of the lens used. Using to the usual sign convention[7] we get

$$z = b_0 - b = b_0 - M \cdot g \tag{4.3}$$

together with equation (4.1). Since it is quite difficult to measure g of the actual setup with a micrometer precision, the magnification M_0 at the position b_0 is measured by maximizing the sharpness of the image.

Using $b_0 = M_0 \cdot g$, equation (4.3) and 4.2 yield

$$z = g \cdot (M_0 - M) \tag{4.4}$$

and

$$\frac{1}{f} = \frac{1}{M_0 \cdot g} + \frac{1}{g} = \frac{1 + M_0}{M_0 \cdot g}. \tag{4.5}$$

Solving equation (4.5) for g yields

$$g = \frac{f}{M_0} \cdot (1 + M_0). \tag{4.6}$$

The z-coordinate of the image can therefore be determined as

$$z = f(M_0 + 1)(1 - \frac{M}{M_0}). \tag{4.7}$$

The z-coordinate positions for the distributions shown in figure 4.1 were calculated by employing equation (4.7) [8] setting M_0 to the calculated mean value $\overline{M_0}$ of the magnification measured.

The intrinsic resolutions of the RasNiK monitors installed at the test facility determined with the "multiple image" method described above are summarized in tables 4.1 to 4.4.

Table 4.1 shows the results of the resolution measurements made with the in-plane alignment system of the upper reference chamber. Data of the other

---

[7] $z > 0$ for decreasing lens-CCD distances and $z < 0$ for increasing lens-CDD distances

[8] Calculation in analogy to "A Formula for the z-Coordinate" [20].

Channel Name	x-coordinate		y-coordinate		z-coordinate	
	Mean [μm]	σ_x [μm]	Mean [μm]	σ_y [μm]	Mean [μm]	σ_z [μm]
In-plane 1	0.00 ± 0.06	0.55 ± 0.04	-0.01 ± 0.04	0.43 ± 0.03	0 ± 24	207 ± 20
In-plane 2	0.01 ± 0.06	0.64 ± 0.04	0.00 ± 0.05	0.57 ± 0.04	-7 ± 40	410 ± 39
In-plane 3	0.01 ± 0.05	0.56 ± 0.04	0.00 ± 0.06	0.71 ± 0.05	24 ± 35	361 ± 28
In-plane 4	0.03 ± 0.05	0.50 ± 0.04	-0.03 ± 0.05	0.53 ± 0.05	19 ± 21	219 ± 16

Table 4.1: Intrinsic resolution of all monitors of the in-plane alignment system of a BOS MDT chamber determined with the “multiple image”method. Sample data for one chamber are shown (upper reference chamber BOS2C10).

chambers are comparable and therefore not shown[9]. The resolution of the in-plane long- and crossbeams in the x- and y-direction transverse to the optical axis given by the standard deviations σ_x and σ_y is well below 1 μm.

Comparison to the corresponding r.m.s. values of table 4.2 for mask basic square sizes of 120 $\mu m \times$ 120 μm[10] shows that the resolution of the in-plane RasNiK monitors is almost an order of magnitude worse. This is due to the fact that a focal length of the lens of 60 mm used for the measurements cited in table 4.2 allows a total setup length of 240 mm if $g = b = 2 \cdot f$ holds true for the system. However, the focal length of the lenses that have to be used for the in-plane system should be 931 mm for the long- and 980 mm for the crossbeams if $g = b = 2 \cdot f$ is fulfilled. A measurement at NiKhef made with a setup of f = 1355 mm has shown that the thermal fluctuation of the air has the biggest impact on the accuracy for “large” mask-CCD distances (in that case 5420 mm). The resolution of such a system is about 2 μm [19].

The mask-CCD distances of the in-plane system are 3724 mm for the long- and 3920 mm for the crossbeams. Although the temperature gradient in the test-facility should be small since it is air-conditioned (compare to chapter 2), the air-conditioning system causes an air-flow leading to possible turbulences. The resolution of these systems should thus be worse than the ones cited in table 4.2 and better than those determined for the f = 1355 mm setup, which is true. We can thus conclude that the resolution of the in-plane system in the transverse directions is better than 1 μm as expected.

The resolution of the in-plane RasNiK systems for the z-coordinate measurement longitudinal to the optical axis is about 200 μm for the long- and 400 μm for the crossbeams. The angle between long- and crossbeams is such that the cosine of this angle yields a factor 0.95. This means resolution measurements along the z-direction of the chamber with a crossbeam should yield the same value as resolution measurements with the corresponding longbeam divided by

---

[9] Intrinsic resolution measurements for all RasNiK monitors of the in-plane alignment system of all chambers currently installed at The Munich Cosmic-Ray Test-Facility can be found in tables A.1 to A.3 of appendix A.

[10] The basic square size of the masks used for the in-plane as well as for the reference system is 120 $\mu m \times$ 120 μm.

that factor. This is not quite true for the crossbeam resolutions, probably because possible air turbulences and temperature gradients have a bigger impact on the crossbeam resolution measurement.

Size of mask fields [μm]	RMS x [μm]	expected[11] RMS x [μm]	RMS y [μm]	expected[11] RMS y [μm]	RMS z [μm]	expected RMS z [μm]
170	0.15	–	0.05	–	0.7	–
120	0.20	0.13	0.06	0.04	0.7	0.6
85	0.08	0.11	0.04	0.04	0.6	0.5

Table 4.2: Results of resolution measurements at NiKhef using the "multiple image" method with masks of different basic square sizes [19]. For each measurement 31 images were taken, except for the setup with the 170 μm basic square size mask in which case 32 images were taken. The focal length f of the lens used is 60 mm.

Comparison of the z-coordinate resolution determined for the in-plane system to the data of table 4.2 shows that the resolution determined for the z-coordinate measurement with an actual setup is nowhere near the resolution measured with the test setup. For a test setup with a lens of $f = 1355$ mm the resolution for the z-coordinate was about 70 μm [19]. Aluminum tubes were used to lessen the effect of temperature gradients and thermal fluctuations of the air. Since this cannot be done for the crossbeams of the in-plane system the author suspects possible temperature gradients and thermal fluctuations of the air causing a degradation of the intrinsic resolution in the actual setup. We can conclude that measurements along the z-coordinate are not accurate enough to allow for measurements with a few micrometers precision.

The results of the resolution measurement with the "multiple image" method for the longbeams of the reference alignment system are summarized in table 4.3. The mean of the x-, y- and z-coordinate measurements is again in good agreement with zero.

The resolution of the reference longbeams in the x- and y-direction transverse to the optical axis given by the standard deviations σ_x and σ_y varies from about 2 μm to about 5 μm for the x-coordinate measurement and is better than 3 μm for the y-coordinate measurement. The resolution of the z-coordinate measurement

---

[11] The larger the numbers of "features" i.e. black/white transitions of a coded mask, the better the accuracy of the reconstruction algorithm (compare section 3.1.1). Increasing the number of transitions by factors 1.4 and 2.0 by decreasing the size of the basic squares of the mask should improve the accuracy of the reconstructed position by factors $\sqrt{1.4}$ and $\sqrt{2}$, respectively. In table 4.2 the expected values are calculated using these factors together with the measurements made with the 170 μm mask. The three times smaller r.m.s. value for the y-coordinate is probably due to the synchronization accuracy of the framegrabber which only contributes to the x-coordinate measurements [19].

Channel Name	x-coordinate		y-coordinate		z-coordinate	
	Mean [μm]	σ_x [μm]	Mean [μm]	σ_y [μm]	Mean [μm]	σ_z [μm]
Reference 1	0.01 ± 0.16	1.77 ± 0.12	0.02 ± 0.27	2.91 ± 0.24	2 ± 22	241 ± 17
Reference 2	0.09 ± 0.20	2.22 ± 0.13	0.02 ± 0.20	2.12 ± 0.12	15 ± 20	220 ± 21
Reference 3	0.55 ± 0.54	5.18 ± 0.74	0.19 ± 0.25	2.57 ± 0.23	-1 ± 22	238 ± 22
Reference 4	-0.12 ± 0.43	4.41 ± 0.36	0.15 ± 0.27	2.99 ± 0.21	-26 ± 26	267 ± 23

Table 4.3: Intrinsic resolution of the longbeams of the reference alignment system determined with the “multiple image”method. Data for all reference longbeams are shown.

is about 250 μm. Therefore this coordinate measurement cannot be used if the vertical distance between the reference chambers is to be monitored.

The resolution for x-coordinate measurements of the reference longbeams 3 and 4 is not quite as good as one would expect compared to the resolution for the same coordinate of the longbeams 1 and 2. The degraded resolution is probably due to the effect of thermal fluctuations of the air as described above. These have a much bigger impact on the reference longbeams 3 and 4 since they are located at the end of the chambers where an air-conditioning outlet causes an airflow through a small air volume. The longbeams 1 and 2 are located at the other end of the chambers in a much larger air volume served by a single air-conditioning outlet not directly feeding this volume. Thermal fluctuations should thus be smaller in the case of the reference longbeams 1 and 2.

In section 3.1.3 an explanation of how the vertical distance is measured with the aid of the reference crossbeams was given. The resolutions determined for these RasNiK monitors are summarized in table 4.4. For x- and y-coordinate measurements the resolution of the crossbeam monitors is better than 1.5 μm and 3 μm respectively. For the z-coordinate measurement the resolution is about 300 μm as already expected.

Channel Name	x-coordinate		y-coordinate		z-coordinate	
	Mean [μm]	σ_x [μm]	Mean [μm]	σ_y [μm]	Mean [μm]	σ_z [μm]
RefCross 1	0.03 ± 0.06	0.68 ± 0.05	-0.19 ± 0.24	2.59 ± 0.22	18 ± 27	288 ± 21
RefCross 2	-0.02 ± 0.07	0.70 ± 0.04	-0.14 ± 0.22	2.18 ± 0.20	-15 ± 22	243 ± 20
RefCross 3	-0.04 ± 0.10	1.10 ± 0.07	0.05 ± 0.17	1.88 ± 0.17	16 ± 25	273 ± 22
RefCross 4	0.03 ± 0.11	1.23 ± 0.08	0.28 ± 0.31	2.74 ± 0.25	25 ± 31	303 ± 27

Table 4.4: Intrinsic resolution of the crossbeams of the reference alignment system determined with the “multiple image”method. Data for all reference crossbeams are shown.

Reference crossbeam and longbeam resolutions should be about the same for all coordinates since the mask-CCD distance of both systems is comparable. A look at the data presented in tables 4.3 and 4.4 reveals that the resolution for x-coordinate measurements of the crossbeams is unusually good compared to the resolution of the longbeams for that coordinate.

The reason for this effect can probably be found by looking at mask images captured by the framegrabber for a long- and a corresponding crossbeam (e.g. figure 3.7). Only about a third of the crossbeam mask image can be used for the determination of the x-position, so there is very little redundancy. Redundant image information contained in the remaining two thirds of the mask image could otherwise be used to make the fit more reliable. The lack of redundancy thus leads to an overall loss of position information making the measurement only seemingly more accurate but less reliable in reality. For the determination of the y-position the full height of the image can be used which offers some redundancy and apparently suffices to gain reliable results.

In analogy to the case of the reference longbeams 3 and 4 compared to the longbeams 1 and 2 the resolution of the crossbeams 3 and 4 for x-coordinate measurements is worse than the resolution for the same coordinate of the crossbeams 1 and 2. The degraded resolution is probably due to the effect of thermal fluctuations of the air already described above.

Through the analysis of the resolution measurements made using the multiple image method we can conclude that the aim of achieving a precision of about 3 μm for displacement measurements transverse to the optical axis of the reference RasNiK monitors can be fulfilled. The resolution of the reference alignment monitors is good enough to allow displacement measurements within a 5 μm-limit needed for the alignment monitoring of the reference chambers (compare to chapter 3).

4.2 Monitoring the Single Chamber Geometry

Section 3.1.2 of chapter 3 introduced the setup of the in-plane alignment system which is used to monitor possible chamber deformations such as curvature, torsion and thermal expansion on the micrometer scale. At the cosmic-ray test-facility each chamber is monitored with the aid of its in-plane system in order to be able to reconstruct the deformation parameters of interest. The reconstructed parameters allow to tell if the chamber geometries were mechanically stable within the 5 μm regime aimed at.

If the chambers fulfill this requirement the track points of cosmic muon tracks measured with each chamber can safely be used to reconstruct the whole muon track and determine the wire-to-wire distances of the drift tubes and the wire plane distances of the test chamber with a precision of about 10 μm (see section 2.2). Additionally, it is then possible to regard the chambers as rigid bodies when calculating relative displacements between the them. In section 4.3 the assumption that the chambers can be regarded as rigid bodies is used when displacements between both reference chambers measured with the reference alignment system are calculated.

In the previous section we have seen that the intrinsic resolution of the in-plane alignment RasNiK monitors of all BOS type MDT chambers installed at the cosmic-ray test-facility is better than 1 μm for position measurements in the x- and y-direction perpendicular to the optical axis. Furthermore, we had to conclude that the position measurement in z-direction ranging from about 200 μm for the in-plane longbeams to about 400 μm for the in-plane crossbeams cannot be used to measure displacements and deformations in that direction on the micrometer scale. Let us have a look which geometrical parameters can be reconstructed using the RasNiK monitor measurements of the in-plane alignment system of a single chamber.

4.2.1 Building a Model of Possible Deformations

Some assumptions are needed to construct an analytical model[12] of the in-plane alignment system. The fundamental assumption made here is that the geometry of an MDT chamber is completely defined by the relative position of its three cross-plates and by their internal properties which will be explained later.

Figure 4.2 shows the chamber cross-plates and introduces their numbering. The paths of the light rays of the in-plane alignment system are indicated in this figure. The coded masks are mounted on cross-plate no. 1, the lenses on cross-plate no. 2 and the CCDs on cross-plate no. 3.

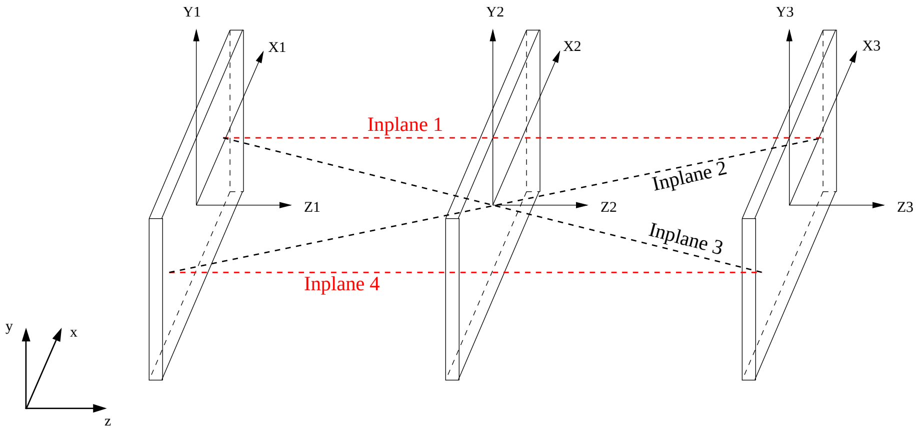

Figure 4.2: Model of a BOS type MDT chamber assuming its geometry is completely defined by the relative position of its three cross-plates and their internal properties [24]. The dashed lines show the paths of the light rays of the in-plane alignment system.

The internal properties of each cross-plate (i = 1,2,3) taken into account in this model can be characterized by two parameters. One parameter is the cross-plate temperature $t_i^{const.}$, assumed to be constant along the cross-plate. These

---

[12] The analytical model presented here is based on a model introduced by A. Ostaptchuk [24].

temperatures act as scale factors between the cross-plates (thermal expansion). The other is the cross-plate sag in direction of y, assumed to lead to cross-plate shapes like a symmetrical parabola as shown in figure 4.3.

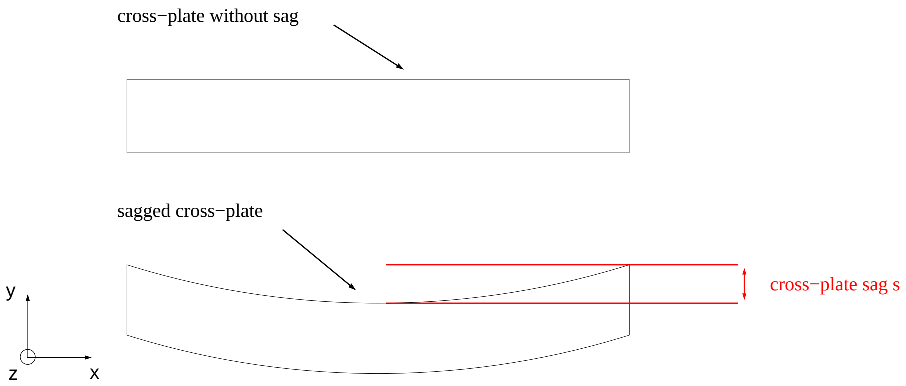

Figure 4.3: Sketch visualizing the cross-plate sag.

The origin of the local cross-plate coordinate frame is fixed to the center of each cross-plate. The global coordinate frame coincides with the local coordinate frame of the middle cross-plate. Then six parameters define the position of each of the extremal cross-plates (i = 1,3) relative to the middle cross-plate (i = 2) acting as reference. These parameters are the translations $\Delta_i x$, $\Delta_i y$ and $\Delta_i z$ ($\forall i = 1, 3$) in the three spatial directions and the three rotations R_i^x, R_i^y and R_i^z ($\forall i = 1, 3$) around each of the coordinate axes of the local coordinate frame.

This means the total number of the degrees of freedom of the modeled system is

$$N_{par} = 2 \cdot 3 + (3 + 3) \cdot 2 = 18 \tag{4.8}$$

(temperature and sag (2) of each cross-plate (3) and translations (3) as well as rotations (3) of the outer cross-plates (2) with respect to the middle one).

In principle each RasNiK monitor of the in-plane system contributes measurement of four parameters relevant for the reconstruction of the chamber geometry: the lens displacement d^x and d^y in both directions perpendicular to the optical axis, the magnification M used in section 4.1 to calculate the z-coordinate position (see equation (4.7)) and the relative rotation angle α^z between the mask and the CCD around the optical axis (*Figure 4.4*).

However, section 4.1 has already shown that the magnification measurement M is not precise enough to reconstruct deformations on the micrometer scale. The algorithm of the program employed to reconstruct the chamber deformations[13] relevant to decide on the mechanical stability of the chambers only uses the lens displacement measurement d^y perpendicular to the optical axis of the

---

[13] The following subsection 4.2.2 will explain the algorithm and show and interpret results gained using it.

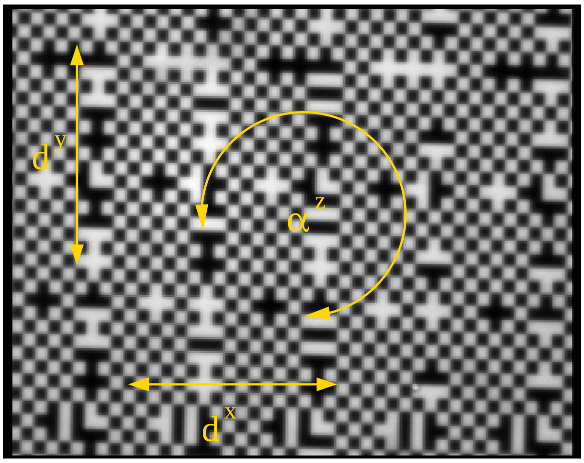

Figure 4.4: Parameters measured by a RasNiK monitor indicated on a mask image. Possible displacements d^x and d^y in both directions perpendicular to the optical axis and the relative rotation angle α^z between the mask and the CCD around the optical axis have been indicated. Details about the magnification measurement M can be found in section 3.1.1. Note that displacement of any optical element of a monitor has an impact on the mask image and thereby on the indicated parameters measured by a RasNiK system.

four in-plane RasNik monitors. These measurements do not suffer from the synchronization error of the framegrabber like the measurements of lens displacement d^x do (see section 4.1) and offer a better precision than the measurement of the rotation angle α^z between the mask and the CCD around the optical axis. Also, the deformation parameters of special interest can all be reconstructed using the measurements of d^y.

Let us nevertheless have a look which deformation parameters could in principle be reconstructed if all the measured parameters of all in-plane RasNiK monitors are used. As the in-plane alignment system consists of a total of four RasNiK monitors in principle a total of 16 chamber deformation dependent measurements are provided.

The 16 RasNiK measurements of the in-plane alignment system can be divided into two subsets of eight measurements each allowing to calculate different deformation parameters. One subset of eight measurements is formed by the in-plane RasNiK measurements d^y_j and α^z_j (j = inp1, inp2, inp3, inp4) (see figure 4.4). This subset allows to reconstruct 6 parameters.

The chamber sag along the direction of the drift tubes (the chamber sag in y direction, figure 4.5)

$$\Delta_y = \frac{\Delta_1 y + \Delta_3 y}{2} \tag{4.9}$$

is one parameter reconstructible with this subset. The measurements d_j^y of the in-plane RasNiK monitors are sensitive to this parameter reconstructed with the above mentioned program.

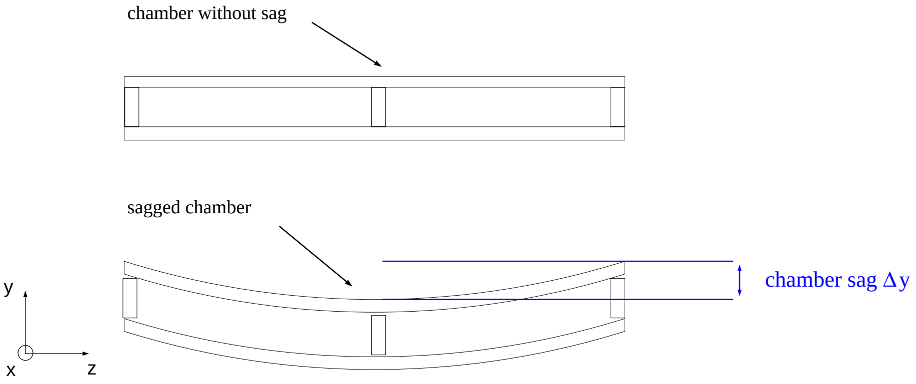

Figure 4.5: Sketch visualizing the chamber sag.

Two parameters are the rotations around the z-axis of the extremal cross-plates with respect to the middle cross-plate, visualized in figure 4.6:

$$R_1^z \quad \text{and} \quad R_3^z. \tag{4.10}$$

Both of these rotations are deformation parameters affecting the d_j^y measurements of the in-plane system and are thus also reconstructed with the program used for data analysis.

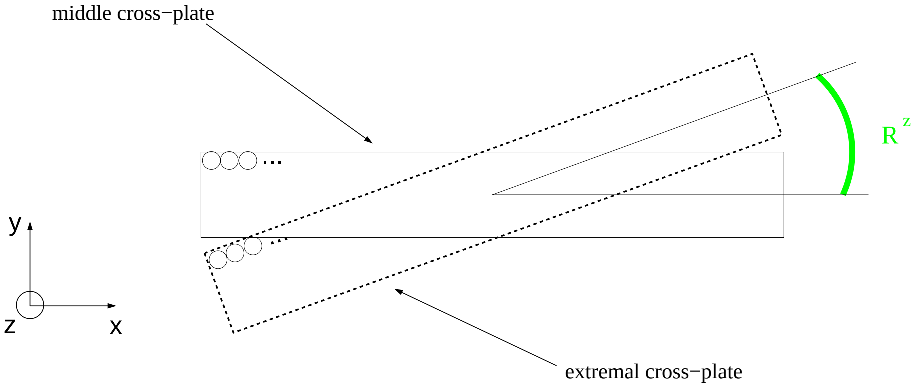

Figure 4.6: Sketch visualizing the rotation of either of the extremal cross-plates relative to the middle one.

The three missing parameters are the sags of the cross-plates (see figure 4.3)

$$s_i. \tag{4.11}$$

Only the sag of the middle cross-plate is reconstructed in the analysis. The possible sags of the other cross-plates can only be reconstructed if the measured rotation angles α_j^z are used in addition to the measurements of d_j^y.

The subset formed by the other the other eight RasNiK measurements d_j^x and M_j (j = inp1, inp2, inp3, inp4) (see figure 4.4) allow the reconstruction of another 6 deformation parameters. Two parameters are the chamber sag in x-direction

$$\Delta_x = \frac{\Delta_1 x + \Delta_3 x}{2} \tag{4.12}$$

and the non-uniformity of chamber expansions in z-direction

$$\Delta_z = \frac{\Delta_1 z + \Delta_3 z}{2}. \tag{4.13}$$

Another two deformation parameters are

$$R_1^y \text{ and } R_3^y, \tag{4.14}$$

the rotations of the extremal cross-plates with respect to the middle one around their y-axis. The last two parameters are the temperature differences between the middle cross-plate and each of the extremal ones

$$\Delta t_{12}^{const.} = \Delta t_1^{const.} - \Delta t_2^{const.} \text{ and } \Delta t_{32}^{const.} = \Delta t_3^{const.} - \Delta t_2^{const.}. \tag{4.15}$$

These 12 parameters out of 18 parameters characterizing deformations of the modeled MDT chamber can in principle be reconstructed from the 16 in-plane RasNiK measurements. The deformation parameters actually reconstructed and controlled are the chamber sag in y-direction Δ_y, the sag of the middle crossplate s_2 and the rotation angles R_1^z and R_3^z around the z-axis of the extremal cross-plates with respect to the middle one (the torsion of the chamber). Six parameters of the model remain uncontrollable.

Two of the uncontrollable parameters are the parallelogram shape of the chamber in y-direction described by

$$\frac{\Delta_1 y + \Delta_3 y}{2} \tag{4.16}$$

and shown on the left hand side of figure 4.7 and the parallelogram shape of the chamber in x-direction described by

$$\frac{\Delta_1 x + \Delta_3 x}{2} \tag{4.17}$$

visualized on the right hand side of figure 4.7.

For the first order of magnitude a parallelogram deformation of the chamber in y-direction or in x-direction is equivalent to the rotation of the whole chamber around the x-axis or the y-axis, respectively. Such rotations of e.g. a reference

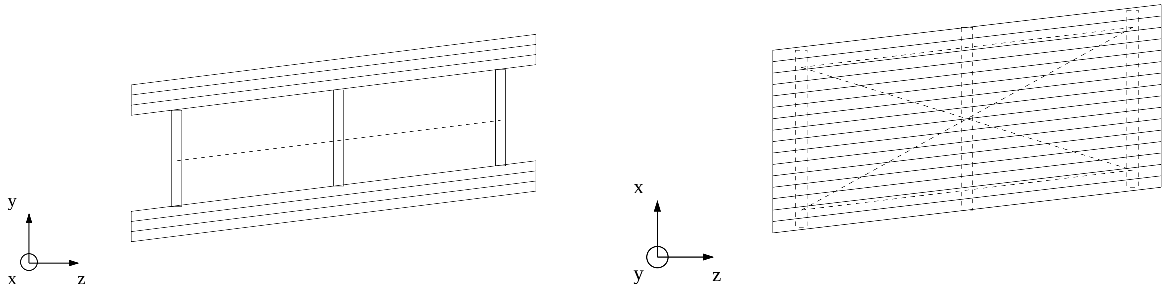

Figure 4.7: Sketch of chamber parallelogram deformations in different directions. Left: Parallelogram deformation in y-direction. Right: Parallelogram deformation in x-direction [24].

chamber would thus have to be detected by the reference alignment system monitoring relative displacements between the reference chambers.

Since the in-plane alignment system is not sensitive to the rotations

$$R_1^x \quad \text{and} \quad R_3^x. \tag{4.18}$$

of the extremal cross-plates with respect to the middle one around their x-axis these two deformation parameters can also not be reconstructed. Those kind of deformations can be caused by different temperatures of the chamber multilayers.

Furthermore, uniform chamber extensions in wire direction described by the parameter

$$\frac{\Delta_1 z + \Delta_3 z}{2} \tag{4.19}$$

cannot be controlled by the in-plane alignment system, in contrast to the non-uniformity parameter described by equation (4.13). Expansions of the chamber in z-direction along the anode wires of the drift tubes have no impact on the measurements made at the cosmic-ray test-facility. Possible uniform chamber expansions and contractions can nevertheless be monitored by the reference alignment system.

The last uncontrollable parameter is the temperature $t_2^{const.}$ of the middle cross-plate, meaning that the in-plane alignment system is not sensitive to uniform temperature changes of the whole chamber. As above, uniform expansions and contractions caused by uniform temperature changes would thus have to be monitored by the reference alignment system.

4.2.2 Reconstruction of Single Chamber Deformations

Before taking a close look at analyzed data of the in-plane system, the idea behind the reconstruction algorithm of the deformation parameters shall be explained. It is based on the numerical minimization of a χ^2-function.

The χ^2-function implemented in the program[14] used by the author to reconstruct and analyze the deformation parameters of MDT chambers depends on the parameters of the most probable chamber deformations. These are the chamber sag in y-direction Δ_y, the sag of the middle cross-plate s_2 and the rotation angles R_1^z and R_3^z around the z-axis of the extremal cross-plates with respect to the middle one as already mentioned in section 4.2.1. It uses the RasNiK monitor measurements d_j^y ($j =$ inp1, inp2, inp3, inp4) (see figure 4.4) of the four in-plane RasNiK systems and looks as follows:

$$\chi^2 = \sum_{j=1}^{4} \frac{\left[d_j^y - d_{j_{theo}}^y(\Delta_y, R_1^z, R_3^z, s_2)\right]^2}{Res_y^2}. \tag{4.20}$$

The variable Res_y^2 stands for the resolution of the RasNiK monitors for the d_j^y measurements.

The following steps are processed by the program to reconstruct the deformation parameters:

1. Definition of the chamber geometry. The coordinates of the local cross-plate coordinate frame with respect to the global one (fixed to the center of the middle cross-plate) are initialized and the coordinates of each of the in-plane RasNiK monitor elements (mask, lens, CCD) are defined in the local coordinate frame of the cross-plate the respective element is mounted on.

2. Read-in of the measured data. The first set of in-plane data[15] is used as calibration data set. It is subtracted from all of the following sets of data. This means the d_j^y measurements used in the χ^2-function (equation (4.20)) are the difference between the calibration data set and each of the following measurements.

   The subtraction of these initial monitor values (zero readings) is coupled to the assumption that the chamber is in its “ideal” position, meaning the chamber sag in y-direction Δ_y, the sag of the middle cross-plate s_2 and the rotation angles R_1^z and R_3^z around the z-axis of the extremal cross-plates with respect to the middle one are all zero[16].

   If the absolute deformation of the chambers installed at the test facility would be of interest, the zero values from the flat granite assembly table had to be used, since the assumption of the chamber being free of deformations after having left the assembly table is not valid. Since only relative changes

---

[14] The program used for data analysis in this section is a slightly modified version of georec_y.f developed by A. Ostaptchuk.

[15] A set of in-plane data is a total of four measurements belonging to one time: one measurement of each of the four RasNiK monitors the in-plane system consists of.

[16] Zero means inside measurement tolerances $\sigma^0_{\Delta_y}$, $\sigma^0_{s_2}$, $\sigma^0_{R_1^z}$ and $\sigma^0_{R_3^z}$.

of the chamber geometry have to be monitored with the in-plane alignment systems of the chambers installed at the cosmic-ray test-facility, it is a valid procedure to use the first set of in-plane data as calibration data set. All deformations reconstructed are thus deformations relative to the chamber geometry encountered initially when data acquisition began.

3. Initialization of the chamber deformation parameters to be reconstructed. The parameters were already mentioned under point two. They are all initialized to zero for reasons already given there.

4. Transfer of the local coordinates to the global coordinate system.

5. Minimization of the χ^2-function (equation (4.20)). The precision with which the deformation parameters have to be reconstructed can be defined and is set to 1 μm for the chamber y-sag Δ_y and the sag of the middle cross-plate s_2. For the angles R_1^z and R_3^z a precision of 1 μrad is required.

One assumption is needed for the program to produce reliable results. It is assumed that all angles are small enough to carry out rotations in arbitrary order without having to resort to the use of Euler angles.

After having explained the model and the algorithm behind the geometry reconstruction program used for data analysis, we will now take a look at results gained through its use. The data shown in figure 4.8 to figure 4.13 was acquired with the in-plane alignment system of the upper reference chamber for a period of 7 days, starting at 0^{00} o'clock on July 19th and ending at 18^{14} o'clock on July 25th of 2002.

All figures shown prove that the in-plane alignment system of MDT chambers installed at the cosmic-ray test-facility is fully operational and reliable for operation times of several days. Raw data of the optical system of the upper reference chamber was analyzed with the modified version of the geometry reconstruction program described above. It is not shown here since it would only prove that the in-plane system is fully operational.

Figure 4.8 visualizes the chamber sag Δ_y in y-direction along the drift tubes over a period of seven days. During this period, the chamber sag did not vary more than 5 μm, although the air conditioning was switched off. During periods of 24 hours it can safely be said that the sag Δ_y varies about 3 μm on average.

A 24-hour structure is visible in figure 4.8. By comparison to the temperature of the upper multilayer shown in figure 4.9 a clear correlation between the multilayer temperature and the chamber sag Δ_y in the direction along the drift tubes can be seen[17].

---

[17] Horizontal mirroring of the temperature plot (*Figure 4.9*) reveals the same course of both the temperature curve and the curve of the chamber sag Δ_y.

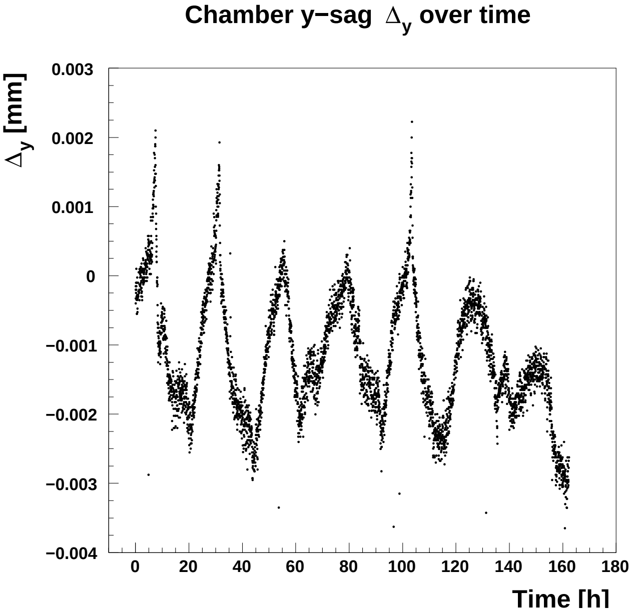

Figure 4.8: Sag Δ_y of a BOS MDT chamber (upper reference chamber) along the direction of the drift tubes in dependence of the time. Sample data are shown for a timespan of seven days, measurements are two minutes apart.

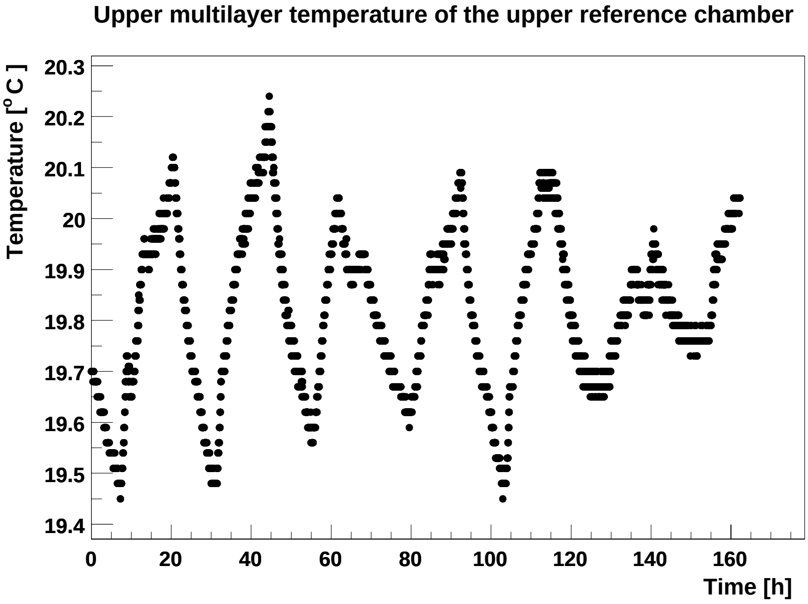

Figure 4.9: Temperature of the upper multilayer of the upper reference chamber. Sample data are shown for a timespan of seven days, measurements are one minute apart. The timespan exactly corresponds to the timespan of the plots shown in figure 4.8 to figure 4.13.

Unfortunately at the time no temperature sensor was installed on the lower multilayer of the chamber, so apart from a clear correlation between this chamber deformation parameter and the temperature of the upper multilayer one cannot tell whether temperature differences between both multilayers cause this kind of chamber deformation in this case, although it is probable. The placement of the temperature sensors monitoring the chamber temperature at different locations on the chambers has since been modified, so future measurements with both the in-plane alignment system and the temperature sensors will allow quantitative investigations.

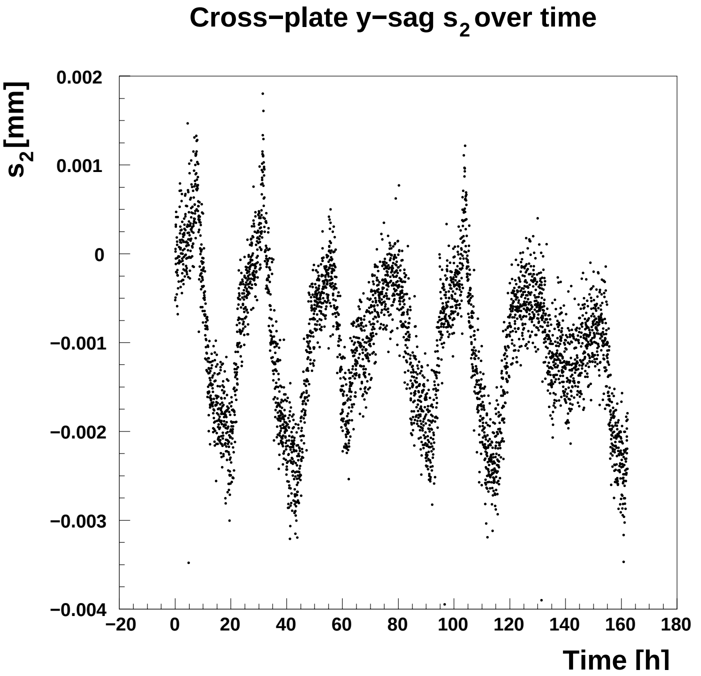

Figure 4.10: Sag s_2 of the middle cross-plate of a BOS MDT chamber (upper reference chamber). Sample data are shown for a timespan of seven days, measurements are two minutes apart.

Figure 4.10 shows the sag of the middle cross-plate s_2 as a function of the time. The course of the cross-plate sag curve is similar to the curve of the chamber y-sag Δ_y presented in figure 4.8. Both deformation parameters are clearly correlated as can be deduced from figure 4.11.

Although the course of both curves is similar and shows the same 24-hour structure, the variations of the cross-plate sag are slightly smaller than those of the chamber y-sag. The total variation over the data-acquisition time of 7 days is about 4 μm, variations during periods of 24 hours are sightly smaller than 3 μm on average.

The rotation R_3^z of the cross-plate on the read-out side of the MDT chamber

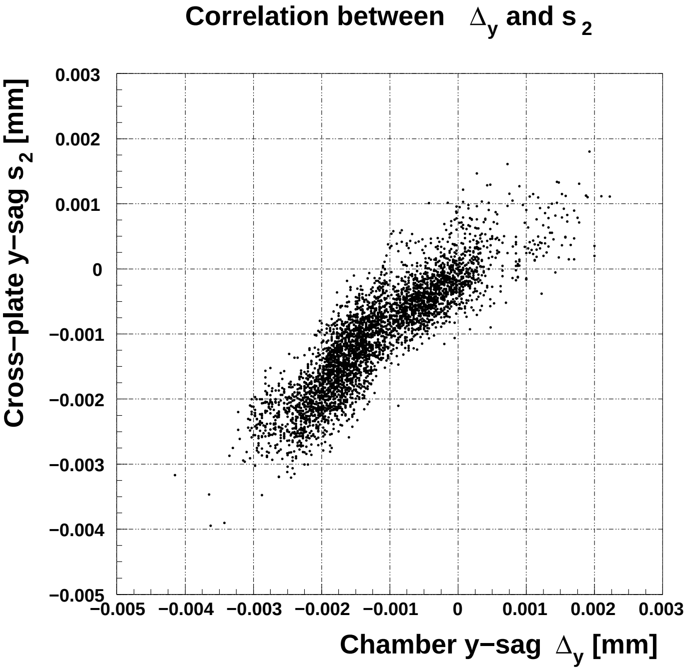

Figure 4.11: Correlation between the sag Δ_y of an BOS MDT chamber (upper reference chamber) and its middle cross-plate sag s_2. The correlation is plotted for data shown in figure 4.8 and figure 4.10.

with respect to the middle cross-plate is presented in figure 4.12. Maximum variation of the angle is about 10 μrad, on average the angle varies about 8 μrad during 24 hours. A plot of the rotation angle R_1^z of the cross-plate on the high-voltage side of the MDT chamber is not shown, since the rotation angle is so small that it cannot be reconstructed.

It is a fact that the high-voltage cross-plate is fixed to a mounting rail with the aid of two mounts and shows no torsion with respect to the middle cross-plate, whereas the read-out cross-plate is only fixed to a mounting rail with one mount in its center and shows the plotted torsion. This is quite surprising because the mounts are so-called “kinematic” mounts which should allow any chamber movements without imposing any mechanical constraint. A rotation of the high-voltage cross-plate with respect to the middle cross-plate should thus be possible, too, no matter if this cross-plate is fixed to the mounting rails at two points.

The last figure shown (*Figure 4.13*) visualizes the correlation between the chamber y-sag Δ_y (*Figure 4.8*) and the angle between the read-out and the middle cross-plate (*Figure 4.12*). As for the case of the chamber y-sag Δ_y and the sag of the middle cross-plate s_2 a correlation becomes visible. It can therefore be concluded that the sag of the middle cross-plate s_2 is also correlated to the angle R_3^z plotted in figure 4.12.

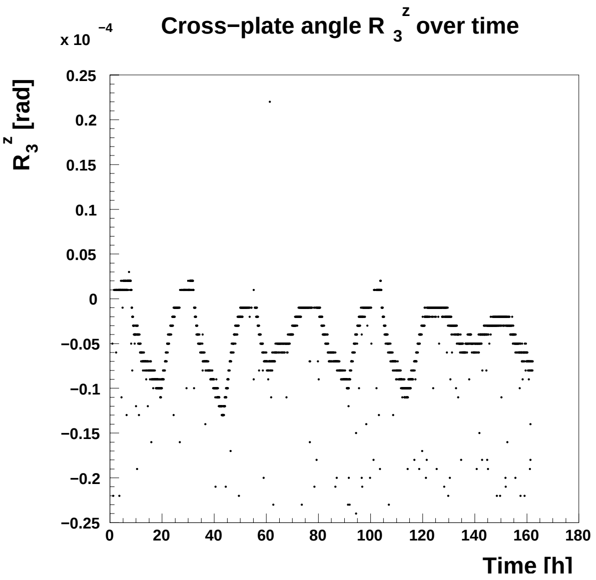

Figure 4.12: Angle R_3^z between the read-out cross-plate and the middle cross-plate of a BOS MDT chamber. Sample data are shown for a timespan of seven days, measurements are two minutes apart.

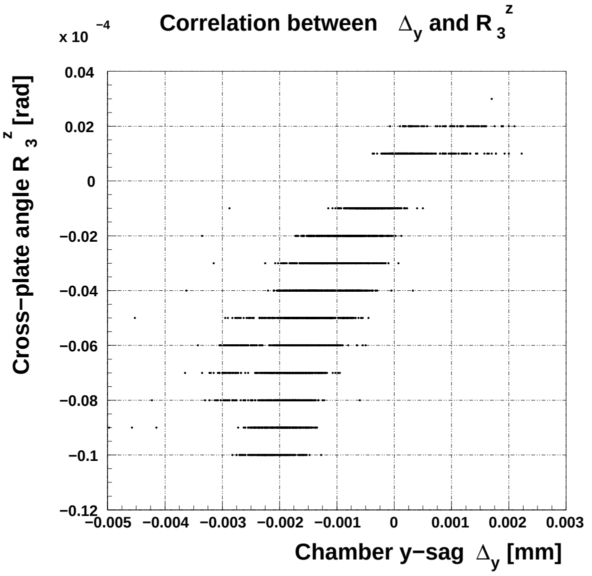

Figure 4.13: Correlation between the sag Δ_y of an BOS MDT chamber (upper reference chamber) and the angle between its read-out and its middle cross-plate R_3^z. The correlation is plotted for data shown in figure 4.8 and figure 4.12.

By looking at the correlations between the chamber y-sag Δ_y, the sag of the middle cross-plate s_2 and the angle R_3^z between the read-out and the middle cross-plate, a consistent picture of the chamber deformation emerges: A small sag of the middle cross-plate and an angle between read-out and middle cross-plate will lead to a slight chamber sag or vice versa.

The most important result of the analysis of the data presented here is, however, that the chamber deformations, whose main parameters were reconstructed with the program described above, are slightly below the critical 5 μm level of mechanical stability needed for the measurement of the wire-to-wire and wire plane distances of a test chamber at the cosmic-ray test-facility. Apparently, this is true even though the air-conditioning system of the cosmic-ray test-facility was not running during the period of time for which data was analyzed.

Furthermore, one can also conclude that treating the reference chambers as rigid bodies when reconstructing relative displacements between them is a valid assumption. Keeping the validity of the "rigid-body hypothesis" in mind, we will next introduce a model allowing to reconstruct possible relative displacements between the reference chambers.

4.3 Monitoring Relative Movements of Muon Chambers

Section 3.1.3 of chapter 3 introduced the setup of the reference alignment system installed at the cosmic-ray test facility. It is used to monitor possible relative chamber displacements between the upper an the lower reference chamber on the micrometer scale. Reconstructing the parameters of possible displacements using the reference alignment system data allows to tell if their relative position is stable within an upper limit of 5 μm[18].

The previous section 4.2 allows to conclude that it is possible to reconstruct certain geometrical parameters of the shape of an MDT chamber with about 1 μm precision using the data of the in-plane system. In turn, this allows to tell whether chambers are mechanically stable enough to be regarded as rigid bodies when calculating relative displacements between them. Section 4.2 has shown the validity of the "rigid-body hypothesis".

It is important to check if it is safe to make this assumption prior to calculating any relative displacements between the upper and the lower reference chamber because of the setup of the reference alignment system. Since this system is glued to the chamber structure (for details of the setup see section 3.1.3) possible individual chamber deformations have a direct impact on the geometry of a reference RasNiK monitor. This could lead to measuring relative displacements between

---

[18] The reasons for this limit are the same as in the case of individual chamber deformations, compare to section 4.2.

the reference chambers with the reference alignment system although no relative displacements have occurred.

In section 4.1 of this chapter we have seen that the intrinsic resolution of the RasNiK monitors of the reference alignment system installed at the cosmic-ray test-facility is about 3 μm for displacement measurements perpendicular to the optical axis whereas the resolution for measurements longitudinal to the optical axis does not permit their use for displacement measurements on the micrometer scale. Let us have a look which parameters of relative chamber displacements between the two reference chambers can be reconstructed using the RasNiK monitor measurements of the reference alignment system.

4.3.1 Possible Relative Movements - a Model

In analogy to the construction of an analytical model of the in-plane alignment system, some assumptions have to be made in order to be able to construct a model of the reference alignment system. The fundamental assumption made in this case is that the geometry of the reference chambers is stable enough to regard them as rigid bodies. This hypothesis has been tested and found to be true.

Another assumption allows further simplification of the reference alignment model. In contrast to the case of the in-plane alignment system where the optical elements of each of the RasNiK monitors are located on different cross-plates and can therefore all move relative to each other, it can be assumed that mask and lens of each of the reference RasNiK monitors remain in a fixed position at a fixed distance relative to each other for the period of data-acquisition. This assumption is a consequence of the “rigid-body hypothesis”: Since the mask and lens support structures of every reference RasNiK monitor are glued to the same chamber (upper reference chamber) and are only separated by either of the extremal cross-plates, their position relative to each other has to remain fixed if the chamber as such can be regarded as mechanically stable (rigid body). The previous section has shown that cross-plate sag variations are below 4 μm over a period of days, so this assumption is valid.

Apart from being treated as rigid bodies no other internal properties of the reference chambers are taken into account in the model. Most of the internal properties of the reference chambers are already controlled by the in-plane alignment model presented in section 4.2.1. The mechanical stability of the reference chambers is the only property needed to reconstruct possible relative displacements between them.

The origin of the local chamber coordinate frame is fixed to the center of its middle cross-plate. The global coordinate frame coincides with the local coordinate frame of the upper reference chamber. Then six parameters define the position of the lower reference chamber with respect to the upper reference chamber acting as reference. These parameters are the translations Δx, Δy and Δz in the three spatial directions and the three rotations R^x, R^y and R^z around each of

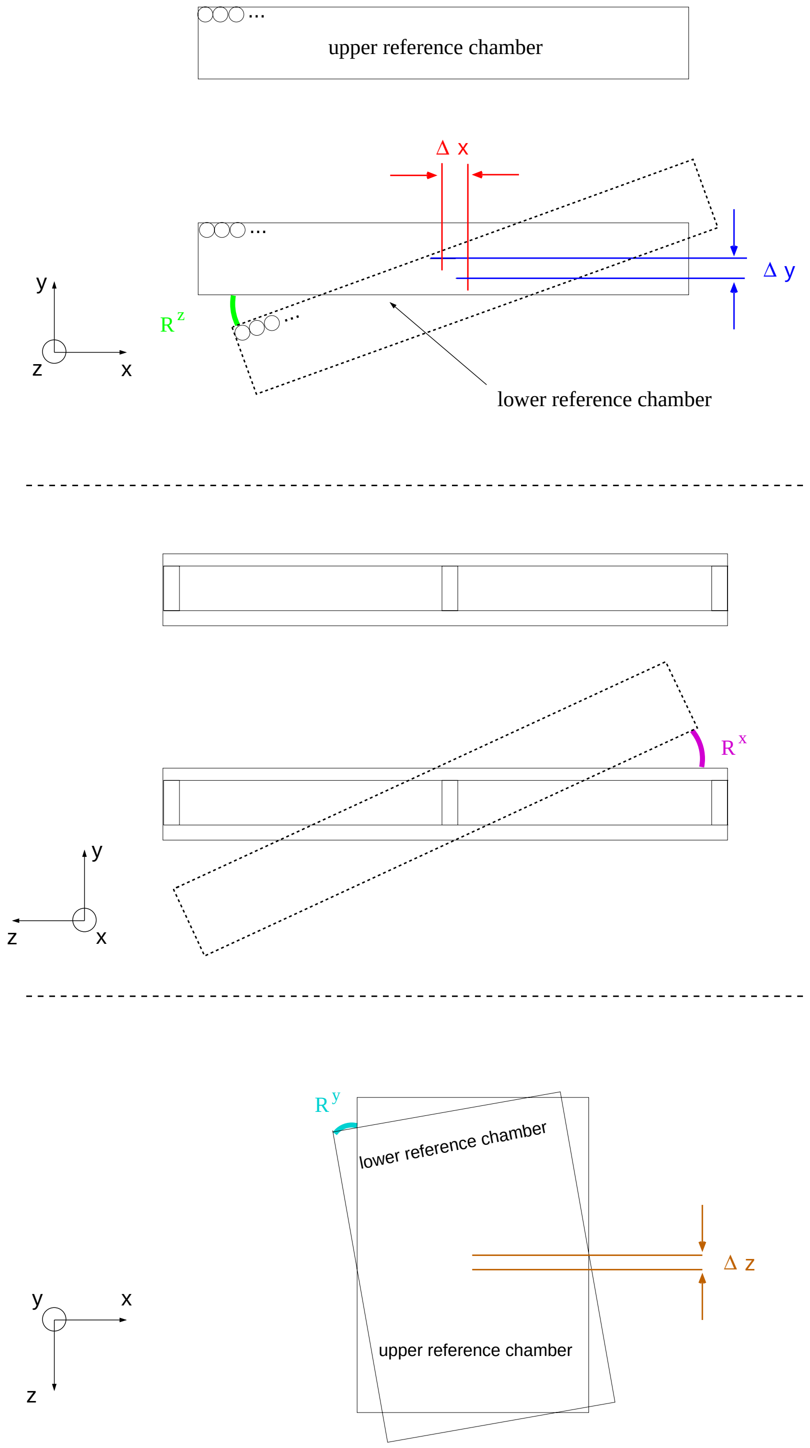

Figure 4.14: Sketch of possible displacements of the lower reference chamber relative to the upper reference chamber.

the coordinate axes of the global coordinate frame. Figure 4.14 visualizes the parameters characterizing possible relative chamber displacements of the reference system.

The total number of the degrees of freedom of the modeled system thus is

$$N_{par} = 3 + 3 = 6 \tag{4.21}$$

As stated in section 4.2.1 for the case of the in-plane system, in principle each RasNiK monitor of the reference system also contributes four measured parameters. This time the measurements of the lens displacement d^x and d^y in both directions perpendicular to the optical axis, the magnification M and the relative rotation angle α^z between the mask and the CCD around the optical axis of each reference RasNiK monitor can in principle be employed to reconstruct relative chamber displacements.

In analogy to section 4.2.2, the magnification measurement M is not used for reconstruction of relative chamber displacement parameters because of its lack of precision. Both of the lens displacement measurements d^x and d^y perpendicular to the optical axis of each of the eight reference RasNiK monitors are used to reconstruct the six relative displacement parameters. Even without the use of the measured rotation angle α^z between the mask and the CCD around the optical axis of each reference RasNiK system, this offers a total of 16 relative chamber displacement dependent measurements allowing to reconstruct all of the six model parameters of possible relative chamber displacements. The system of possible displacements is thus overdetermined.

The following subsection will make use of the presented model of relative reference chamber displacements and present data of reconstructed and analyzed relative chamber displacement parameters.

4.3.2 Reconstruction of Relative Displacements between the Reference Muon Chambers

Before taking a look at analyzed data of the reference system, some remarks about the program[19] used to reconstruct and analyze the relative reference chamber displacement parameters will be made.

The program employed makes use of the same principle as the program explained in section 4.2.2. Analogously, it is based on the minimization of a χ^2-function depending on the chamber displacement parameters. In case of the reference alignment system, these are the translations Δx, Δy and Δz in the three spatial directions and the three rotations R^x, R^y and R^z around each of

---

[19] The program used for data analysis in this section is called testalign.f. It was developed by A. Ostaptchuk and the author himself. It is based on A. Ostaptchuk's previous program geo-rec_y.f already mentioned and employed by the author for the analysis of the in-plane alignment system data (see section 4.2.2).

the coordinate axes of the global coordinate frame, as mentioned in section 4.3.1. The χ^2-function now uses the reference RasNiK monitor measurements d_j^x and d_j^y ($j = $ ref1, refcr1, ref2, …, refcr4) (see figure 4.4) and looks as follows:

$$\chi^2 = \sum_{j=1}^{8} \left[\frac{\left[d_j^x - d_{j_{theo}}^x(\Delta_x, \Delta_y, R^y, R^z)\right]^2}{Res_x^2} + \frac{\left[d_j^y - d_{j_{theo}}^y(\Delta_z, R^x, R^y)\right]^2}{Res_y^2} \right]. \quad (4.22)$$

The variables Res_x^2 and Res_y^2 stand for the resolution of the RasNiK monitors for the measurement of d_j^x and d_j^y, respectively.

The implementation of the reconstruction algorithm and the steps processed by the program to reconstruct the relative chamber displacement parameters are essentially the same as for the case of the in-plane alignment system described in section 4.2.2, so they will not be repeated here.

The data presented in figure 4.15 to figure 4.20 was acquired with the reference alignment system for a period of 8 days, starting at 17^{38} o'clock on September 8th and ending at 16^{16} o'clock on September 15th of 2002. All figures shown prove that the reference alignment system set up at the cosmic-ray test-facility is fully operational and reliable for operation times of several days. As for the data analysis of the in-plane system, no raw data of the reference alignment system will be shown here, since it would only prove that the reference alignment system is fully operational.

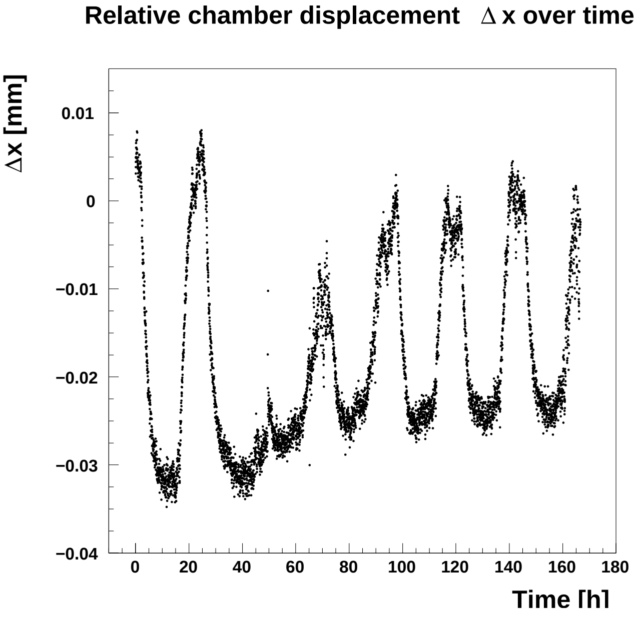

Figure 4.15: Relative displacements Δx (see figure 4.14) between the reference chambers. Sample data for a period of eight days.

Figure 4.15 visualizes the relative displacement Δx between the reference chambers in x-direction (compare to figure 4.14) for a period of eight consecutive days. It can be seen that no system failures occurred, all data could be used for analysis. During this period, the relative chamber displacement Δx varied by about 40 μm. It can thus already be concluded that the alignment monitoring between the reference chambers is indispensable as displacements between the chambers exceed the stability limit of 5 μm over a period of 20 hours needed for the determination of the wire-to-wire and the wire plane distances. Only for the period between 40 and 70 hours the displacement Δx stays within this limit, no other stable period of 20 hours can be found.

A 24-hour structure is clearly visible in figure 4.15. Within this structure, periods of stability not exceeding the often mentioned 5 μm-limit can be found. Stable periods of about 10 hours are periodically encountered, starting during the second half of the night and lasting until about noon. Then a shift Δx of about 25 μm within roughly 2-3 hours can be seen, followed by a second period of stability of about 5 hours. The cycle is completed by another shift Δx of about 25 μm within roughly 2-3 hours having the opposite sense of direction compared to the first shift.

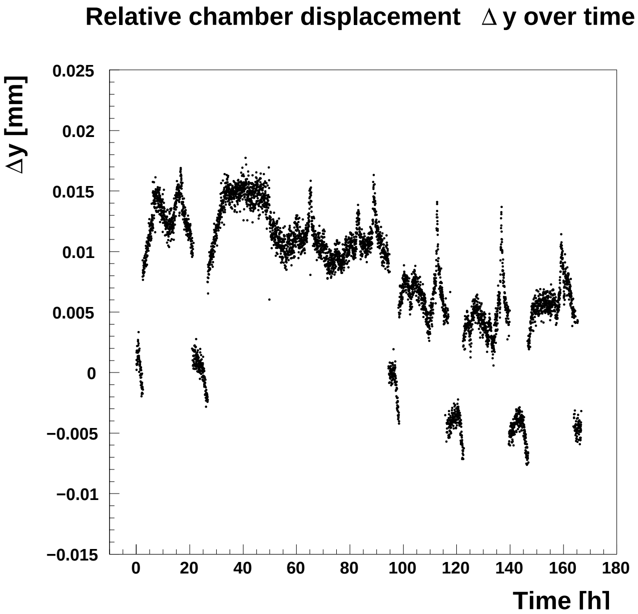

Figure 4.16: Relative displacements Δy (see figure 4.14) between the reference chambers. Sample data for a period of eight days.

In comparison to the relative displacement Δx between the reference chambers in x-direction, the relative displacement Δy between the reference chambers in y-direction (a change in the vertical distance between the chambers, see figure 4.14) shows a maximum variance of 20 μm over the timespan of eight days. The 24-hour structure is again visible.

The relative displacement Δy between the reference chambers can essentially be divided in two stable bands, each stable to about 5 μm and separated by 5-7 μm. These "bands" belong to the same periods of stability encountered when examining the relative displacement Δx. In general, the relative position of the reference chambers seems to be more stable in y-direction, even though still exceeding the stability limit.

The relative movement Δz of the reference chambers with respect to each other along the direction of the anode wires of the drift tubes (the z-direction, see figure 4.14) is presented in figure 4.17. This relative displacement varies about 15 μm at maximum and generally stays within the stability limit for the whole timespan shown, apart from some spikes of about 5 μm, for instance around 100 hours. Some features of the 24-hour structure can also be identified for displacements Δz, but this structure is less clear than for instance the one of the displacements Δx shown in figure 4.15.

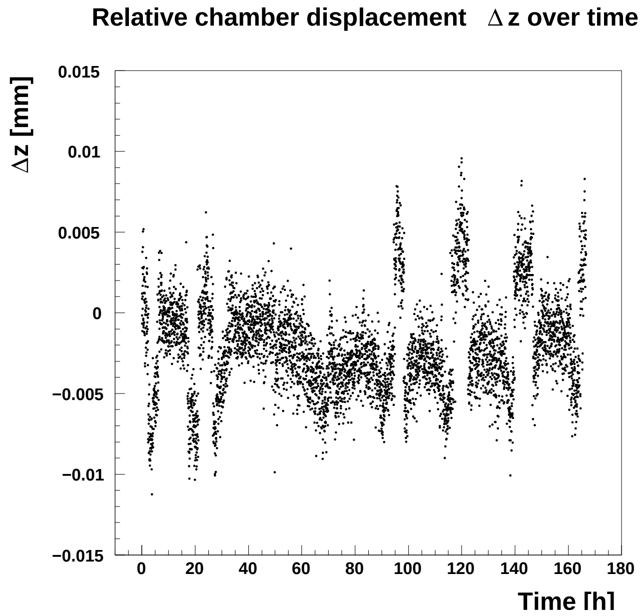

Figure 4.17: Relative displacements Δz (see figure 4.14) between the reference chambers. Sample data for a period of eight days.

Relative chamber displacements Δz have little to no impact on the measurements conducted with cosmic rays at the test-facility. The stability of relative z-position of the reference chambers can therefore not be exploited. With high certainty no correction of cosmic-ray data acquired will ever have to be corrected for displacements Δz.

The angles of the relative rotations between the reference chambers are visualized in figure 4.18 to figure 4.20. For all relative rotations R^x, R^y and R^z

around each of the global coordinate axes a stable band of about 5 μrad width can be seen which extends itself over the whole period data are shown for.

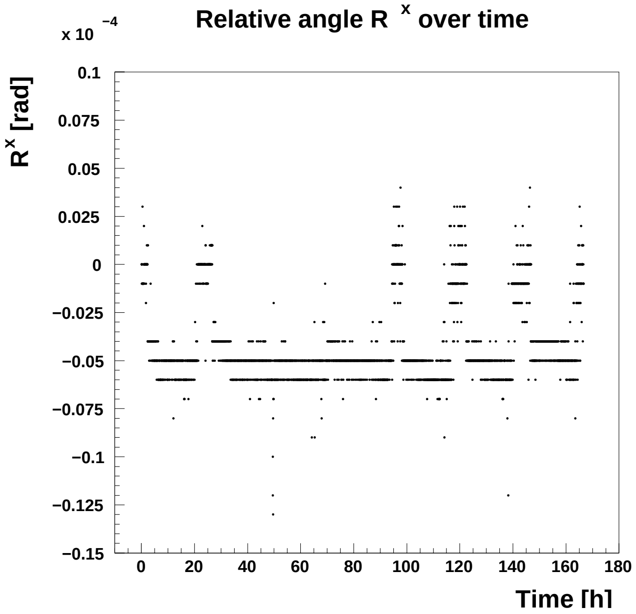

Figure 4.18: Relative rotation angle R^x (see figure 4.14) between the reference chambers. Sample data for a period of eight days.

Some spikes leaving the stable "bands" can be seen. The maximum variation of the relative rotation R^x around the x-axis is 10 μrad, it is 15 μrad for R^y and 20 μrad for R^z. Nonetheless relative chamber displacements between the reference chambers caused by relative rotations between them have to be taken into account.

The picture of relative displacements between the reference chambers emerging from the plots presented in this section is the following: The reference chambers move relative to each other mainly in the x- and y-direction. The movement in z-direction is negligible for the reason of being small and for the reason that this displacement has no impact on the cosmic-ray data. Rotation angles between the chambers are relatively stable over long periods.

The relative displacements Δx and Δy in x- and y-direction are of such a magnitude that they cannot be neglected. It was shown in section 4.2.2 that the reference chambers can be regarded as mechanically stable over periods of several days. Their individual deformations are so small that they do not have an impact on displacements measurements conducted with the reference alignment system. The displacements seen in the plots presented in this section are presumably caused by a movement of the whole chamber support structure. The upper part of the structure is mechanically coupled to the test-facility walls. The mechanical coupling is such that it leaves the possibility for the chamber support "tower" to be diagonally tilted around its base, away from the test-facility walls the tower is fixed to.

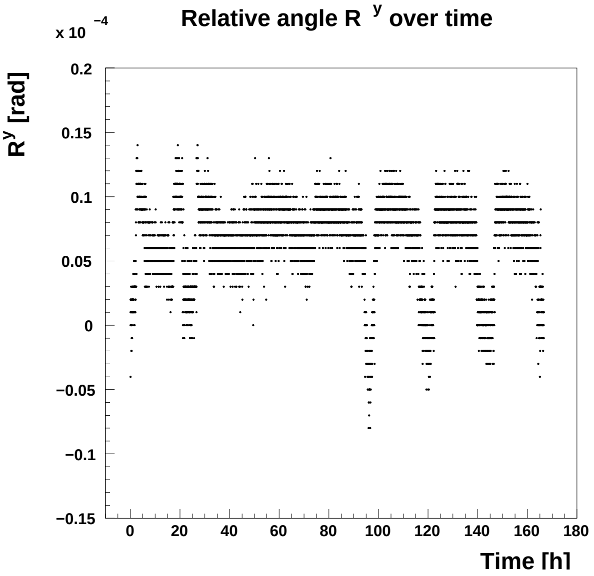

Figure 4.19: Relative rotation angle R^y (see figure 4.14) between the reference chambers. Sample data for a period of eight days.

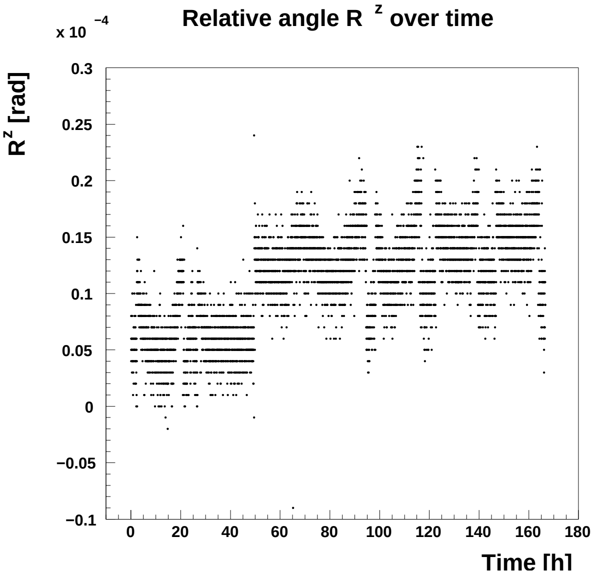

Figure 4.20: Relative rotation angle R^z (see figure 4.14) between the reference chambers. Sample data for a period of eight days.

Such a movement of the chamber support tower is consistent with the data shown throughout this section. It is also quite probable, since direct and indirect (through the test-facility windows on the opposite side) sunlight reaches the test-facility walls where the support tower is fixed from sunrise to sundown. A thermal expansion of the walls would be transmitted to the support tower through their mechanical coupling.

Measurements of the movement of the upper part of the chamber support tower were already thought of and tests have been made, but no measurement has been consequently carried out yet. It is the authors opinion that such a measurement would help to clarify the picture of relative chamber displacements between the reference chambers since a movement of the chamber support tower offers a consistent explanation for the measured displacements.

As there are no temperature sensors fixed either to the walls or to the chamber support tower, no relevant temperature plot to support the author's hypothesis can be presented here. Further investigations are needed.

Unfortunately it was not possible to check whether the program used by the author to produce the results presented in this section calculates relative displacements between reference chambers exactly mirroring the "real" relative reference chamber movements with respect to each other. The design of the chamber support structure was never meant to allow setting well-defined relative shifts between the reference chambers. No dial gauges can be tuned to pre-defined values thereby inducing well-defined displacements between the reference chambers which could then be reconstructed with the program to check if the "right" displacements are reconstructed. This means no systematic test of the program could be made because the reference chambers are not supposed to be moved once they have been installed with a lot of effort and care.

Nonetheless, it is possible to check if the displacement parameters reconstructed by the program are in one-to-one correspondence to displacements occurring in reality. If chamber displacements between the reference chambers occur during data-acquisition with the MDT chambers, shifts in their relative position can be calculated if cosmic-ray data acquired during periods of stability is compared to each other. This was shown by O. Kortner in his doctoral thesis [13].

A data-acquisition period of 10 hours is sufficient to calculate e.g. the relative displacement Δx between the reference chambers in x-direction to a precision of about 2 μm using cosmic-ray data [13]. For periods of 5 hours the achievable precision would be a factor $\sqrt{2}$ lower, i.e. still about 3 μm. Consecutive periods of stability of 5-10 hours time are regularly encountered, evidence for this claim is given in the plots of the reconstructed relative reference chamber displacements presented above.

It is already possible to select periods of time during which the relative chamber displacements stay below the 5 μm limit of mechanical stability (see above). Analyzing cosmic-ray data for consecutive periods of stability and comparing the results for both periods will reveal the “real” displacement shifts between the reference chambers. These can then be compared to the relative reference chamber displacements reconstructed with the program used above. Should both methods yield the same result the possibility to use analyzed cosmic-ray data acquired during any period of time will be opened up. Then it will be possible to correct for relative displacements between the reference chambers occurring between periods of stability through the use of the optical reference alignment system and its analysis program.

This test could not yet be done since the reference MDT chambers were not fully equipped and tested with the read-out electronics needed. The test will be conducted as soon as the reference MDT chambers installed at the cosmic-ray test-facility are ready for data acquisition.

Chapter 5

Calibration of the Capacitive Alignment System

After the explanation of measurement, modelling and reconstruction of possible deformations of muon chambers and of possible relative displacements between the reference chambers in chapter 4 this chapter will focus on the calibration of the capacitive probes.

Let us recall that these capacitive probes are the instruments used for the alignment monitoring of the test chamber with respect to the upper reference chamber. The concept of capacitive displacement measurement, the layout of the capacitive alignment system and the precision which in principle can be achieved have been pointed out in section 3.2. Now we will explain how the probes are calibrated.

During the process of this explanation the choice of the nominal vertical distance between probes and targets should become clear. Also, the achievable precision will be a natural result of the calibration procedure, just like the algorithm which later on can be used to determine actual displacements.

5.1 The Capacitive Probe Calibration Stand

For the calibration of the capacitive probes a calibration stand designed by A. Kraus specifically for this purpose is used. Its schematic layout is shown in figure 5.1.

The grounded metal target as well as the sensor support are fixed to an aluminum support structure sitting on little rails. Sensors and target slide easily on these rails when moved with the aid of micrometer screws. The scale division of both micrometer screws is 2 μm which conservatively sets the upper limit on for the precision with which displacements can be set.

As can be seen in figure 5.1 “vertical” displacements (displacements in y-direction) are caused by moving the sensor support whereas horizontal displace-

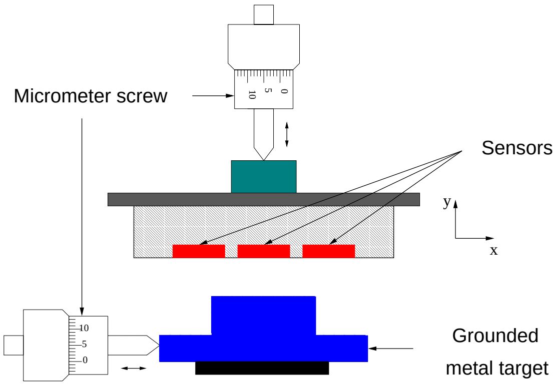

Figure 5.1: The capacitive probe calibration stand for the capacitive alignment system.

ments (displacements in x-direction) are induced by moving the target. The target has to be connected to the common ground connector of the amplifier card rack for the voltage reading of the sensors to be stable to about 1 millivolt. Originally no ground connection was made leading to oscillations of the output voltages. This effect had previously not been observed, so the author suspected a missing mass connection to be the cause. The problem could be easily fixed by providing the mass connection mentioned above.

For the calibration of the probes software had specifically been developed. This software was programmed by A. Kraus and is described in his thesis [27]. The measurements made for his diploma thesis did not include a full calibration of the sensors. In attempting this procedure serious inconsistencies arose, requiring a thorough investigation of his program. With the help of J. Dubbert the author corrected several fatal errors in the code. These errors, however, could not have been revealed by the measurements described in [27].

5.2 Analysis of the Calibration Data

Before we begin with the analysis of the calibration data, let us recall what "calibration" means in the context of the capacitive alignment system. The system is meant to measure vertical and horizontal displacements. The sensor output is, however, not a distance but a voltage varying with the distance sensor-target. It is the aim of the calibration to correlate the sensor output voltages to vertical and horizontal sensor-target positions in order to calculate relative displacements from these.

The calibration data can be subdivided into two sets of data. The analysis of both sets shares a common analytical approach. One set of data belongs to the sensors which are only vertically sensitive, namely those located directly over the step of the metal target. The other set of data belongs to the sensors located over the edges of the step of the metal target. These are horizontally sensitive. We will start out with the data analysis of the "vertical" sensors.

5.2.1 Vertically Sensitive Sensors: A One-Dimensional Linear Interpolation

Figure 5.2 shows an example plot for one of the vertically sensitive sensors. Sensor output voltages have been recorded for vertical distances in a range of 3 to 7 mm between the sensors and the metal target. The vertical distance between data points corresponds to 50 μm.

A close look at this plot showing actual calibration data reveals that the dependence of the sensor output voltage on the vertical position is not linear over the whole vertical distance covered by the calibration[1].

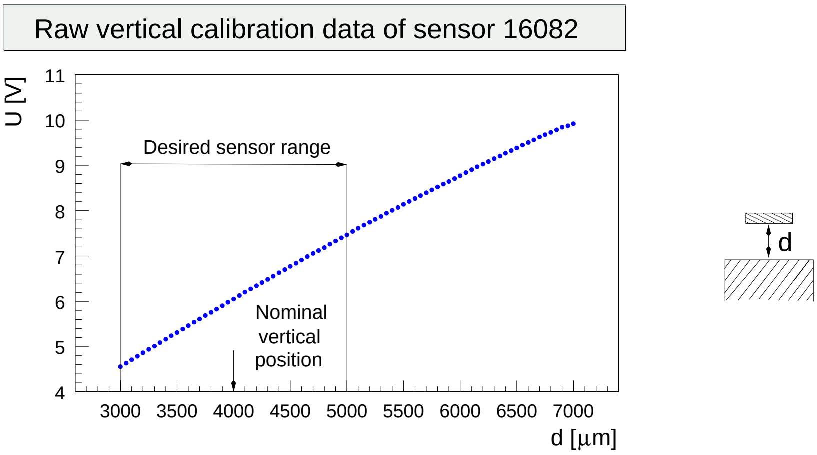

Figure 5.2: Sensor output voltage in dependence of the vertical distance between sensor and metal target. Sample data for one of the vertically sensitive sensors.

Unlike analytical approaches made before ([27],[13]) the author chose not to try a polynomial fit to the vertical calibration data. For a 2 mm wide interval around a working distance of 4 mm a polynomial fit to the calibration data has been used by O. Kortner. In order to achieve a standard deviation from the mean zero of about 2 μm a polynomial of fifth degree had to be fitted to the data [13]. The analysis of A. Kraus employed a polynomial of eighth degree to fit the calibration data for distances in an interval of 9 mm with a precision of $\pm 4 \mu m$ [27].

---

[1] According to the producer-supplied information the probes should be linear for vertical distances in the range of 0-7 mm. The amplifier circuitry generating the output signal voltage should be linear to 2%.

The author's goal was to analyze the data recorded in the simplest possible way offering the needed precision. A linear fit over the total range of 4 mm did not offer the precision wanted. However, locally the course of the raw data curve seemed to be adequately linear. This opened up the possibility to locally describe the course of the curve by linearly interpolating between two neighboring points. The formula used for linear interpolation is listed in appendix B.

The following was done to test if the linear interpolation described by equation (B.2) yields the precise vertical position $y(U)$. Two calibration data points (U^M_{k-1}, y^M_{k-1}) and $U^M_{k+1}, y^M_{k+1})$ being the direct left and right neighbors of a third point (U^M_k, y^M_k) also recorded during calibration were used to interpolate its vertical position $y(U^M_k)$:

$$y(U^M_k) = y^M_{k-1} + \frac{y^M_{k+1} - y^M_{-1}}{U^M_{k+1} - U^M_{k-1}}(U^M_k - U^M_{k-1}). \tag{5.1}$$

Then the residual

$$Res_{vertical} = y^M_k - y(U^M_k) \tag{5.2}$$

was calculated. It is a measure for the absolute deviation of the interpolated vertical distance $y(U^M_k)$ from the real vertical distance y^M_k set during the calibration data take.

The procedure described above allows to interpolate vertical positions y using the calibration data and to compare these to data actually measured. Figure 5.3 shows the residuals for all vertically sensitive sensors over the whole range calibration data was recorded for. The mean of the residuals is in agreement with zero and their root-mean-square deviation is less than or equal to 3 μm for all of them. This deviation drops to less than 1 μm if only a range of ±1 mm around the nominal vertical sensor-target distance of 4 mm is considered. This sets the upper limit for the achievable precision.

Sensor No.	Vertical range $3 - 7$ mm		Vertical range $3 - 5$ mm	
	Mean [μm]	RMS [μm]	Mean [μm]	RMS [μm]
16075	-0.38	2.58	-0.07	0.83
16077	-0.31	2.00	-0.04	0.74
16080	-0.42	3.04	-0.04	0.79
16082	-0.18	1.81	-0.06	0.81

Table 5.1: Precision of the vertical position reconstruction by linear interpolation. All vertically sensitive capacitive sensors are shown.

Therefore, we conclude that linear interpolation using the calibration data as a look-up table and employing equation (B.2) yields the exact vertical positions

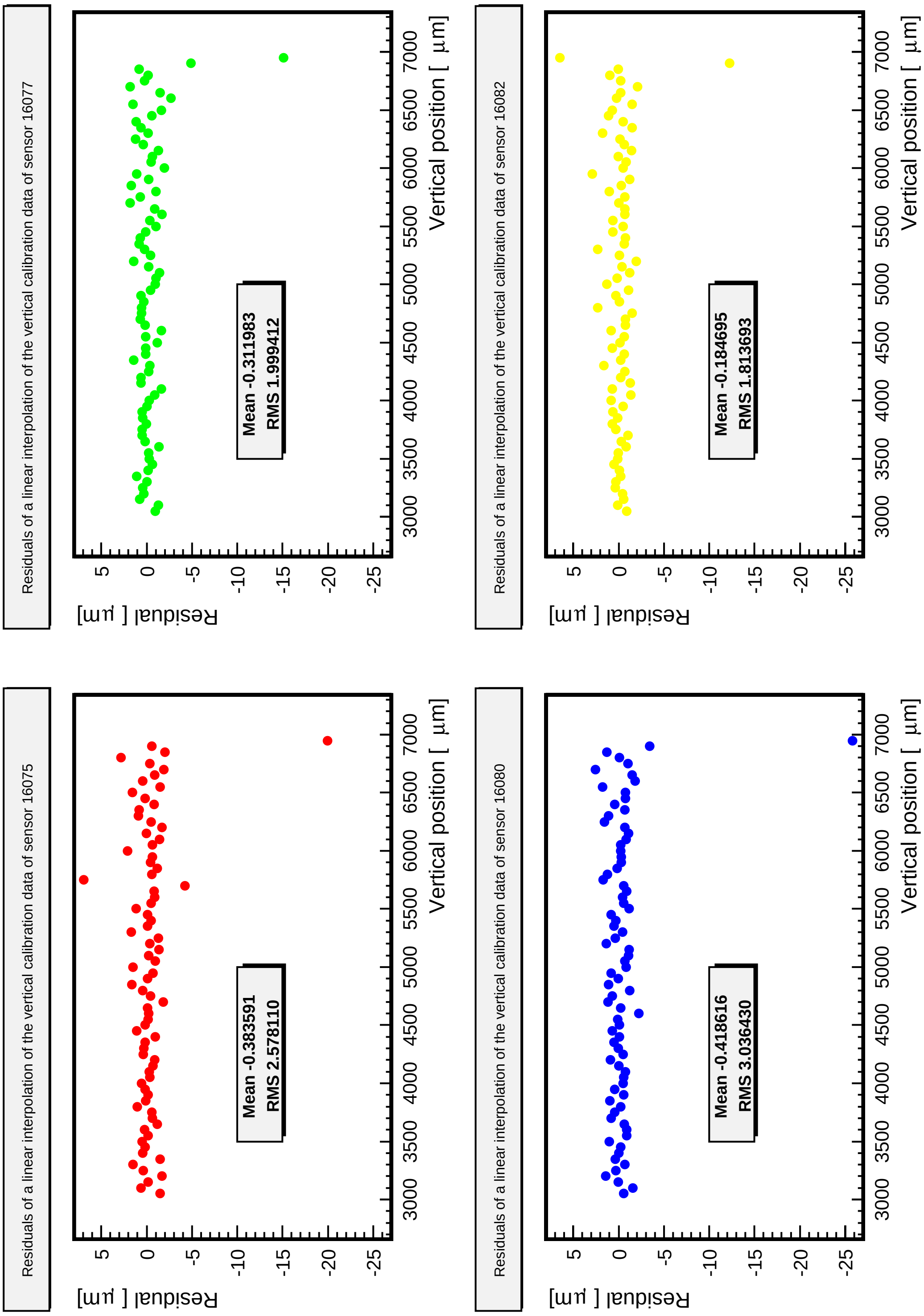

Figure 5.3: Residuals of a linear interpolation for the vertically sensitive sensors.

y from the measured output voltage U. The precision achieved is about 1 μm. Results are also summarized in table 5.1.

5.2.2 Horizontally Sensitive Sensors: A Two-Dimensional Linear Interpolation

The preceding section 5.2.1 has proven that vertical distances can be calculated from the output voltages of the vertically sensitive sensors using a simple linear interpolation algorithm. The precision achieved with this algorithm is such that it seems possible to use a two-dimensional linear interpolation algorithm for the analysis of the horizontal calibration data.

A look at raw data from the horizontally sensitive sensors will tell whether this approach makes sense at all. Figure 5.4 displays horizontal calibration data of the two sensors sensitive to horizontal movements of one of the triplets. The x-axis shows the horizontal positions, the y-axis the vertical positions. The “surface” of the recorded output voltages $U(x, y)$ looks smooth and at least locally linear enough in both x and y to try a two-dimensional linear interpolation by simply expanding the approach made in the previous section 5.2.1 to two dimensions.

The data visualized in figure 5.4 was recorded as follows: For a well-defined pre-set vertical distance y the horizontal position x of the sensor triplet was incremented in 100 μm steps in the range of 0 to 5.5 mm. For each step the output voltages of both horizontally sensitive sensors were recorded. This procedure was repeated for 21 equidistant vertical positions y being 200 μm apart and ranging from 3-7 mm. All the horizontal calibration data for one sensor and one pre-set vertical distance y make up a so called y-slice of calibration data.

Simply speaking, sensor output voltages have been recorded for each point of a calibration data grid segmented in 100 μm × 200 μm rectangles. How is it possible to determine the horizontal position from this data grid? The approach is visualized in left part of figure 5.5 and the formulas of the interpolation procedure are listed in appendix B.

In analogy to the procedure described in section 5.2.1 used to test if the linear interpolation yields the precise vertical distance, a test of the linear interpolation in two dimensions (equation (B.5) to equation (B.8)) has been made. The right hand side of figure 5.5 schematically shows how this test was done.

For test purposes the well-known horizontal position x_k^M belonging to the calibration data point $U_k^M(x_k^M, y_k^M)$ with

$$x_{k-1}^M \leq x_k^M \leq x_{k+1}^M \tag{5.3}$$

and

$$y_{l-1^M} \leq y_l^M \leq y_{l+1}^M \tag{5.4}$$

of a horizontally sensitive sensor is compared to its interpolated horizontal position $x(U_k^M, y_l^M)$.

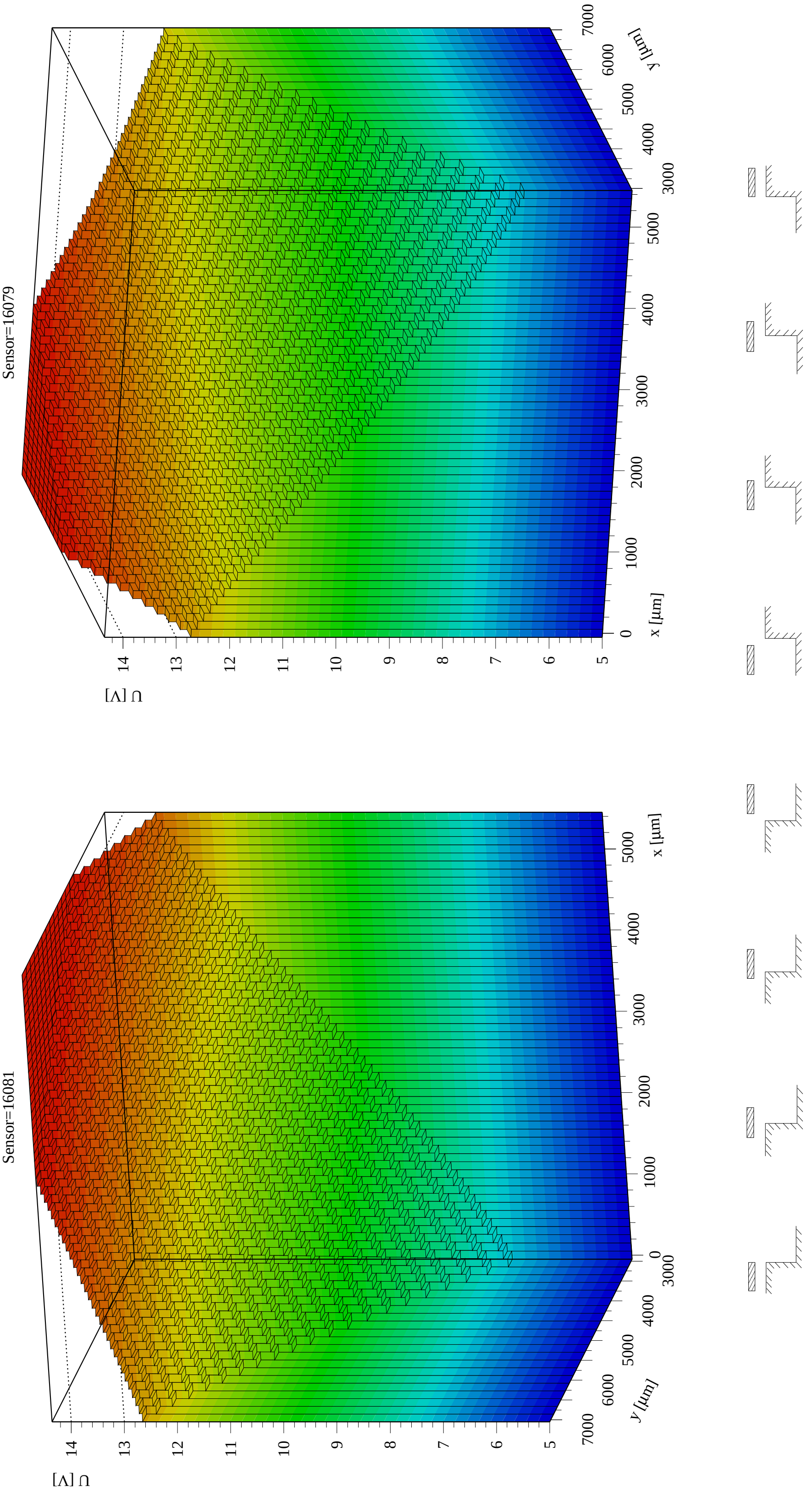

Figure 5.4: Sensor output voltage in dependence of the horizontal position x for different vertical sensor-target distances y. Raw calibration data for both horizontally sensitive sensors of one triplet is shown. Below the x-axis the horizontal position of each sensor over the edge of the metal step is denoted. Sensors reaching their saturation voltage cause the voltage plateau above 14 V.

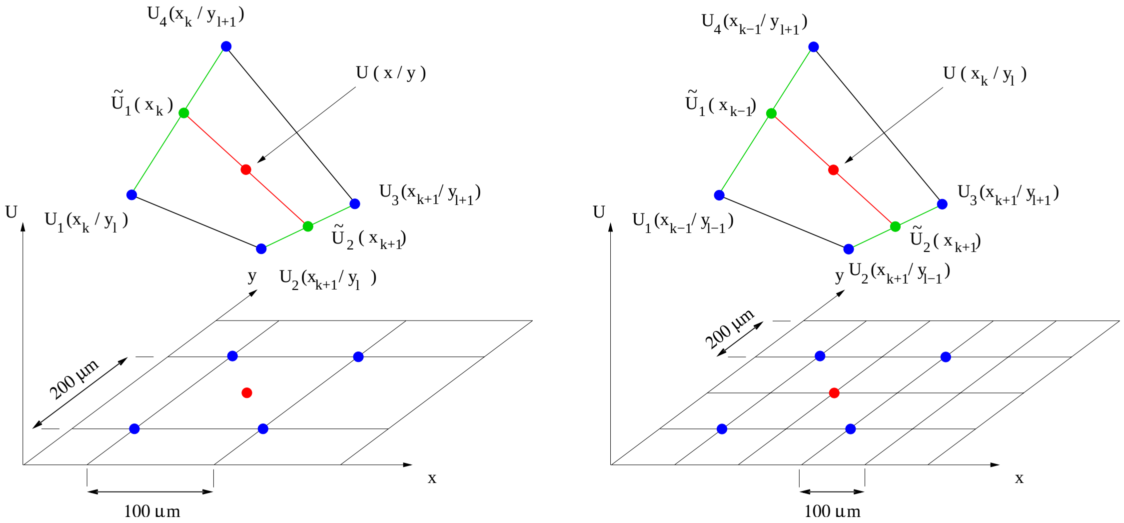

Figure 5.5: Schematics of the two-dimensional interpolation procedure used to determine the horizontal position of a sensor triplet with respect to the metal target. Left: Basic interpolation procedure. First $\tilde{U}_1(y)$ and $\tilde{U}_2(y)$ are interpolated between two neighboring y-slices (green), then both values are used to determine the x-position of the center point (red). Right: Test of the interpolation procedure with recorded data. First $\tilde{U}_1(y)$ and $\tilde{U}_2(y)$ are interpolated between the y-slices y_{l-1} and y_{l+1} (green), then both values are used to determine the x-position of the center point (red).

All points x_k^M and y_l^M are elements of the calibration data grid $\forall\ k, l$.

First $\tilde{U}_1(y_l^M)$ and $\tilde{U}_2(y_l^M)$ are calculated as described in equation (B.5) and equation (B.6). The horizontal sensor position $x(U_k^M, y_l^M)$ is then given by

$$x(U_k^M, y_l^M) = x_{k-1} + \frac{x_{k+1} - x_{k-1}}{\tilde{U}_2 - \tilde{U}_1} \cdot (U_k^M - \tilde{U}_1). \tag{5.5}$$

Again a residual

$$Res_{horizontal} = x_k^M - x(U_k^M, y_l^M) \tag{5.6}$$

is calculated. This time it is a measure for the absolute deviation of the interpolated horizontal position $x(U_k^M, y_l^M)$ from the actual horizontal position x_k^M set during the calibration data take.

And again it is possible to compare horizontal positions actually set and measured during the calibration data aquisition to horizontal positions x interpolated using the calibration data. Before we take a look at the results the method described above yields we will take the time to think about different strategies to determine the horizontal position of a sensor triplet.

The reader might have noticed that the vertical distance y between the sensor triplet and the target has to be known beforehand in order to be able to apply the two-dimensional interpolation algorithm described above. The previous section 5.2.1 has shown that this is achieved with an accuracy better than 1 μm by applying equation (B.2) to the sensor readings of the vertically sensitive sensors. Therefore the vertical triplet-target distance y and the output voltage of both of the horizontally sensitive sensors are available as variables for equation (B.8).

Apart from the one vertically sensitive sensor two horizontally sensitive sensors belong to one triplet. Thus it is in principle possible to interpolate two horizontal positions, one for each sensor. This has the advantage that it is possible to calculate a horizontal triplet-target position even when one of the sensors has reached its saturation voltage and is thus no longer sensitive to horizontal movements. Sensors reach their saturation voltage for large vertical triplet-target positions combined with the saturated sensor being located over the base of the step instead of over its edge. When this happens however, the other horizontally sensitive sensors is located right over the edge of the step and hence is sensitive. Figure 5.4 visualizes this effect.

One possible strategy to determine the horizontal triplet-target position thus is to calculate the mean of the horizontal positions of both sensors of one triplet in the range where both of them are sensitive. Whenever one sensor is no longer sensitive because of its horizontal position with respect to the edge of the step only the interpolated horizontal position of the sensitive sensor is used.

Still, another strategy exists to determine the horizontal triplet-target position. It is possible to define

$$U_{\text{diff}} = U_{\text{Sensor1}} - U_{\text{Sensor2}} \tag{5.7}$$

to be one output voltage of both horizontally sensitive sensors of a triplet.

On the left hand side figure 5.6 shows the course of the calibration data curves of both sensors for one y-slice. The right hand side of the figure visualizes the voltage difference U_{diff} of both sensors shown. Now U_{diff} together with the already calculated vertical distance y (look above) can be taken as an input to the two-dimensional interpolation described in equation (B.5) to equation (B.8). The horizontal position can thus be determined by interpolating only once. The averaging over interpolated horizontal sensor positions is no longer needed and absorbed into calculating U_{diff}.

Both strategies have been implemented in a C++ program by the author. It seemed the best way to decide which strategy yields the best result in terms of numerical stability and precision possible. Offhand, there are some advantages of the second approach over the first. The interpolation algorithm is only used once, errors due to the algorithm are therefore only made once instead of twice. No averaging over sensors has to be done, too. In all, the second approach is simpler than the first.

Although both strategies in principle yield the same results over wide ranges,

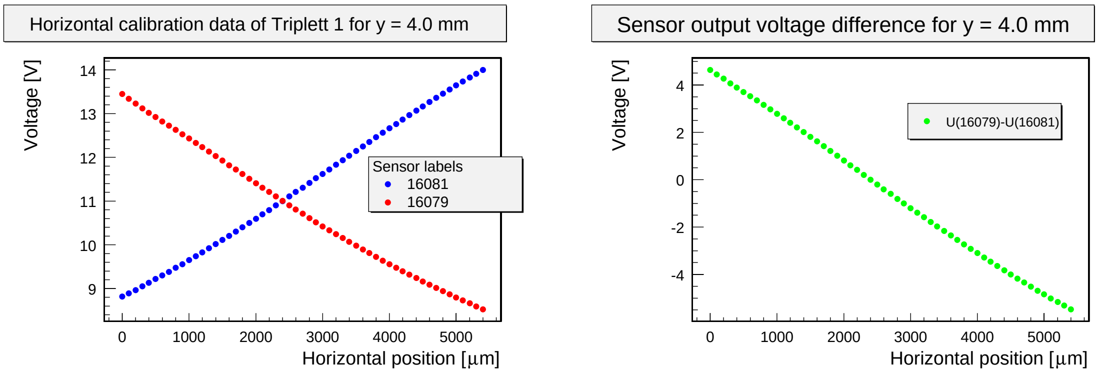

Figure 5.6: Example of horizontal raw calibration data of one triplet for one y-slice. Left: Output voltages of both horizontally sensitive sensors in dependene of the horizontal position x of the sensors for the 4 mm y-slice. Right: Voltage difference $U_{\text{diff}} = U_{16079} - U_{16081}$ in dependence of the horizontal position x of the triplet for the 4 mm y-slice.

the second strategy presented provides better precision. Apart from the fact that the interpolation is only done once, this is due to the fact that the effect of possible noise is compensated when U_{diff} is calculated. It is very probable that noise is correlated for all sensors of a triplet, so subtracting the output voltage of one horizontally sensitive sensor of a triplet from the other in effect leads to a cancellation of the noise effects. The calculation of U_{diff} thus yields a smoothened voltage curve allowing to achieve a better precision because of the better linearity of U_{diff} as compared to the individual output voltages of both horizontally sensitive sensors.

Figure 5.7 visualizes the residuals between the horizontal positions x actually set for one triplet during the calibration data acquisition and the interpolated horizontal positions. These positions have been interpolated using U_{diff} (the second approach described above). The residuals have been calculated using equation (5.6). The range of the horizontal values was limited to ±1 mm around the nominal horizontal target position of about 2350 μm[2].

Not all residual plots for the triplet are shown. We limit ourselves to showing the residuals for the nominal vertical sensor-target distance of 4.0 mm and to the plots from the borders of the ±1 mm vertical working range around it. The nominal vertical triplet-target distance has been chosen after plotting all residuals for a horizontal range of ±1 mm and the full vertical range of 3-7 mm calibration data was recorded for. Examination of the residuals together with the requirement to have a vertical working range of ±1 mm around the nominal vertical triplet-target distance led to this choice.

---

[2] The nominal horizontal target position of 2350 μm is imposed by the geometry of the capacitive probe calibration stand.

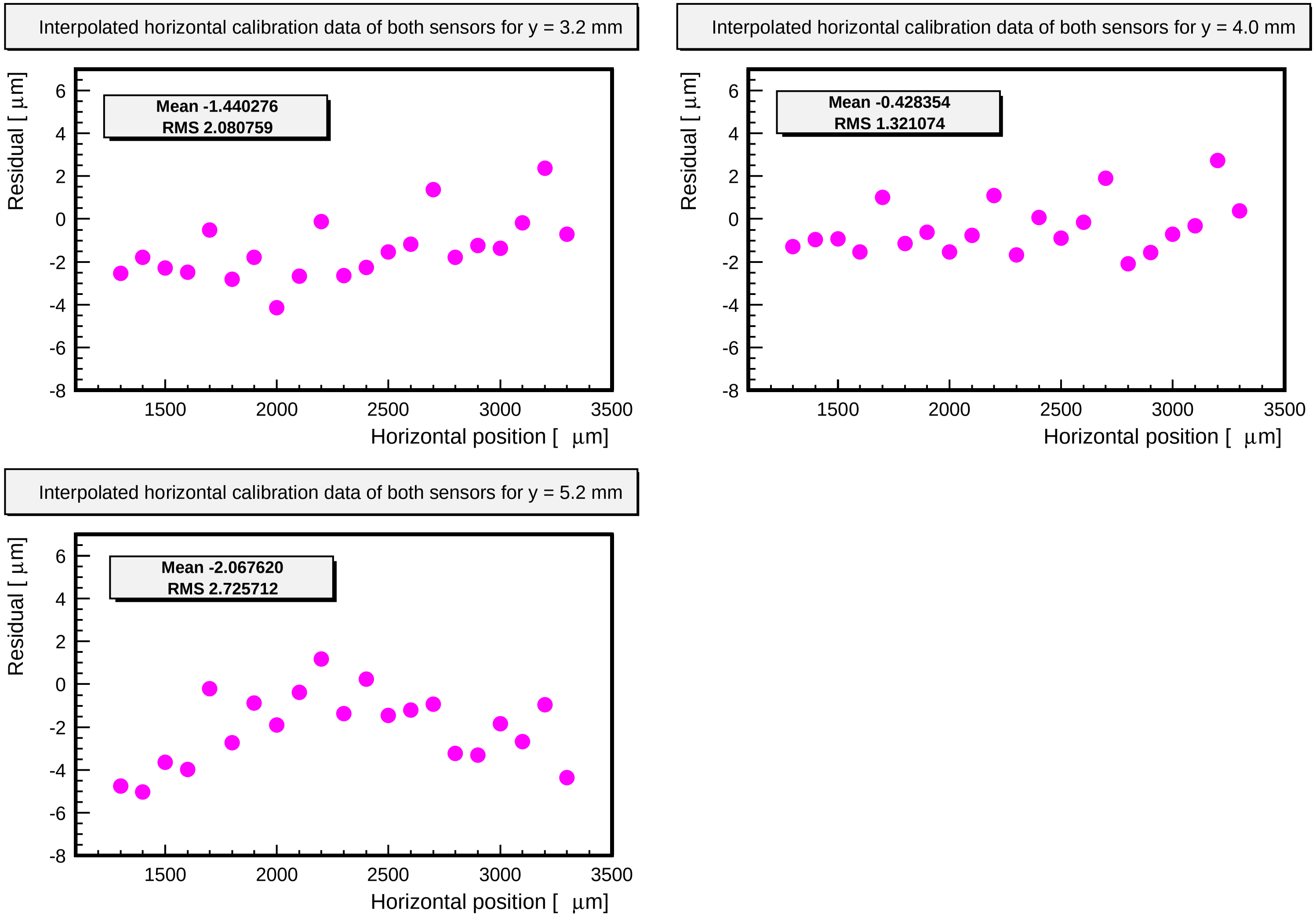

Figure 5.7: Residuals of a two-dimensional linear interpolation for the horizontally sensitive sensors of one triplet. The r.m.s. value indicated is the actual spread of the data around zero. The plot in the upper right corner is for the nominal vertical triplet-target distance of 4.0 *mm*. The other plots show the residuals at the borders of the chosen working range.

When we take a look at the residuals in the plots of figure 5.7 we notice a small systematic deviation of the mean value from zero. It is small enough to be negligible. The root-mean-square deviation value shown was calculated for a set mean value of zero. This means the r.m.s. value given is the absolute deviation of the residuals from zero. It sets the upper limit for the achievable precision, in this case 2.7 μm for a vertical and horizontal working range of ± 1 mm around the nominal triplet-target position (also see table 5.2).

Although a full set of analyzed calibration data exists for the second triplet, it will not be shown here. The analysis strategy and the interpolation algorithm employed were exactly the same. The author would nonetheless have liked to present the results of the analysis for the second triplet as well. During the analysis procedure the author noticed that one sensor belonging to the second triplet yielded output voltages that were significantly different from the other seven sensors. The raw calibration data plot of the output voltage in dependence of the horizontal distance shown in figure 5.8 reveals that the course of the voltage curve is not as steep as all other curves are and that the saturation voltage lies below 13 V instead of above 14 V.

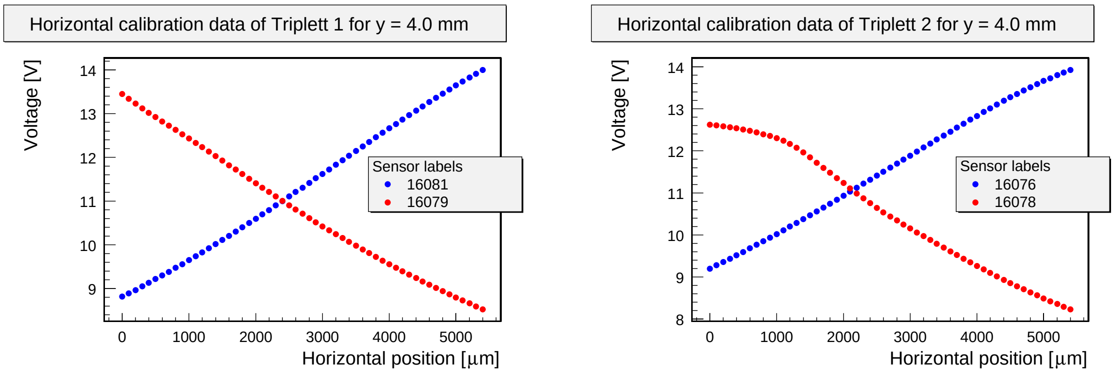

Figure 5.8: Comparison of horizontal raw calibration data of both triplets for one y-slice. Left: Output voltages of both horizontally sensitive sensors in dependence of the horizontal position x of Triplet 1 for the 4 mm y-slice. Right: Output voltages of both horizontally sensitive sensors in dependence of the horizontal position x of Triplet 2 for the 4 mm y-slice. Note how the voltage curve of sensor 16078 (red) has a significantly different course from the one of the curve of sensor 16079 (also red) on the left hand side.

By connecting the sensor to another amplifier card the author verified that this problem is most probably due to a faulty adjustment of the amplifier (offset, gain and drive can be adjusted). The sensor itself behaved just as all other sensors when connected to another amplifier card. Of course the problem can be solved by readjusting the parameters of amplification circuit. Since we do not have the means to do this ourselves, the amplifier card will be sent to the manufacturer for recalibration.

Still, we conclude that by following the second analysis strategy the two-dimensional linear interpolation algorithm contained in equation (B.5) to equation (B.8) together with the use of the calibration data recorded as a look-up table yields the actual horizontal triplet-target position x from the measured output voltage U and the interpolated vertical position y. The precision achieved is better than 3 μm. The results are summarized in table 5.2.

Vertical triplet-target distance [mm]	Residual	
	Mean [μm]	RMS [μm]
3.2	-1.44	2.08
3.4	0.38	1.26
3.6	-1.12	1.99
3.8	-0.88	1.44
4.0	-0.43	1.32
4.2	-1.35	1.95
4.4	1.41	2.00
4.6	-0.11	1.44
4.8	-0.27	1.62
5.0	0.26	2.62
5.2	-2.07	2.72
5.4	-1.36	3.18
5.6	-1.45	3.56
5.8	-0.76	1.87
6.0	-4.46	5.12
6.2	-1.27	5.42
6.4	4.76	24.33
6.6	5.97	28.95
6.8	-2.40	30.36

Table 5.2: Precision of the horizontal position reconstruction by two-dimensional linear interpolation for the horizontal working range. Data is shown for Triplet 1 only. The r.m.s value given is the absolute deviation of the residuals from zero. Data is shown for the whole range of vertical triplet-target distances, the rows colored light gray just show data for the selected vertical working range.

Chapter 6

Conclusion and Outlook

Alignment monitoring of MDT chambers at the Munich Cosmic-Ray Test-Facility through the use of optical and capacitive alignment systems has been the focus of the studies presented in this thesis.

An optical alignment system based on the RasNiK principle monitoring possible relative displacements between the reference MDT chambers has been set up by the author. The setup procedure revealed that the mechanical precision of all parts of each the optical-element support-structures is crucial for systems intended for measurements with an accuracy of a few micrometers. The reference alignment system has been used to monitor actual displacements between the reference chambers.

Additionally, the in-plane alignment system of each MDT chamber, which is also based on the RasNiK principle, has been employed to monitor the individual chamber geometry of each of the installed chambers.

As both systems are based on the same principle, they both showed a sensitivity to direct and stray light leading to a rapid degradation of the image quality, although an infrared light source and infrared filters are used in the standard design. Adequate light shielding allowed continuous and reliable operation of both systems. This issue will also have an impact on the alignment of the muon chambers at the ATLAS experiment, since it is foreseen to use RasNiK-based alignment systems already during the installation of the chambers. Without proper light shielding a reliable operation of these systems cannot be counted on.

The intrinsic resolution of each of the RasNiK monitors installed at the Cosmic-Ray Test-Facility - whether of the reference or of the in-plane alignment system - has been determined using the so called “multiple image” method. For both optical systems the resolution for displacements of optical elements along the optical axis is of the order of 100 μm and can therefore not be used to monitor deformations and displacements on the micrometer scale.

The intrinsic resolution of the in-plane RasNiK monitors for optical element displacements perpendicular to the optical axis has been found to be better than 1 μm in agreement with previous studies. For the RasNiK monitors of the reference alignment system the intrinsic resolution for these kind of displacements was determined to be about 3 μm. As individual chamber deformations and relative displacements between the reference chambers below a limit of 5 μm over a time of 20 hours can be neglected, one can conclude that the intrinsic resolution of both systems is sufficiently good to detect deformations and displacements exceeding the stability limit.

Individual chamber deformations have been reconstructed with a modified program developed by A. Ostaptchuk. In-plane alignment system data analyzed with this program have proven an excellent mechanical stability over a period of days of an individual chamber installed at the test facility. Deformations stay below the critical 5 μm limit. Regarding the chambers as rigid bodies when reconstructing relative displacements between them is therefore a valid assumption. Furthermore, individual chamber deformations are small enough not to have an influence on the geometry of the reference alignment system directly mounted on the chambers.

An analysis program to reconstruct the relative displacements between the reference chambers from the reference alignment system data has been developed for this thesis in cooperation with A. Ostaptchuk. It is based on the same algorithm as the program used for the data analysis of the in-plane system. It is extendable to a setup with a total of five chambers (3 chambers to be tested and 2 reference chambers) and allows to include the reconstruction of the relative displacements between the upper reference chamber and the test chamber using the capacitive alignment system data. Thereby it will in future be possible to reconstruct the relative chamber position of all chambers installed at the test facility with one program using one principle.

The analysis of the reference alignment system data has shown that relative displacements between the reference chambers normally exceed the stability limit during the 20 hours needed to acquire cosmic-ray data. Therefore the reference alignment system is absolutely indispensable to select periods of stability. It can be assumed that the movement of the chamber support tower causes these relative displacements because of its mechanical coupling to the test-facility walls subject to thermal expansion. Further investigations like measurements with a laser interferometer could help to classify and quantify the cause of the relative displacements between the reference chambers.

Tests of the program used for reconstruction of relative displacements between the reference chambers have to be conducted in future. No mechanical means allowed setting well-defined relative displacements which could then be reconstructed. A test of the program is nevertheless possible by comparing displacements reconstructed with the program and displacements calculated using cosmic-ray data. This test should be undertaken as soon as the reference chambers are fully equipped with read-out electronics.

For the purpose of monitoring relative displacements between the upper reference chamber and the test chamber a capacitive alignment system is employed at the Cosmic-Ray Test-Facility. Calibration data for each of the capacitive probes has been acquired and analyzed. Two interpolation algorithms were developed and tested during the analysis of the calibration data. It has been shown that these algorithms are stable and produce reliable results, allowing to reconstruct relative vertical displacements between test and upper reference chamber with an accuracy of about 1 μm through linear interpolation using the calibration data. It has furthermore been shown that two-dimensional linear interpolation using the calibration data allows reconstruction of relative horizontal displacements with an accuracy better than 3 μm. The capacitive alignment system is now ready and operational. This system can now also be used to align the test chambers relative to the upper reference chamber upon their installation.

It can therefore be concluded that the alignment systems at the Cosmic-Ray Test-Facility have all been set up and are now fully and reliably operational. Data analysis programs have been developed which allow to include all systems. Their functionality has been tested and proven, although a final test of the results still remains to be undertaken. Finally, it can safely be said that alignment monitoring is indispensable for the success of the chamber tests with cosmic rays, even though the overall stability of the whole setup is very good.

Appendix A

Intrinsic Resolution of the In-Plane Alignment Systems

This appendix lists the intrinsic resolution of all in-plane RasNiK monitors of both reference chambers and the test chamber currently installed at the Munich Cosmic-Ray Test-Facility. The intrinsic resolution of all reference alignment system RasNiK monitors is fully documented in tables 4.3 and 4.4 presented in chapter 4.

The intrinsic resolution of each in-plane monitor for the x-, y- and z-coordinate measurements is given by the σ_x, σ_y and σ_z, respectively, of a χ^2 fit with a Gauss function. The "multiple image" method described in section 4.1 was used to determine the resolutions listed. Data analysis was carried out in exact analogy to the procedure described in that section. Unless otherwise stated data are shown for 140 consecutive measurements with each monitor.

A.1 Intrinsic Resolution of the In-Plane Alignment Systems of the Upper Reference Chamber BOS2C10

Channel Name	x-coordinate		y-coordinate		z-coordinate	
	Mean [μm]	σ_x [μm]	Mean [μm]	σ_y [μm]	Mean [μm]	σ_z [μm]
In-plane 1	0.00 ± 0.06	0.55 ± 0.04	-0.01 ± 0.04	0.43 ± 0.03	0 ± 24	207 ± 20
In-plane 2	0.01 ± 0.06	0.64 ± 0.04	0.00 ± 0.05	0.57 ± 0.04	-7 ± 40	410 ± 39
In-plane 3	0.01 ± 0.05	0.56 ± 0.04	0.00 ± 0.06	0.71 ± 0.05	24 ± 35	361 ± 28
In-plane 4	0.03 ± 0.05	0.50 ± 0.04	-0.03 ± 0.05	0.53 ± 0.05	19 ± 21	219 ± 16

Table A.1: Intrinsic resolution of all monitors of the in-plane alignment system of the BOS2C10 MDT chamber determined with the "multiple image"method. This chamber is the upper reference chamber at the Munich Cosmic-Ray Test-Facility.

A.2 Intrinsic Resolution of the In-Plane Alignment Systems of the Lower Reference Chamber BOS2C08

Channel Name	x-coordinate		y-coordinate		z-coordinate	
	Mean $[\mu m]$	σ_x $[\mu m]$	Mean $[\mu m]$	σ_y $[\mu m]$	Mean $[\mu m]$	σ_z $[\mu m]$
In-plane 1	-0.02 ± 0.03	0.34 ± 0.02	-0.02 ± 0.03	0.40 ± 0.03	0 ± 23	252 ± 18
In-plane 2	-0.02 ± 0.03	0.38 ± 0.03	-0.05 ± 0.04	0.47 ± 0.03	-22 ± 24	266 ± 23
In-plane 3[1]	0.07 ± 0.13	0.56 ± 0.11	-0.01 ± 0.10	0.58 ± 0.08	21 ± 140	496 ± 19
In-plane 4	0.06 ± 0.06	0.70 ± 0.07	0.06 ± 0.08	0.69 ± 0.07	-25 ± 59	541 ± 62

Table A.2: Intrinsic resolution of all monitors of the in-plane alignment system of the BOS2C08 MDT chamber determined with the “multiple image”method. This chamber is the lower reference chamber at the Munich Cosmic-Ray Test-Facility.

A.3 Intrinsic Resolution of the In-Plane Alignment Systems of the Test Chamber BOS4C16

Channel Name	x-coordinate		y-coordinate		z-coordinate	
	Mean $[\mu m]$	σ_x $[\mu m]$	Mean $[\mu m]$	σ_y $[\mu m]$	Mean $[\mu m]$	σ_z $[\mu m]$
In-plane 1	0.00 ± 0.03	0.38 ± 0.03	-0.03 ± 0.04	0.44 ± 0.04	-4 ± 21	220 ± 17
In-plane 2	-0.03 ± 0.04	0.44 ± 0.04	-0.05 ± 0.06	0.59 ± 0.05	11 ± 27	276 ± 23
In-plane 3[2]	-0.02 ± 0.06	0.50 ± 0.05	-0.01 ± 0.05	0.54 ± 0.04	-2 ± 38	333 ± 36
In-plane 4	-0.02 ± 0.05	0.55 ± 0.03	0.01 ± 0.06	0.64 ± 0.04	-10 ± 27	292 ± 26

Table A.3: Intrinsic resolution of all monitors of the in-plane alignment system of the BOS4C16 MDT chamber determined with the “multiple image”method. This chamber currently[3] is the test chamber at the Munich Cosmic-Ray Test-Facility.

---

[1] Of the 140 measurements only 102 were used to determine the intrinsic resolution of this monitor since the images of the other 38 measurements could not be analyzed properly by the analysis module. Possible reasons are given in chapter 4.

[2] Of the 140 measurements only 38 were used to determine the intrinsic resolution of this monitor since the images of the other 102 measurements could not be analyzed properly by the analysis module. Possible reasons are given in chapter 4.

[3] November 2002.

Appendix B

Linear Interpolation Procedures Employed for the Calibration of the Capacitive Probes

This appendix lists the formulas used for the calibration procedure of the capacitive probes. The calibration procedure itself is described in chapter 5. There calibration data and gained results are presented. Figure 5.5 included in chapter 5 might help to clarify the formulas of the two-dimensional linear interpolation (section B.2) employed for the calibration of the horizontally sensitive capacitive probes.

B.1 Vertically Sensitive Sensors: One-Dimensional Linear Interpolation

Let U be the sensor output voltage for a vertical sensor-target position y. If U_k^M and U_{k+1}^M are two neighboring calibration data points for which

$$U_k^M \leq U \leq U_{k+1}^M \tag{B.1}$$

holds true then the vertical sensor-target position $y(U)$ is given by

$$y(U) = y_k^M + \frac{y_{k+1}^M - y_k^M}{U_{k+1}^M - U_k^M}(U - U_k^M). \tag{B.2}$$

B.2 Horizontally Sensitive Sensors: Two-Dimensional Linear Interpolation

Let $U(x, y)$ be the sensor output voltage of a horizontally sensitive sensor for a target position (x, y). Furthermore, let

$$x_k \leq x \leq x_{k+1} \tag{B.3}$$

and

$$y_l \leq y \leq y_{l+1} \tag{B.4}$$

be true for (x, y). Then $\tilde{U}_1(y)$ and $\tilde{U}_2(y)$ can be determined by interpolation between the neighboring y-slices y_l and y_{l+1}:

$$\begin{aligned} \tilde{U}_1(y) &= U_1 + \frac{U_4 - U_1}{y_{l+1} - y_l} \cdot (y - y_l) && \text{(B.5)} \\ \tilde{U}_2(y) &= U_2 + \frac{U_3 - U_2}{y_{l+1} - y_l} \cdot (y - y_l). && \text{(B.6)} \end{aligned}$$

$\tilde{U}_1(y)$ and $\tilde{U}_2(y)$ can in turn be used to interpolate $U(x, y)$:

$$U(x, y) = \tilde{U}_1 + \frac{\tilde{U}_2 - \tilde{U}_1}{x_{k+1} - x_k} \cdot (x - x_k). \tag{B.7}$$

Solving equation (B.7) for the horizontal position x yields

$$x(U, y) = x_k + \frac{x_{k+1} - x_k}{\tilde{U}_2 - \tilde{U}_1} \cdot (U - \tilde{U}_1). \tag{B.8}$$

List of Figures

List of Tables

Bibliography

[1] The LEP Collaborations ALEPH, DELPHI, L3, OPAL, the LEP Electroweak Working Group and the SLD Heavy Flavour and Electroweak Groups. *A Combination of Preliminary Electroweak Measurements and Constraints on the Standard Model.* hep-ex/0112021. CERN: December 2001.

[2] ATLAS-Collaboration. *ATLAS Detector and Physics Performance – Technical Design Report.* CERN/LHCC 99-15. CERN: 1999.

[3] The LHC project.
`http://lhc-new-homepage.web.cern.ch/lhc-new-homepage/`.
Website: last access November 2002

[4] Deile, Mario. *Optimization and Calibration of the Drift-Tube Chambers for the ATLAS Muon Spectrometer.* Doctoral thesis. LMU Munich: 2000.

[5] Jackson, John David. *Classical Electrodynamics.* 3rd edition. New York: John Wiley & Sons, Inc, 1999.

[6] Particle Data Group, D.E. Groom et al.. *European Physical Journal* C15(2000).

[7] Wille, Klaus. *Physik der Teilchenbeschleuniger und Strahlungsquellen.* Stuttgart: Teubner, 1996.

[8] Wiedemann, Helmut. *Particle Accelerator Physics II - Nonlinear and Higher-Order Beam Dynamics.* 2nd edition. Heidelberg: Springer, 1999.

[9] ATLAS-Muon-Collaboration. *ATLAS Muon Spectrometer – Technical Design Report.* CERN/LHCC 97-22. CERN: 1997.

[10] ALEPH, DELPHI, L3 and OPAL Collaborations, The LEP Working Group for Higgs Boson Searches. *Search for the Standard Model Higgs Boson at LEP.* LHWG Note/2002-01. Amsterdam: July 2002

[11] Hessey, N.; A. Staude and T. Trefzger. *Cosmic Ray Test Stand at the LMU Munich.* ATLAS-Note MUON-98-266. CERN: 1998.

[12] X-QC Muon group, ATLAS.
`http://x.home.cern.ch/x/xtomo/www/2D-Results.html`.
Website: last access November 2002.

[13] Kortner, Oliver. *Schauerproduktion durch hochenergetische Myonen und Aufbau eines Höhenstrahlungsprüfstands für hochauflösende ATLAS-Myonkammern.* Doctoral thesis. LMU Munich: 2002.

[14] Kortner, Oliver et al.. *First Results from the Cosmic-Ray Test-Facility at LMU Munich.* To be submitted to the ATLAS collaboration. CERN: 2002.

[15] Groenstege, H. L.. *The coding of the mask for CCD_Rasnik.* NIKHEF Technical Note ETR_94-10. NiKhef: 1994.

[16] Groenstege, H.L. and P.A.M. Rewiersma. *RasLeD - The lightsource for the RasNik alignment system..* NIKHEF Technical Note ETR_99-04. NiKhef: September 1999.

[17] Groenstege, H.L. and P.A.M. Rewiersma. *RasCaM - The sensor for the RasNik alignment system..* NIKHEF Technical Note ETR_99-03. NiKhef: September 1999.

[18] VLSI Vision Ltd.. *VISION VV 5430 Monolithic Sensor.* Product Datasheet. 1998.

[19] Van der Horst, Astrid. *Measurements on RASNIK.* NIKHEF Technical Note. NiKhef: February 1995.

[20] Dicker, Gerald. *Linearity, Resolution, and Systematic Errors of the CCD-RASNIK Alignment System.* NIKHEF Technical Note. NiKhef: May to July 1997.

[21] Hashemi, Kevan S. and James R, Bensinger. *Pixel CCD RASNIK.* ATLAS Internal Note MUON-No-180. CERN: 1997.

[22] Van der Graaf, Harry. Private Communication. June 2002.

[23] Van der Graaf, H.; H. Groenstege, F. Linde and P. Rewiersma. *RasNiK, an Alignment System for the ATLAS MDT Barrel Muon Chambers – Technical System Description.* NIKHEF Technical Note. NiKhef: April 2000.

[24] Ostaptchuk, Andrei. *MonteCarlo Simulation of the In-Plane Alignment System.* ATLAS Internal Note MUON-NO-96-108. CERN: 1996.

[25] Mackall, Scott William. *Measurement of the Stability in the Relative Alignment between the Silicon Microvertex Detector and the Time Expansion Chamber Subdetectors in the L3 Experiment at CERN during the 1994 Large Electron Positron Collider Run.* Master thesis. Tuscaloosa: 1995.

[26] Busenitz, Jerry; Oliver Kortner and Hans Tuchscherer. *Analysis of the 1996a CDMS Data*. L3 Internal Note. CERN: 1996.

[27] Kraus, Alois. *Genaue Bestimmung der Ereigniszeit und Entwicklung eines Alignierungssystems für einen großen Höhenstrahlteststand*. Diploma thesis. LMU Munich: 2001.

Acknowledgements

I should like to express my gratitude to Mrs. Professor Dorothee Schaile for the opportunity to do a diploma thesis at her chair of particle physics, for her support throughout the time I have spent working on it and for her commitment to the students attending her lectures due to which my interest in particle physics was awakened.

In high energy physics however, the scale of experiments has reached a magnitude which creates the need for a lot of scientists working together as a team. Although the Munich Test Facility is not very large compared to the ATLAS experiment as such still a team of physicists is needed for its setup, its operation and the analysis of the gained experimental results. This is why I should like to thank everybody who actually worked at the test facility directly or indirectly and thus made an important contribution to this thesis.

But, as always, there are some very special persons without whom neither my time spent working on this thesis nor the outcome would have been the same. This is why I should like to express my thankfulness to:

- Oliver Kortner for his "hands-on" support, his help with physics and analytical problems and especially for his friendship
- Arnold Staude for his interest in the progress of my work, his advice, his suggestions and for allowing me to use his house at Excheneveux
- Andrei Ostaptchuk for the readiness to explain the working principle of his program, for offering his help in writing new code and for all the time he dedicated to this
- Otmar Biebel for trying to help wherever he could and just for listening which can be very hard sometimes
- Jörg Dubbert, who was of great assistance solving quite a few software problems and spent a lot of time and effort proofreading this thesis, focussing on the physics presented

- Cornelius Fritz Vollmer and Philipp Schieferdecker, who were always willing to help when I encountered problems while using ROOT
- Linda B. and Walter D. Stewart for being good host parents during my high school year as an exchange student in America, thus offering me the opportunity to improve my English and for still being good friends
- Norbert Volkwein for time and effort invested in proofreading this thesis for correct English
- Michael Deveaux for his support, his firm belief in my abilities and his exceptional and unconditional friendship
- Karl Gössling for being one of my truest friends, for his open ears and good advice, for protecting my love for judo and for all the time we have spent together off and on the tatami
- My parents for offering every support they were able to, thus allowing me to pursue my studies, for never questioning neither the purpose of my doings nor their outcome, for believing in their son and for their deep friendship

Finally thank you to those who always have been or became good friends to me during my years at the university, especially to Sven Passlack. Special thanks go to my sister Stefanie Stiller just for being herself.

Ich versichere hiermit, die vorliegende Arbeit selbstständig verfaßt und keine anderen als die angegebenen Quellen und Hilfsmittel verwandt zu haben.

Gerd Wolfram Stiller

München, 13. Dezember 2002